POLITECNICO DI MILANO

School of Industrial and Information Engineering

Master of Science in Materials Engineering and Nanotechnology

PHONONIC CRYSTAL BASED LENSES FOR FOCUSING AND ENERGY HARVESTING

Supervisors:
Prof. Alberto CORIGLIANO

Prof. Attilio Alberto FRANGI

Dott. Valentina ZEGA

Master Thesis By:
Marco ANTONACCI
Matr. N. 918027

Academic Year 2019-2020

Ai miei amici e alla mia famiglia.

Abstract

In recent years, sensors and micro-devices are becoming more and more part of our everyday life, as their presence is increasing in a very high number of appliances, from smartphones and gaming apparatus to domotics and IoT applications. As such, there is a growing trend in the research and academic world toward the study and development of mechanisms which can allow such systems to be powered autonomously, allowed even by the fact that the smaller dimension of sensor, nowadays, makes them less power consuming. In this work, the aim is focused on the review of solutions which allow to concentrate the displacement and the energy of vibrations in a single spot, to pose ground for further investigation of EH systems coupled with lenses. In particular, the focus has been put on phononic crystal based lenses. Phononic crystals are periodic structures which aim at tailoring material properties by exploiting physical or geometrical features, like local inclusions of height variations. As a result, by proper modifications of the structure of the device, local tuning of the refractive index for elastic waves can be enabled, which will allow to build lenses. Three different devices are tested, in particular a GRIN lens, which focuses waves on the centre of the device, and two Luneburg lenses, which focus waves at the diametrically opposed point with respect to the entrance one. The aim is to compare their results in terms of focusing ability and frequency range of validity. Based on the found results, the following step will test the ability of such structures not only to amplify wave displacement, but in their efficiency in concentrating the energy that waves carry in a single localised point, with the potentiality of being used for energy harvesting purposes if results are promising. As such, the final discussion is dedicated to the overview of which device could be the best for a possible prototype realization.

Abstract

Negli ultimi anni, sensori e microdispositivi stanno diventando sempre più parte integrante della nostra quotidianità. Ne è testimonianza la loro presenza all'interno di dispositivi che usiamo giornalmente, notevolmente aumentata. Se, qualche anno fa, le applicazioni che ne prevedevano l'utilizzo erano molto più limitate, anche per una questione di costo, oggi sensori sono installati in dispositivi molto comuni quali smartphone, consolle di gioco, per arrivare a dispositivi per la domotica e l'IoT. Da questa osservazione nasce una problematica, ovvero come riuscire a dare energia a ciascuno di questi dispositivi, tutti in connessione tra di loro, in maniera sostenibile. Ad oggi molte soluzioni prevedono batterie però, allo stesso tempo, la ricerca sta sviluppando prototipi e tecnologie che permettano il riciclo e l'accumulo di energia dall'ambiente circostante, con l'obiettivo finale di riuscire a fornire energia a questi sistemi in maniera più eco sostenibile. Questo oggi è reso possibile anche dal fatto che le dimensioni più ridotte dei sensori permettono di ottenere un'efficienza energetica molto maggiore. In questo lavoro di tesi, l'attenzione è stata posta sull'utilizzo di lenti per onde elastiche basate su strutture definite cristalli fononici. I cristalli fononici sono strutture periodiche, artificialmente realizzate che, grazie allo sfruttamento di proprietà fisiche dei costituenti e della periodicità stessa, permettono di regolare localmente le proprietà del materiale. Questo, nel nostro caso, consente la regolazione dell'indice di rifrazione per le onde elastiche, di modo tale che si possano costruire delle lenti che focalizzino le onde entranti in un punto ben preciso del dispositivo. In particolare, tre diversi dispositivi sono stati analizzati: una lente GRIN, che si pone l'obiettivo di focalizzare onde al centro della lente stessa, e due lenti di Luneburg che, invece, hanno come obiettivo la focalizzazione delle onde sul punto diametralmente opposto a quello di entrata. I risultati ottenuti, mediante simulazione numerica, vengono confrontati per verificare la riproducibilità dell'effetto di focalizzazione e per testare in che intervallo di frequenze il fenomeno sia nettamente visibile. Una volta individuato il dispositivo migliore per ogni categoria, questi vengono confrontati ulteriormente per testare se, oltre ad un incremento della magnitudo di spostamento, le lenti offrono dei tangibili effetti di localizzazione dell'energia. In questo modo, è possibile ipotizzare l'utilizzo di tali strutture per EH mediante l'utilizzo di layer piezoelettrici. Infine, una volta compreso quale sia il dispositivo più promettente, viene proposta una discussione sulla effettiva realizzazione di un prototipo.

Contents

List of Tables

List of Figures

Chapter 1

Introduction

With a continuously increasing number of sensors is used in devices of everyday life, there is a constantly growing need of finding an efficient way of giving them power. The most reliable source of energy are batteries, which come with problems of maintenance and durability. Hence, the need for finding alternatives which are more ecological, with the final aim of wirelessly powering those sensors. Vibration energy harvesting aims exactly at this purpose, to collect power from the environment, accumulate it and reuse it when needed. Between the different strategies that can be used to absorb and collect power from the environment, nowadays there is a growing interest toward the use of metamaterials and phononic crystal based strategies. They can be defined as artificial structures which are created thanks to the periodic repetition in space of a single geometric unit. The main interesting feature of such novel materials is that their material properties are strongly influenced by the geometrical features of the repeating unit. By changing it, properties can be tailored. This master thesis focuses on the construction of different phononic crystal structures to build different prototypes of lenses. Three different types of lenses will be considered, following designs found in literature. Once defined, each lens will be numerically tested, to correctly address their capabilities in terms of focusing. Then, the final discussion will be dedicated to their possible efficiency in applications for energy harvesting. The work is organized as follows. Chapter 2 is dedicated to the overview of the theory exploited in this work. First, an explanation on phononic crystals and their band structure is presented, to understand how waves propagate inside them. After, a more general description of elastic waves in solids is given. Then, a description of lenses and their working principle is given, to finally conclude with how the realization of lenses with phononic crystals can be possible. Chapter 3 proposes a discussion on energy harvesting, with a focus on the review of different solutions based on metamaterials. Then, three different prototypes are going to be tested. Chapter 4 describes the realization and the numerical testing of the first device, here referred to as "GRIN Prototype". Chapter 5 describes the realization of the first Luneburg Lens, here referred to as "Luneburg Prototype 1". Then, chapter 6 describes the realization of the second Luneburg lens, also referred to as "Luneburg prototype 2". For each device tested, the correspondent chapter first describes the theory employed behind the realization of such structure. In particular, the focus is put on how it has been possible to match the theoretical refractive index profile of the lens to the one associated to the phononic crystal structure. Then, frequency analysis performed with numerical simulations are reviewed. The aims, here, are two. The first is to prove if focusing can be achieved. Then, the next step is to check for which range of frequency the device allows to reproduce the correct phenomena. Last, in all this three chapters a final discussion is carried out on time domain simulations, aiming at confirming the functioning of the device and at testing the efficiency of vibration based energy harvesting on some prototypes. Finally, chapter 7 contains final concluding remarks, selecting which of the different designs reviewed proved to be the most promising.

Chapter 2

Metamaterials: Definition and examples of applications

In the research field of environmental vibration energy harvesting, an innovative group of structures has rose to prominence in recent years for their ability to control sound wave propagation. These structures are often called metamaterials. By definition, a metamaterial is an artificial periodic structure which is created with the precise purpose to locally tailor its material properties, for instance stiffness, speed of travelling waves and Poisson's ratio, in order to obtain final objects with innovative characteristics which cannot be found naturally in existing materials, like waveguiding abilities. The idea for these structures came from the observation of real crystals, where the study of electronic states lead to the conclusion that electrons cannot have any value of energy available, but they are constrained to have precise energy levels dictated by the structure of the crystal itself. In fact, the presence of potential energy in crystals and the periodicity of the structure are the main responsible for the opening, in the dispersion curves for electrons, of forbidden energy levels, called bandgaps[1]. In light of this behaviour, numerous efforts have been employed into demonstrating the same effect that we can see with electrons for electromagnetic and elastic waves. This led to the theoretical postulation first, then practical demonstration, of the existence of photonic and phononic crystals, where bandgaps for the propagation of light or sound waves, depending, arise. Since we are interested in elastic wave propagation, we focus now on the description of the latter. In this chapter a detailed explanation on metamaterials is carried out, with a precise focus on the working principle behind them. In particular, section 2.1 deals with the description of crystals in physics and the derivation of their dynamic theory, essential for understanding the calculation of dispersion relations, which play a key role for wave propagation. Section 2.2 deals with the more general phenomena of wave propagation in elastic media, with focus on guided wave modes or Lamb modes, which are the subject of our study. Section 2.3 describes the working principle of lenses and the theoretical derivation of the refractive index profiles needed for their realization. Last, section 2.4 deals with how we can induce locally in metamaterials the variation of a wave's speed, to create such presented structures.

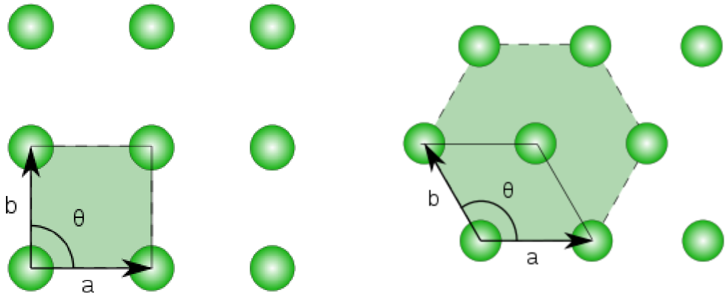

Figure 2.1: From Wikipedia (https://it.wikipedia.org/wiki/Reticolo_di_Bravais), graphical representation of two 2D lattices with a unit cell. Left: square symmetry. Right: Hexagonal symmetry

2.1 Phononic Crystals: Dynamic Theory

First, crystals are defined as structures where a geometric entity, called primitive cell, is repeated in 3D space by translation. Considering a simple bidimensional case, a graphical representation of a crystal is given in image 2.1, where the primitive cell underlined in both figures is able to replicate the entire structure of the crystal by translation only. Crystals, to be fully characterized, need to be described by a lattice system and a base. We can define lattice systems as the geometrical backbone structures of the unit cell, described by three angles and three edges. Each lattice system differs from the others for at least one of these variables. They are 7: cubic, monoclinic, triclinic, hexagonal, orthorhombic, rhombohedral and tetragonal. A base, on the other hand, contains informations on where, in the unit cells, atoms are located. The union of lattice systems with precise bases gives birth to *Bravais Lattices*. Not all combinations between bases and lattice systems are possible, in fact only 14 of them exist in natural materials. A unit cell is called primitive if it cannot be reduced in smaller sized cells which correctly reproduce, by translation, the entire crystalline material. Once a definition of a primitive cell has been given, it is essential to introduce another important geometric entity, which is called reciprocal lattice, of which

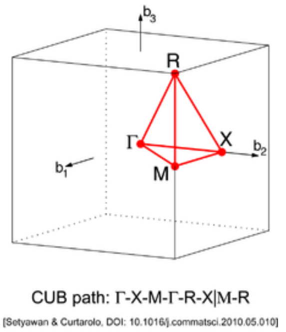

Figure 2.2: From Wikipedia (https://en.wikipedia.org/wiki/Brillouin_zone), Graphical representation of a 3D Brillouin zone for a simple cubic lattice.

an example is reported in figure 2.2. Essentially, the reciprocal lattice is the Fourier transform of the primitive unit cell, which leads to the formation of another unit cell, also primitive, in a 3D space where vectors are represented by the momentum k. The primitive unit cell of the reciprocal space is called first Brillouin zone, and the study of its properties is of key importance in explaining scattering and bandgap opening. Having cleared what a crystal is, the next step is dedicated to dynamic theory's derivation, which is essential for explaining wave propagation behaviour inside crystals and the opening of bandgaps in their dispersion relations. This purpose can be realized with the introduction of the Born-Von Karman model[2] and the explanation of its core implications. The problem is going to be treated with a semi-classical approximation, which means that the main assumptions are derived starting from classical physics' equations, after which a quantum treatment will be needed. The first step is taken by writing the position of the generic nucleus p following the Born and Huang notation, as

$$r\begin{pmatrix} p \\ \mathbf{n} \end{pmatrix} = \mathbf{R_n} + \mathbf{r}_p = n_1\mathbf{a}_1 + n_2\mathbf{a}_2 + n_3\mathbf{a}_3 + \mathbf{r}_p \tag{2.1}$$

where $\mathbf{R_n}$ represents coordinates of the lattice points, while $\mathbf{r}_p$ represents the position of the nucleus written following the internal reference system of the cell itself. If vibrational motions exist in the crystal, the displacement vector $\mathbf{u}$ can be written as the difference between the position after and before motion, like

$$\mathbf{u}\begin{pmatrix} p \\ \mathbf{n} \end{pmatrix} = \mathbf{r'}\begin{pmatrix} p \\ \mathbf{n} \end{pmatrix} - \mathbf{r}\begin{pmatrix} p \\ \mathbf{n} \end{pmatrix} \tag{2.2}$$

If we are at thermodynamic equilibrium, a potential function can be written by a series expansion arrested at the second order as

$$U_v = \frac{1}{2}\sum_{\mathbf{nn'}}\sum_{pp'}^{1,s}\sum_{jj'}^{1,3}\Phi_{jj'}\begin{pmatrix} p & p' \\ \mathbf{n} & \mathbf{n'} \end{pmatrix} u_j\begin{pmatrix} p \\ \mathbf{n} \end{pmatrix} u_{j'}\begin{pmatrix} p' \\ \mathbf{n'} \end{pmatrix}. \tag{2.3}$$

The tensor $\Phi_{jj'}$ is also called interatomic force constant tensor and is defined as

$$\Phi[\begin{pmatrix} p & p' \\ \mathbf{n} & \mathbf{n'} \end{pmatrix} = [\Phi_{jj'}\begin{pmatrix} p & p' \\ \mathbf{n} & \mathbf{n'} \end{pmatrix}] = \frac{\partial^2 U_v}{\partial u_j\binom{p}{\mathbf{n}}\partial u_{j'}\binom{p'}{\mathbf{n'}}} \tag{2.4}$$

The equations which will allow to solve the problem can be written starting from the Lagrangian $L_v = T_v - U_v$ and writing Lagrange's equation. In order to do that, the vibrational kinetic energy of a crystal is needed, which takes the form

$$T_v = \frac{1}{2}\sum_{n}\sum_{p}^{1,s} m_p|\dot{u}\begin{pmatrix} p \\ \mathbf{n} \end{pmatrix}|^2 \tag{2.5}$$

It follows that, writing Lagrange's equation

$$\frac{d}{dt}\frac{\partial L_v}{\partial \dot{u}\binom{p}{\mathbf{n}}} - \frac{\partial L_v}{\partial \mathbf{u}\binom{p}{\mathbf{n}}} = 0 \tag{2.6}$$

$$m_p\ddot{u}\begin{pmatrix} p \\ \mathbf{n} \end{pmatrix} = -\sum_{\mathbf{n'}}\sum_{p'}^{1,s}\Phi\begin{pmatrix} p & p' \\ \mathbf{n} & \mathbf{n'} \end{pmatrix} : \mathbf{u}\begin{pmatrix} p' \\ \mathbf{n'} \end{pmatrix} = \mathbf{F}\begin{pmatrix} p \\ \mathbf{n} \end{pmatrix} \tag{2.7}$$

The obtained equations form a system of $3sN$ Newtonian equations, where s is the number of atoms in the unit cell and N the number of unit cells in the crystal. Now, crystals have been defined as periodic structures. As such, the next step will be the application of boundary conditions which are periodic, as

$$\mathbf{u}\begin{pmatrix} p \\ \mathbf{n} + (N_j - 1)\mathbf{a}_j \end{pmatrix} = \mathbf{u}\begin{pmatrix} p \\ \mathbf{n} \end{pmatrix} \tag{2.8}$$

with $j = 1, 2, 3$ and $N = N_1 N_2 N_3$, where N is the total number of cells available in the crystalline structure. As a consequence of the application of periodic boundary conditions, solutions of the written Newtonian equations have to satisfy Bloch's theorem, so

$$\mathbf{u}\begin{pmatrix} p \\ \mathbf{n} \end{pmatrix} = \mathbf{u}\begin{pmatrix} p \\ 0 \end{pmatrix} \exp^{i\mathbf{qn}} \tag{2.9}$$

where $\mathbf{q}$ represents the available set of wave-vectors inside the 1BZ of the crystal, which are discrete. The fundamental role of Bloch's theorem is exactly ensuring that, to solve this problem, we can reduce the number of equations needed, from 3sN to 3s. This is thanks to the fact that, due to symmetry and periodicity, every situation outside the Brillouin zone can be obtained by studying phenomena inside the zone and, then, by translating them out. As such, the focus now will be put on the study of the fundamental cell, from which the behaviour of the whole crystal can be grasped. Considering the new facts underlined, Newtonian equations can be rewritten again introducing the dynamic matrix, which is the Fourier transform of the interatomic force constant tensor. It is found that

$$m_p \ddot{\mathbf{u}}(p, \mathbf{q}) = -\sqrt{m_p} \sum_{p'}^{1,s} \sqrt{m_{p'}} \mathbf{D}\begin{pmatrix} pp' \\ \mathbf{q} \end{pmatrix} : \mathbf{u}(p', \mathbf{q}) \tag{2.10}$$

with

$$\mathbf{D}\begin{pmatrix} pp' \\ \mathbf{q} \end{pmatrix} = \sum_{\mathbf{h}} \frac{\Phi\binom{pp'}{\mathbf{h}}}{\sqrt{m_p m_{p'}}} \exp^{i\mathbf{qh}} \tag{2.11}$$

Having obtained the final version of the equations, the last missing piece of information is the possible form of sets of solutions. Solutions for this problem can be written in the form

$$\mathbf{u}(p, \mathbf{q}) = \frac{1}{\sqrt{N m_p}} Q(\mathbf{q}) \mathbf{e}(p, \mathbf{q}) \exp^{-i\omega(\mathbf{q})t} \tag{2.12}$$

where two new quantities have been introduced: the polarization unit vector $\mathbf{e}$(p,$\mathbf{q}$) and the scalar complex amplitude Q($\mathbf{q}$). Substituting this expected solution an eigenvalue problem is obtained

$$\sum_{j'}^{1,3} \sum_{p'}^{1,s} \{D_{jj'}\begin{pmatrix} pp' \\ \mathbf{q} \end{pmatrix} - \omega^2(\mathbf{q}) \delta_{jj'} \delta_{pp'}\} e_{j'}(p', \mathbf{q}) = 0 \tag{2.13}$$

Remaining focused on the first Brillouin zone, the solving conditions gives, for every available $\mathbf{q}$ value, 3s solutions $\omega^2(\mathbf{q}) = \omega_\alpha^2(\mathbf{q})$, where α is called branch index. Positive solutions $\omega_\alpha = \omega_\alpha(\mathbf{q})$ are called dispersion relations. Only positive solutions are considered since they are the only one with a physical meaning. All the available solutions can be divided into two types. Of the

3s $\omega_\alpha(\mathbf{q})$ solutions, 3 are referred to as acoustic branches, while 3s-3 solutions are called optical branches. The distinction between them lies in the fact that they are linked to different phenomena: acoustic branches are related to the movement of the centre of mass of the basis, while the other ones refer to the internal motion of the basis. The different nomenclature, on the other hand, highlights another difference. *Acoustic* modes are such called because their motion coincides with that of macroscopic elastic waves when $\mathbf{q} \longrightarrow 0$. *Optical* modes, on the other hand, derive from the fact that corresponding modes can have a fluctuating electric dipole, which strongly influences light absorption properties of the crystal. Acoustic frequencies always exist, while is not the same for optical frequencies. In fact, if $s = 1$, $3s - 3 = 0$ and only acoustic branches exist. Until now, the problem has been treated as a classical one, so no quantization has been introduced. The last step of the derivation is now introduced, which needs the quantum treatment. A more general solution for this problem can be written by a linear combination of obtained solutions like

$$u\begin{pmatrix} p \\ \mathbf{n} \end{pmatrix} = \frac{1}{\sqrt{Nm_p}} \sum_{\mathbf{q}\in\mathbf{BZ}} \sum_{\alpha}^{1,3s} Q(\mathbf{q},\alpha)\mathbf{e}(p,\mathbf{q},\alpha) \exp^{i\mathbf{qn}} \exp^{-i\omega_\alpha(\mathbf{q})t} \tag{2.14}$$

Introducing the vibrational Hamiltonian and substituting the linear combination of displacements we get

$$H_v = \frac{1}{2} \sum_{\mathbf{q}\in\mathbf{BZ}} \sum_{\alpha}^{1,3s} \left\{ |P(\mathbf{q},\alpha)|^2 + \omega_\alpha^2(\mathbf{q}) \, |\xi(\mathbf{q},\alpha)|^2 \right\} \tag{2.15}$$

where $P(\mathbf{q},\alpha)$ are kinetic momenta conjugated to normal coordinates $\xi(\mathbf{q},\alpha)$. This is the practical demonstration that the vibrational behaviour of the crystal itself coincides with that of $3sN$ independent quantum harmonic oscillators. In fact, all this quantum treatments allow to pass from $3sN$ equations in $3sN$ variables to a set of $3sN$ equations

$$\ddot{\xi}(\mathbf{q},\alpha) + \omega_\alpha^2(\mathbf{q})\xi(\mathbf{q},\alpha) = 0 \tag{2.16}$$

which are completely independent. To better explain more practically all those implications and derivations, let's explore a more practical example. The situation of a 1D crystal with 2 atoms per unit lattice will be described hereafter. Let a be the lattice constant, m_1 and m_2 their masses, with $m_1 > m_2$. The atoms will be separated by an equal distance. This means that, if atom 1 is located at the edge of the cell, atom 2 is positioned in the middle. The focus will now be placed on the primitive cell and the derivation will start by taking into consideration only the interaction between this atoms and their first neighbours. After some calculations, the dynamic matrix can be built as

$$D\begin{pmatrix} pp' \\ q \end{pmatrix} = \begin{pmatrix} \frac{2\kappa}{m_1} & -\frac{\kappa}{\sqrt{m_1 m_2}}(1 + \exp^{-iqa}) \\ -\frac{\kappa}{\sqrt{m_1 m_2}}(1 + \exp^{+iqa}) & \frac{2\kappa}{m_2} \end{pmatrix} \tag{2.17}$$

Having found D, it is possible to write the eigenvalues of the matrix, in the form

$$\omega_{1,2}^2(q) = \frac{\kappa}{\mu} \mp \frac{\kappa}{\mu}\sqrt{1 - 4(\frac{\mu}{M})\sin^2{(\frac{qa}{2})}} \tag{2.18}$$

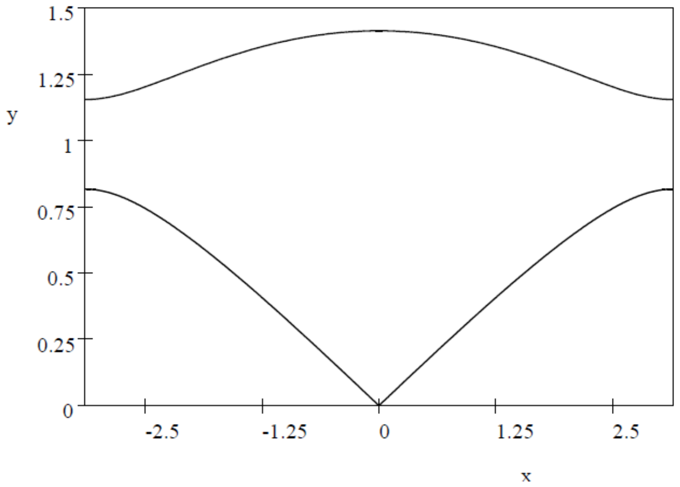

Figure 2.3: Bottani C.E., 2017[2]: Acoustic modes for the simple 1D crystal with 2 atoms pr unit cell. The dispersion relations $y = \omega\sqrt{\frac{\mu}{\kappa}}$ are plotted over $-\pi < x = qa < \pi$

where $\mu = m_1 m_2/2$ is the reduced mass and $M = m_1 + m_2$ is the sum of the ion's masses. Wanting to plot our result a comment can be made on what happens at the origin and at the edges of the first Brillouin zone. If $q \longrightarrow 0$ it is found that

$$\omega_1 \approx \sqrt{\frac{\kappa}{2M}}a\,|q| \tag{2.19}$$

$$\omega_2 \approx \sqrt{\frac{2\kappa}{\mu}}(1 - \frac{\mu a^2 q^2}{8M}) \tag{2.20}$$

while, when at the zone edge, so $q = \mp\pi/a$,

$$\omega_1 = \sqrt{\frac{2\kappa}{m_1}} \tag{2.21}$$

$$\omega_2 = \sqrt{\frac{2\kappa}{m_2}} \tag{2.22}$$

The obtained results can be graphically seen by looking at the graph in image 2.3. We can see that two branches are drawn, corresponding to ω_1 and ω_2. The first branch is acoustic, while the second one is optical. between the two branches, in the frequency range between $\omega_1(\pi/a)$ and $\omega_2(\pi/a)$ it can be noticed that neither of the curve passes there for any q value belonging to the 1BZ. Translated in other terms, this means that a Bragg bandgap opened between those frequencies, which represents forbidden frequencies that cannot propagate in the crystal[3]. The derivation of the dynamic theory is now complete. In our case, the dynamic theory will be of vital importance. In fact, the ability to correctly plot dispersion relations for crystalline materials will be crucial in this work. The study of these graphs is exactly what will allow us to trigger wave propagation control: by tuning locally the properties of the unit cell, the dispersion relation for a given mode changes, allowing to create devices which can focus waves, which is one of our main aim.

2.2 Wave propagation in solids: Bulk and surface waves

Having derived the dynamic theory and its results, the next step is dedicated to the discussion of the more general topic of wave propagation in elastic solid media. Generally speaking, different types of waves can exist and propagate in those materials: body, surface and guided waves[4]. Their nomenclature already tells much about their nature: body waves can exist and propagate only in the bulk of materials, surface waves can propagate only along their boundaries while guided waves, which are our main interest, exist in thin structures, where the presence of two surfaces acts like a waveguide, hence the name. It is interesting to point that the premises to solving those problems are very much similar, as it is often required to start from the Navier's equation or the Christoffel's equation, depending if the medium is isotropic or anisotropic. However, these waves have very different characteristics when it comes to dispersion relations, velocity and direction of propagation. What will pose an extreme difference will be the application of different boundary conditions, owing to dissimilar solutions. Starting this overview with bulk waves, let's suppose to be studying the case of an infinite, elastic and isotropic body with the absence of body forces $F = 0$. The Navier equation then becomes

$$(\lambda + \mu)\nabla(\nabla \cdot u) + \mu\nabla^2 u = \rho\ddot{u} \tag{2.23}$$

Using Helmholtz's decomposition principle to divide the displacement field in the sum of a scalar and a vector potential and substituting it inside the equation we get

$$(\lambda + \mu)\nabla(\nabla\Phi + \nabla\Psi) + \mu\nabla^2(\nabla\Phi + \nabla\Psi) + F = \rho(\nabla\frac{\partial^2\Psi}{\partial t^2} + \nabla \times \frac{\partial^2\Psi}{\partial t^2}) \tag{2.24}$$

Now, since the gradient of Ψ and the curl of Φ are equal to zero, the equation can be rewritten as

$$\nabla[(\lambda + 2\mu)\nabla^2\Phi - \rho\frac{\partial^2\Phi}{\partial t^2}] + \nabla \times [\mu\nabla^2\Psi - \rho\frac{\partial^2\Psi}{\partial t^2}] = 0 \tag{2.25}$$

The final form of the solving equation has already been obtained. If a solution needs to exist, both terms have to vanish, which leads to two possible solutions, the first one being

$$\nabla^2\Phi = \frac{1}{\alpha^2}\frac{\partial^2\Phi}{\partial t^2} \tag{2.26}$$

while the second one is

$$\nabla^2\Psi = \frac{1}{\beta^2}\frac{\partial^2\Psi}{\partial t^2} \tag{2.27}$$

The two equations allow to obtain, as solution, travelling waves inside the medium and, at a more close look, they even resemble in form the classical D'Alembert's equation. The existence of two separate solutions and the possibility to solve them without the need to pose boundary conditions, as we are in an infinite medium, highlights the fact that the solutions are independent from one another, and so they cannot be coupled inside the bulk of the material itself and travel without interaction. So, we can have only two types of waves that

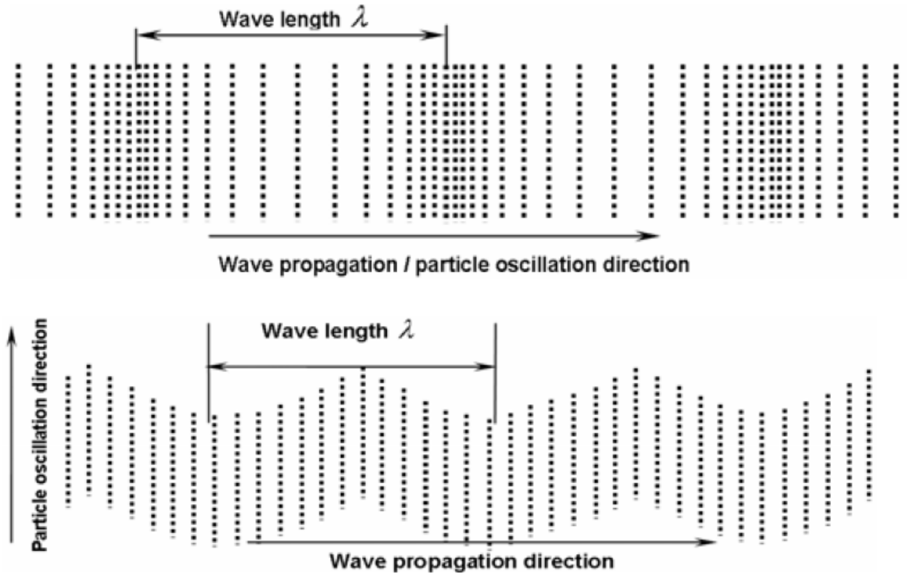

Figure 2.4: Zongquing S. et al, 2009[5]: Top: Graphical representation of a compression or P wave, where the displacement direction matches the propagation direction. Bottom: Graphical representation of a shear or S wave, where displacement is perpendicular to propagation direction.

can exist in the bulk of an infinite homogeneous material. Analysing the two waves that can travel, few interesting points can be highlighted, also noticeable graphically in figure 2.4. The first equation yields a wave which can travel inside the medium with speed equal to α, where

$$\alpha^2 = \frac{\lambda + 2\mu}{\rho} \tag{2.28}$$

These types of waves are called compressional or longitudinal waves because they have nonzero displacement only along the direction of propagation, and so they generate compressive and extensive motions as they propagate. The second equation yields a wave which travels at speed equal to β, where

$$\beta^2 = \frac{\mu}{\rho} \tag{2.29}$$

In this case, the wave has nonzero displacements only in the two directions perpendicular to the direction of propagation. For this reason, these types of waves are also called transversal or shear waves. For every kind of material, $\alpha > \beta$, and this can be simply understood by looking at their formulas. So, longitudinal waves travel at faster speed, and are usually detected first by instruments like seismographs. This precise fact leads to the usage of another terminology to refer to these waves. Longitudinal waves are also called P waves, from prima, as they are faster, while shear or transverse waves are also called S waves, from secunda. Furthermore, in some particular cases, only longitudinal waves exist, for instance in liquid media, since $\mu = 0$ in this case. Having analysed the form and existence of body waves, the other big group of elastic waves are surface ones. In

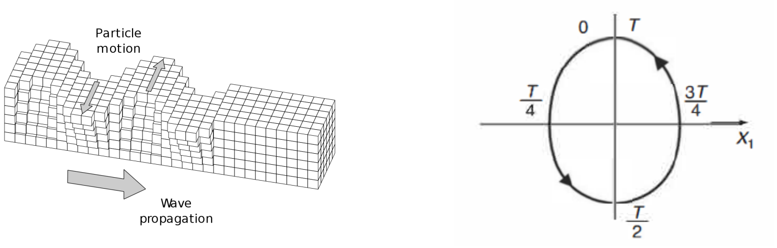

Figure 2.5: Surface waves displacement representation. Left: Love waves, from Wikipedia (https://en.wikipedia.org/wiki/Love_wave). Right: Rayleigh waves, from [4]

more general terms, when waves encounter inhomogeneities in the medium, they suffer phenomena of reflection and transmission. Depending on how parameters like ρ and μ change between subsequent inhomogeneous layers, we have reflection and refraction at different angles, similarly to what happens with light that crosses materials with different refractive indexes. However, if a homogeneous body is considered, like we have done before, ρ and μ are constant. As such, the only possibility that can exist of encountering inhomogeneities in the material occurs at the free surface. There, from the reflection of P and S waves, we can generate new type of waves which come from the constructive interference of different body waves. They are called surface waves because their amplitude of displacement decreases exponentially with the object's depth, similarly to what happens with an evanescent wave. As such, they can propagate with relevant amplitude of displacements only on those boundaries. Even placing ourselves in this scenario, different types of surface waves can exist, differentiating from one another essentially in the geometry of displacement that they cause. More precisely, usually they are divided into Rayleigh and Love waves. Looking at the right image of figure 2.5, Rayleigh waves cause elliptical displacements of particles in the solid material, as they possess both a longitudinal and transverse component of displacement which are out of phase, while Love waves cause horizontal displacements along the body's surface, which is pictured as an horizontal surface in the left image in figure 2.5. As mentioned before, even if the starting point is similar to that of the bulk wave problem, now the absence of an infinite material introduces the need for application of boundary conditions. In particular, the solution can be reached by applying traction free boundary conditions, that are

$$\tau_{31} = \tau_{32} = \sigma_{33} = 0 \tag{2.30}$$

Not only that, but since these waves come from superposition of other waves, their velocity is no more constant, and it depends on frequency. For this reason their frequency-wavelength correlation is often called dispersion relation. Generally speaking, due to their characteristics, surface waves are slower of both P and S waves. Surface waves in general are very much studied in seismology because, due to their high displacements at the surface of the earth's crust, they are the main responsible for structural damage in earthquakes. We now proceed to analyse our main case of interest, that is wave propagation inside a layer of thickness H, or guided wave propagation, represented in figure 2.6. This can be seen as a peculiar surface wave propagation case where two free surfaces are present. In both the case that we start from a longitudinal or shear wave, reflection and refraction across free surfaces occurs, owing to the decoupling of these modes and their superposition. The so called Lamb waves are, then, product of the superposition of reflected waves[5]. The starting point is, as before, represented by the Navier's equation, reported in (2.23). The next step will be dedicated at solving this equation for a system like the one depicted in figure 2.6. The two boundaries, or free surfaces, are placed at positions $x_3 = \pm H/2$. By using the scalar and vector potentials formulation and re-substituting them inside the equation, the following formulation is obtained

$$\frac{\partial^2 \phi}{\partial x_1^2} + \frac{\partial^2 \phi}{\partial x_3^2} = \frac{1}{\alpha^2}\frac{\partial^2 \phi}{\partial t^2} \tag{2.31}$$

$$\frac{\partial^2 \Psi}{\partial x_1^2} + \frac{\partial^2 \Psi}{\partial x_3^2} = \frac{1}{\beta^2}\frac{\partial^2 \Psi}{\partial t^2} \tag{2.32}$$

As a simplifying assumption, the derivation is performed in a plane strain condition. Supposing that the solution takes the form of a plane wave, it can be written that

$$\phi = \Phi(x_3)\exp[i(kx_1 - \omega t)] \tag{2.33}$$

$$\Psi = \Psi(x_3)\exp[i(kx_1 - \omega t)] \tag{2.34}$$

If this tentative form is substituted inside the previous equations, it can be found that

$$\phi = \Phi(x_3) = A_1 \sin(px_3) + A_2 \cos(px_3) \tag{2.35}$$

$$\Psi = \Psi(x_3) = B_1 \sin(qx_3) + B_2 \cos(qx_3) \tag{2.36}$$

where

$$p^2 = (\frac{\omega^2}{\alpha^2} - k^2) \tag{2.37}$$

$$q^2 = (\frac{\omega^2}{\beta^2} - k^2) \tag{2.38}$$

As a consequence of this derivation, equations for stresses and displacements will now be a sum of sine and cosine functions of x_3, which are algebraic functions with different properties. Especially, with respect to $x_3 = 0$, we have that sine is an odd function, while the cosine is an even function. This leads to the possibility of splitting the solution that we can get into two categories: symmetrical

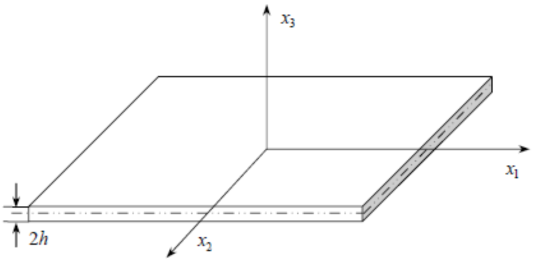

Figure 2.6: Zonqing S. et al, 2009[5]: Graphical representation of a lamina used for the derivation of Lamb waves' dispersion relations.

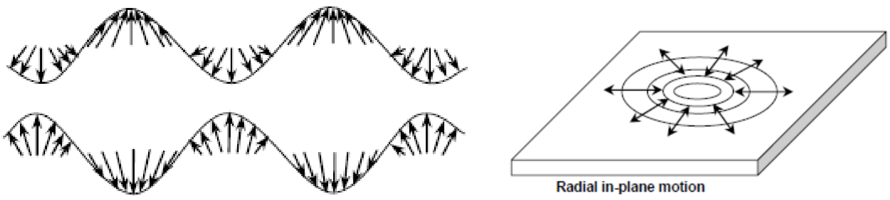

Figure 2.7: Zonqing S. et al, 2009[5]: Graphical representation of the displacement caused by a symmetric lamb wave. Left: displacement symmetry with respect to axis x_1. Right: Graphical representation of the motion caused in the laminar structure.

and antisymmetric modes[6]. Symmetric modes are characterized by having a displacement along x_1, the propagation direction, that is symmetric. For antisymmetric modes the opposite is true, in fact displacements along direction x_1 are antisymmetric. The last step in the derivation is obtaining the dispersion relations and the amplitudes of scalar and vector potentials A_1, A_2, B_1 and B_2, which still are missing. This can be done by applying traction free boundary conditions that are, in the case of plane strain conditions,

$$\sigma_{31} = \sigma_{33} = 0 at x_3 = \pm H/2 \tag{2.39}$$

Discarding trivial solutions, represented by $A_2 = B_1 = 0$ or $A_1 = B_2 = 0$ and making some rearrangements, the dispersion relation are obtained as

$$\frac{\tan(qH)}{\tan(pH)} = -\frac{4k^2pq}{(q^2-k^2)^2} \tag{2.40}$$

$$\frac{\tan(qH)}{\tan(pH)} = -\frac{(q^2-k^2)^2}{4k^2pq} \tag{2.41}$$

Equation (2.40) is the dispersion relation for symmetric waves, while (2.41) is the equation for antisymmetric waves. Taking back the attention on displacements, their graphical representation is clearly depicted in figures 2.7 and 2.8. Symmetric modes will have a symmetric displacement with respect to the x_1 axis. This causes a radial in plane motion of particles. For antisymmetric modes,

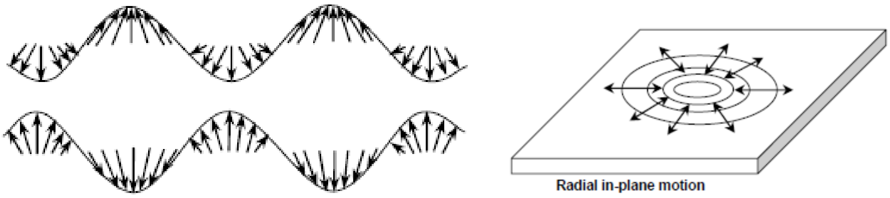

Figure 2.8: Zonqing S. et al, 2009[5]: Graphical representation of the displacement caused by an antisymmetric lamb wave. Left: displacement symmetry with respect to axis x_1. Right: Graphical representation of the motion caused in the laminar structure.

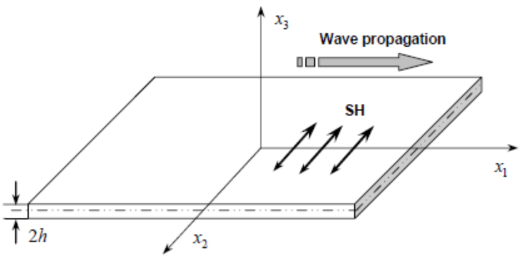

Figure 2.9: Zongqing S. et al, 2009[5]: Graphical representation of the displacement caused by SH waves in a lamina.

on the other hand, displacement is antisymmetric with respect to the x_1 axis, thus particles move in and out of plane. There are infinite solutions that can satisfy the above equations, both for symmetric and antisymmetric modes. It is to be noted, though, that the hypothesis of plane strain limits the number of solutions that can be grasped by solving the problem, as some particular modes will be missing. In particular, modes that cause displacements along u_2 are not grasped by this derivation. To get the solutions that are missing, results have to be obtained from another perspective and, more importantly, without any assumption on the strain state, so now the plane strain assumption will be removed[6]. Let's start supposing that the solution can still be represented by an exponential plane wave and that this form is suitable for representing every one of its reflection when it strikes the surface, as

$$u_j = a_j \exp[ik(x + l_z z)] \tag{2.42}$$

with $j = 1; 2; 3$ and $l_z = \frac{k_z}{k_x}$. From the substitution of this tentative solution form into the Christoffel's equation

$$(k_{il} c_{Ij} k_{Jj} - \rho\omega^2 \delta_{ij}) u_j = 0 \tag{2.43}$$

where $i, j = x; y; z$, $I, J = xx; yy; zz; xy; xz; yz$ and

$$k_{il} = \begin{bmatrix} k_x & 0 & 0 & 0 & k_z & k_y \\ 0 & k_y & 0 & k_z & 0 & k_x \\ 0 & 0 & k_z & k_y & k_x & 0 \end{bmatrix} \tag{2.44}$$

and solving the equation, it can be found that

$$u_j = \sum_{n=1}^{6} C_n \alpha_j^{(n)} \exp[ik(x + l_z^{(n)} z)] (j = x, y, z) \tag{2.45}$$

The goal now is to apply traction free boundary conditions in order to find solutions for the amplitudes C_j. As before, by doing so a linear homogeneous system of equations is found and, searching for non-trivial solutions, the same result as before for what concerns symmetric and antisymmetric waves are retrieved, plus the existence of the extra modes that were missing, which are still infinite in number. The extra modes that have been found are called SH modes,

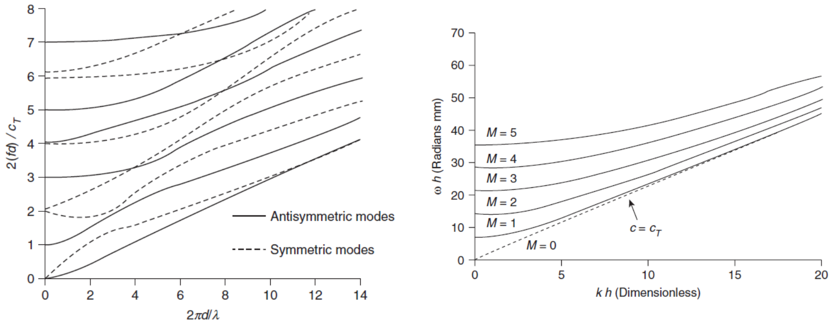

Figure 2.10: Rose J.L., 2014[6]: Representation of the dispersion relations for Lamb waves. Left: S_0 and A_0 waves. Right: SH_0 waves.

their displacement representation can be seen in image 2.9 and their dispersion relation is

$$(M\pi)^2 = (\omega h/\beta)^2 - (kh)^2 \tag{2.46}$$

Note that all the equations found for symmetric, antisymmetric and shear horizontal modes appear to be simple, but usually they can be solved only numerically. Figure 2.10 proposes a graphical representation of their dispersion relations for the first modes. When referring to one of these modes, since they are infinite, usually a number is followed by the type of wave encountered. The first order mode are indicated with subscript zero, all the other with increasing numbers.

2.3 Working principle of lenses

Having concluded the part dedicated to wave transport phenomena in both crystalline structure and generic solids, the next paragraph will be focusing on the structures that we want to exploit for our application: lenses. In optics, a lens is defined as a refractive object that is able to deflect light, usually to achieve focusing or collimation. This allows us to have control on light propagation phenomena. Different types of lenses exist, which differentiate from one another thanks to their different refractive index profile across the lens itself, which allows to trigger different focusing points or deviation effects from device to device. In the next pages, two different types of lenses are going to be analysed, which are the main interest of this master thesis project: a GRIN lens and a Luneburg lens. Starting with the first device, flat GRIN lenses, abbreviation for GRadient-INdex lens, are devices able to focus planar wavefronts entering one edge of the device along their axis[7]. To achieve this kind of focusing, usually a parabolic or hyperbolic secant refractive index profile is needed, which allows to trigger the desired focusing or collimation effect. The hyperbolic secant refractive index profile, for a planar waveguide in plane xz, is

$$n^2(x) = n_s^2 + (n_0^2 - n_s^2)sech^2(\alpha x) \tag{2.47}$$

where, referring to the waveguide pictured in image 2.11, n_s is the substrate's refractive index, n_0 is the refractive index along the z axis and α^{-1} is the position, in the parabolic or HS profile where the refractive index decays to

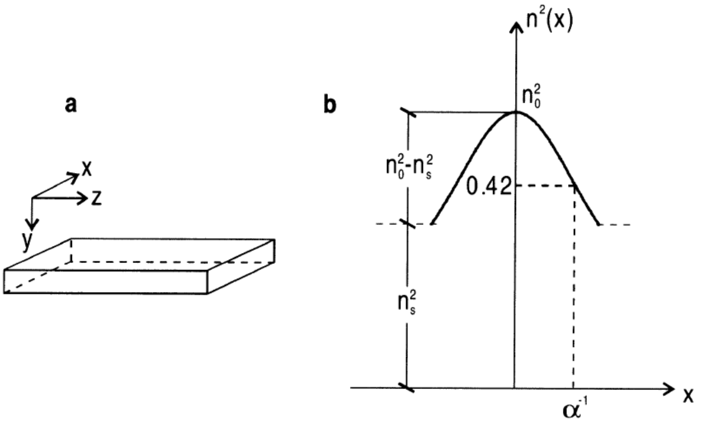

Figure 2.11: Reino C.G. et al, 2002[7]: Left: schematic representation of a planar optical waveguide with the reference system used for the theoretical ray equation derivation. Right: Representation of the hyperbolic secant refractive index profile.

0.42 of its maximum value. Having defined the refractive index, the goal now is to study propagation of beams in this medium. As such, the derivation of the ray equation, which describes the propagation of light between any 2 points, is crucial. The graphical description of the phenomena is reported in figure 2.12. To do this task, the first step consists in writing the expression of the differential arc length along a beam like

$$ds = \sqrt{dx^2 + dy^2 + dz^2} = \sqrt{1 + \dot{x}^2}dz \tag{2.48}$$

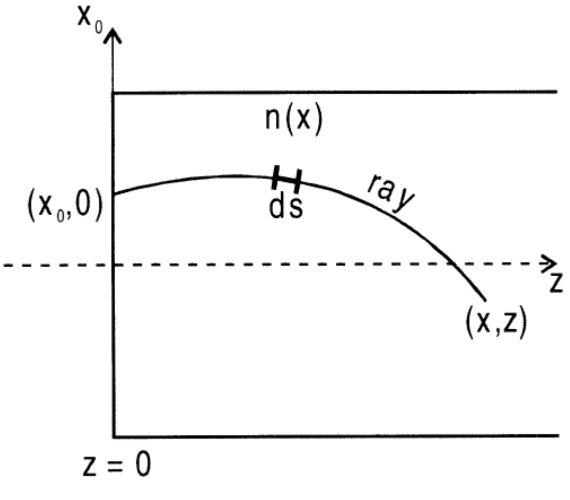

Figure 2.12: Reino C.G. et al, 2002[7]: Representation of the ray trajectory inside the GRIN medium.

After some algebraic passages, the equation can be rewritten, integrated between two points located at z=0 and any z>0. Then, the form of the ray position and slope is obtained, as

$$x(z) = \frac{1}{\alpha}\sinh^{-1}[u(z)] = \frac{1}{\alpha}\sinh^{-1}[u_0 H_f(z) + \dot{u}_0 H_a(z)] \tag{2.49}$$

$$\dot{x}(z) = \frac{\dot{u}(z)}{\alpha\cosh[\alpha x(z)]} = \frac{u_0 \dot{H}_f(z) + \dot{u}_0 \dot{H}_a(z)}{\alpha\cosh\left\{\sinh^{-1}[u_0 H_f(z) + \dot{u}_0 H_a(z)]\right\}} \tag{2.50}$$

where several definitions have been introduced. γ is a function of both the third invariant direction cosine of the beam and the homogeneous substrate's refractive index, while H_a and H_f are called axial and field rays, where

$$H_a(z) = \frac{\sin(\alpha\gamma z)}{\alpha\gamma}; \dot{H}_a(z) = \cos(\alpha\gamma z) \tag{2.51}$$

$$H_f(z) = \cos(\alpha\gamma z); \dot{H}_f = -\alpha\gamma\sin(\alpha\gamma z) \tag{2.52}$$

Now, these formulas have been obtained as an exact solution, without the need to introduce any approximation at all. This means that the hyperbolic secant gradient index profile used has a great advantage over the parabolic one: in fact, this profile is free of aberrations. In the case of a parabolic profile, a similar solution can be found, but some approximations are needed for reaching the final solution. As another remark of this conclusion, the first order arrested Taylor series expansion of the hyperbolic secant is exactly a parabolic plot. Now, having derived the ray equation, we apply it to see where we have to expect collimation or focusing to happen. In particular, to study the focusing and collimation properties, answers are to be found by looking at the zeros of the two defined functions H_a and H_f. For achieving focusing, the condition is

$$H_a(z_m) = \dot{H}_f(z_m) = 0 \tag{2.53}$$

where m is an integer number, and z_m any position in the waveguide satisfying

$$z_m = \frac{m\pi}{\alpha\gamma} \tag{2.54}$$

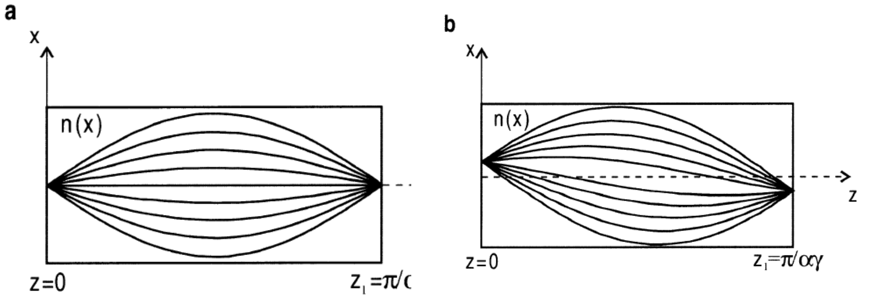

Figure 2.13: Reino C.G. et al, 2002[7]: Graphical demonstration of the focusing capabilities of GRIN planar waveguides for both left: on axis and right: off axis case.

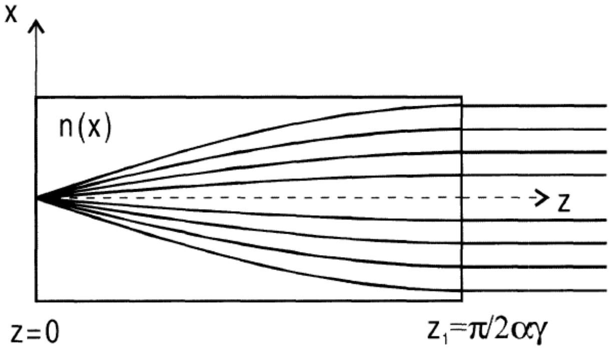

Figure 2.14: Reino C.G. et al, 2002[7]: Demonstration of the collimation capabilities of GRIN planar waveguides.

When this condition is satisfied, it can be found that

$$x(z_m) = (-1)^m x_0 \tag{2.55}$$

$$\dot{x}(z_m) = (-1)^m \dot{x}_0 \tag{2.56}$$

This means that, independently of the starting ray slope at the input position, all rays are perfectly equalized at z_m. The graphical representation of this effect can be seen in images 2.13. Both in the case of an on axis (left) or off axis (right) light source, focusing is achieved. This is one of the two properties that can be exploited by GRIN planar waveguides, the other one, as anticipated, is collimation, which requires the following condition on axial and field rays:

$$H_f(z_p) = \dot{H}_a(z_p) = 0 \tag{2.57}$$

where, again, p is an integer number and z_p any length satisfying

$$z_p = \frac{(2p+1)\pi}{2\alpha\gamma} \tag{2.58}$$

Recalculating position and slope of beams in the Cartesian coordinates we have

$$x(z_p) = \frac{(-1)^p}{\alpha} \sinh^{-1}[\frac{\dot{x}_0}{\gamma}] \tag{2.59}$$

$$\dot{x}(z_p) = 0 \tag{2.60}$$

The situation is graphically represented in image 2.14. This second property is exploited widely in literature, as it allows planar wavefronts entering from one side of the device to be focused on the other side.

The second type of lens that will be investigated in this project is the realization of a Luneburg lens. The device takes its name from the scientist that first solved the light propagation problem across its surface, defining the needed refractive index profile inside it. A graphical representation of the problem solved by Luneburg is reported in figure 2.15. Essentially, for building this device, two

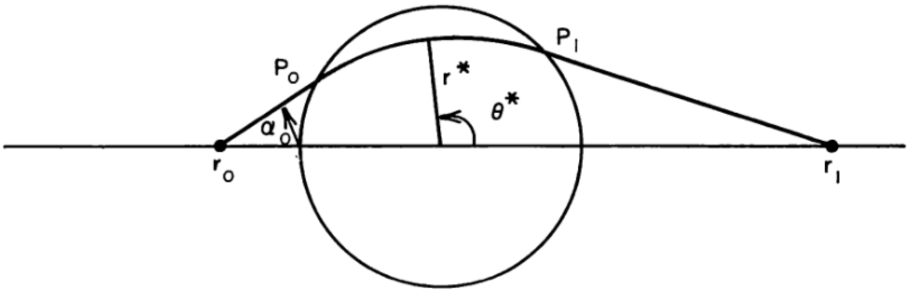

Figure 2.15: Luneburg R.K.[8]: Graphical representation of the generic problem solved by Luneburg.

points have to be fixed, in the figure labelled as r_0 and r_1, which are the two points at which light is focused, one being the starting point of light beams, the other one being the final focusing point[9]. It is clear that endless different lens profiles can arise from this definition. Generally speaking, the problem has been solved following these steps. Due to the symmetry of the given problem, as the device has radial symmetry, the system is going to be described with polar coordinates, defined by r and θ. The light ray equation can then be written as

$$\theta = \theta^* - K \int_{r*}^{r} \frac{dr}{r\sqrt{\rho^2 - K^2}} \tag{2.61}$$

where θ^* is

$$\theta^* = \pi + K \int_{r_0}^{r*} \frac{dr}{r\sqrt{\rho^2 - K^2}} \tag{2.62}$$

and ρ is

$$\rho^2 = n^2 r^2 = K^2 = r_0^2 \sin^2 \alpha_0 \tag{2.63}$$

Depending on our starting point, if the distribution of n inside the material is known, so ρ is given, the equation allows to determine at which position r_1 intersection with the axis verifies. Otherwise, if the r_1 position is known, the necessary profile to obtain such deviation can be retrieved. Our case of interest matches that used by Luneburg in its first derivation of the solution[8]. Since our goal is to focus planar wavefronts on the diametrically opposed point with respect to the entrance one, it follows that one focus is placed at infinite, such that light is perfectly collimated when entering the device, while the second focus is placed at the lens' edge, as depicted in figure 2.16. To obtain a device that allows this propagation, the following refractive index profile has to be adopted

$$n(r) = \sqrt{2 - \left(\frac{r}{R}\right)^2} \tag{2.64}$$

where r is the radial position inside the lens and R the value of its radius. Usually, in literature, Luneburg lenses are designed such that the refractive index, as the profile suggests, is equal to 1 at the external surface, such to avoid reflection at the interface between the outer material and the lens. For now, only light propagation has been taken into account, even if our case of

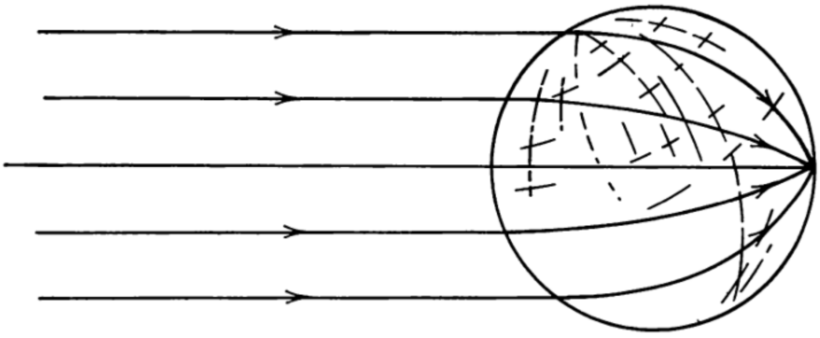

Figure 2.16: Luneburg R.K.[8]: Graphical representation of the Luneburg lens' working principle.

interest is sound wave propagation. Essentially, all the concepts seen up to this point can be extrapolated and reused for elastic waves: a sonic lens has the same goal and the same working principle as a lens for light. As such, the refractive index's variation inside the medium allows to deflect waves. Of course, to achieve this variation, changes in density and Young's modulus are exploited, rather than changes in dielectric constant $\epsilon(r)$. This, as it will be cleared out shortly, can be possible thanks to metamaterial structures. Another peculiarity of lenses for elastic waves is that, thanks to some of the advantages of metamaterials based structures, we are able to change locally the device's properties, refractive index included, with the possibility to create lenses which are flat, with respect to their optical counterpart which, in their most classical realizations, often contain convex elements.

2.4 Metamaterial based lenses: how to tailor the refractive index and application examples

Having just reviewed lenses and their working principle, the issue of how to control elastic wave speed remains. The answer lies in the versatility of metamaterials which, alongside their novel properties, can allow to tailor material properties inside them. As such, they are an optimal choice for this application. Again, by definition, a metamaterial is an artificial periodic structure which is created with the precise purpose to tailor its material properties, in order to obtain final objects with novel characteristics not found naturally in more conventional materials. What is striking and remarkable is that the tailoring in material properties is not achieved by exploiting the chemical properties of its constituents, but rather by proper modification of the geometry of the unit cell. As anticipated before, the observation of real crystals and the study of electrons in them, historically, lead first to the development of photonic crystal, in which variations of the dielectric constant allow to deviate, refract and, more generally, control light propagation. The first practical applications to such derivations came at the end of the last century. For instance, Joannopoulos J.D. et al. in 1997 tried to apply these concepts to prototype devices[10]. They calculated photonic bandgaps for crystalline structures composed of square and hexagonal

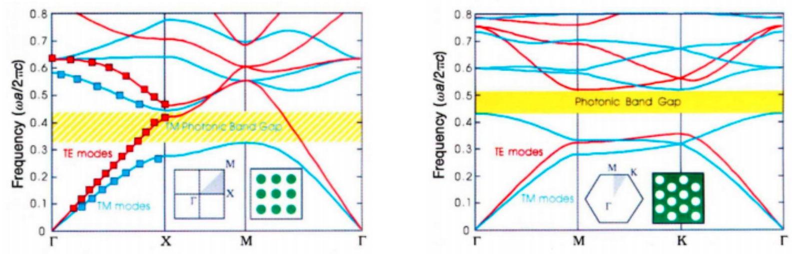

Figure 2.17: Joannopoulos J.D. et al, 1997[10]: Graphical representation of the dispersion relations for two materials with two different unit cells. Left: unit cell with square simmetry. Right: Unit cell with hexagonal symmetry.

unit cells, as it can be seen in images 2.17 Then they applied this concept to create a waveguide. In order to do that, they removed a row inside the perfect crystal layer, thus introducing a defect band inside the forbidden gap, which allows waves to selectively travel only in this region. Figure 2.18 shows the electric field of light propagating in the crystal on the right and its calculated band structure for the used crystal on the left. We can see that the electromagnetic field propagates only where the cylindrical inclusions are not present, since in that region the field fades away, as it turns into an evanescent wave. Once proven correct, the same idea was carried to elastic waves, and phononic crystals were developed. In order to achieve the manipulation of material properties inside the cell, many strategies can be used. the most promising ones will now be reviewed. Some examples, which will be treated more in details in the next pages, could be the variations of the cell's thickness[11], usage of an inclusion with a varying radius[12] or rotation of the inclusion itself[13]. A first example of tailoring wave speed inside phononic crystals can be achieved by modifying the filling ratio of the cell by insertion of an inclusion, either empty or realized with a material different from the bulk one. As an example, Jaeyub H. et al.

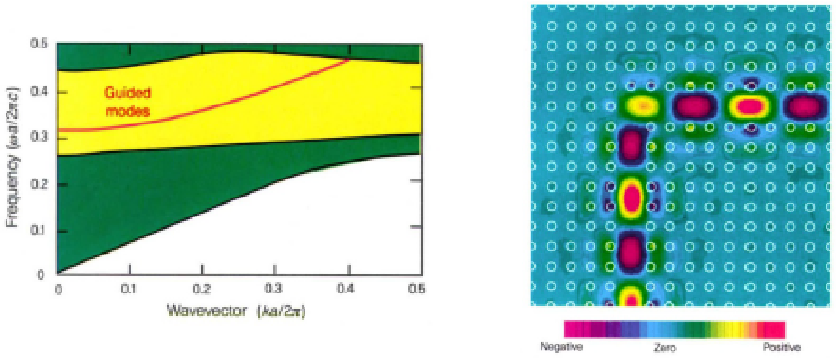

Figure 2.18: Joannopoulos J.D. et al, 1997[10]: Left: Projected photon bands for a waveguide in a square lattice of dielectric rods. The removal of rows of rods creates the red band inside the forbidden bandgap. Right: Simulation showing the electric field output for a propagating electromagnetic wave, which can propagate selectively only inside the waveguide.

proposed a structure working as a GRIN lens by exploiting a circular hollow

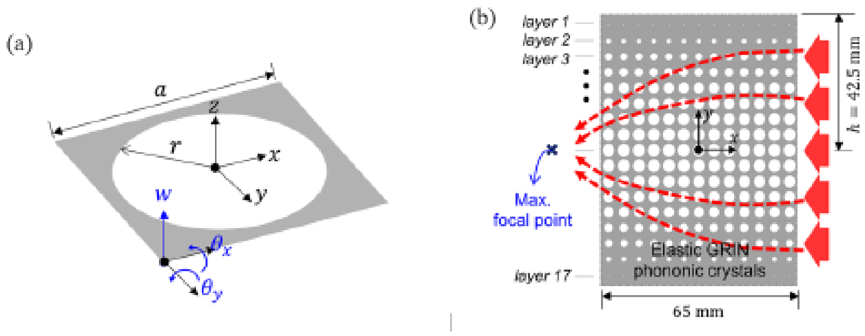

Figure 2.19: Jaeyhub H. et al. 2019[12]: Left: Representation of the unit cell used in this work. Right: Representation of the GRIN structure obtained with the diameter variation.

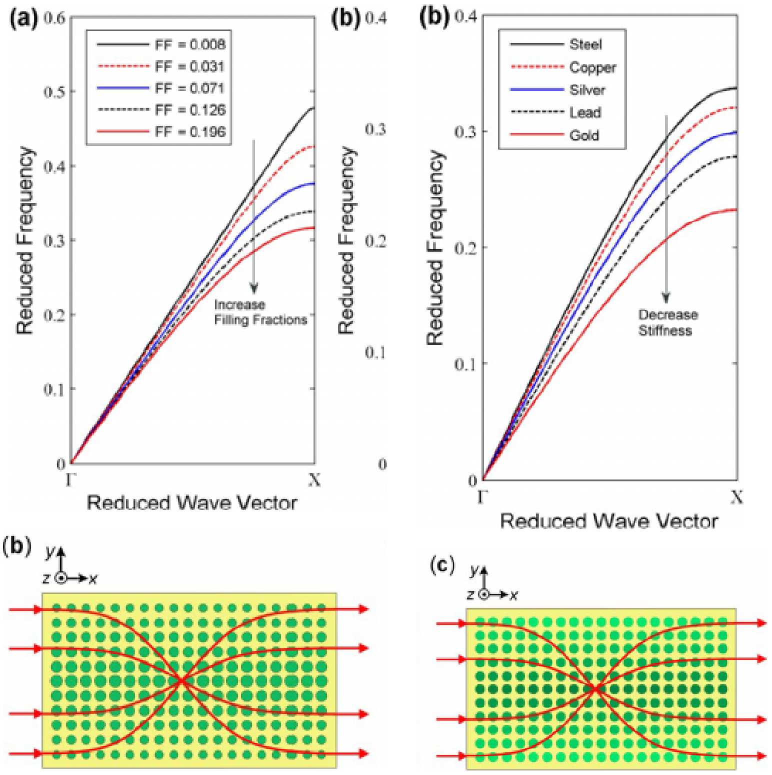

Figure 2.20: Sz-Chin S.L. et al. 2009[14]: schematic representation of the two metamaterial based devices used in their research. Left: Metamaterial composed by a steel matrix with an epoxy inclusion of variable filling fraction. Right: Metamaterial composed by a steel matrix with inclusions of different materials with the same diameter.

inclusion, as we can see in image 2.19[12]. By changing the diameter of the inclusion, hence the filling fraction, different wave speeds can be achieved. In order for the change in wave speed to be effective, the radius of the hollow part has to be tuned with an ideal profile for the refractive index, giving focusing in a given spot. The ideal profile follows the law

$$n_{target} = n_{max} sech(\eta y) \tag{2.65}$$

$$\eta = \frac{1}{h} cosh^{-1}(\frac{n_{max}}{n_{eff}}) \tag{2.66}$$

Once built, the device shows its working capabilities as intended. Other authors exploited a similar idea, using a filled unit cell instead, like Sz-Chin S. L. et al, 2009[14]. Having always as goal the realization of a GRIN structure, they employed two different designs, reported here in image 2.20. While the one on the left aims at achieving the tuning of refractive index by changing the radius' inclusion, so basically the same approach done by the previous paper but with a different material that the bulk one, the second image reveals a different approach, where the tuning is done by exploiting cylinders of constant radius but made of materials with different stiffnesses, which allow waves at a given frequency to travel at different speeds. Also in this case, after the theoretical representation of the unit cell and the calculation of an ideal refractive index profile, the device is built and tested, showing to behave as demonstrated, always with axial focusing. An interestingly different approach has been employed by Yuping T. et al in 2019[13]. In fact, although even they wanted to create a phononic crystal based GRIN plate, they employed a totally different approach, exploiting an asymmetric scatterer. In other terms, they still added a solid constituent to the unit cell, in this case an epoxy resin inclusion in a steel matrix but, what causes waves to change speed and direction of propagation is their orientation. The left image of figure 2.21 explains the concept visually. The selected unit cell has an hexagonal geometry with a scatterer embedded

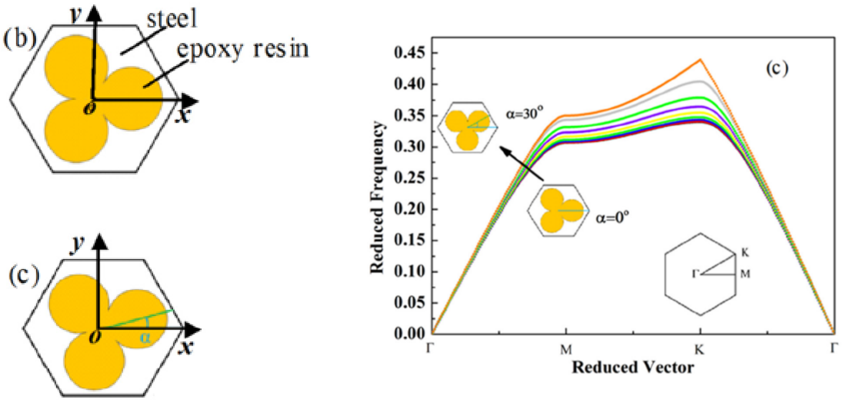

Figure 2.21: Yuping T. et al, 2019[13]: Left: representation of the unit cell employed in this work for the realization of a GRIN device. Right: Plot of the dispersion relations, calculated via numerical software, which show the effectiveness of the inclusion rotation strategy

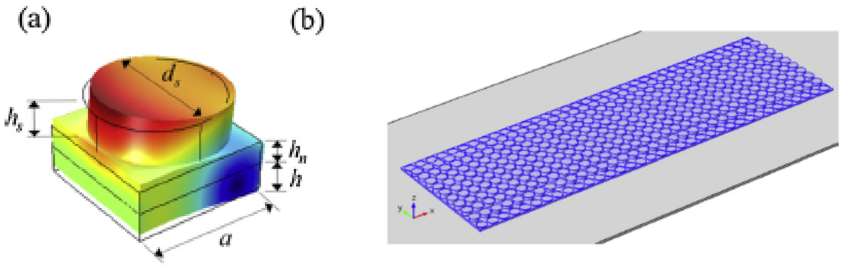

Figure 2.22: Tol s. et al.2019[11]: Left: Representation of the unit cell used in this work for realizing a GRIN plate. Right: GRIN plate obtained by 3D printing.

which has a sort of clover-like form. By rotating the scatterer, inside the GRIN structure, of an angle α between 0° and 30°, they are able to control wave propagation. The right image in figure 2.21 shows how the dispersion relation for waves changes as the inclusion angle is rotated. Once the concept has been proven valid, the aim is to match the value of the refractive index of a given rotated scatterer to an ideal profile that allows axial focusing. Even here, the device showed the predicted behaviour in numerical simulations. More often, solutions in literature exploit out of plane variations of the cell's thickness to induce a variation in the propagation speed for flexural waves. For instance, Tol S. et al, 2019, used an aluminium unit cell with a stub of variable height[11], as reported in image 2.22. By properly changing the diameter, waves travelling in these cells are able to show different travelling speeds. Simulations made with COMSOL Multiphysics software allowed to get the dispersion curve at different diameter values. Then, the estimated refractive index plot, for a given frequency wave, is exploited for the final design of the GRIN device. Another interesting addition is that, in some cases, these effects have been exploited altogether, to have more control over property tuning in these materials. It is the case of the work proposed by Torrent D. et al, 2016[15]. In fact, they designed a complex unit cell, depicted in image 2.23, always for sound wave focusing. It is composed by a rhombus made of aluminium with a double inclusion. The first, denoted by radius R_α, is made of gold, while the second is a hollow inclusion. The double

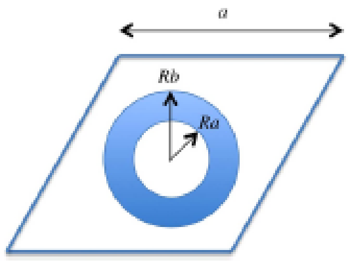

Figure 2.23: Torrent D. et al, 2016[15]: Representation of the complex unit cell used for wave propagation control in the authors' work.

inclusion choice was made for enabling multimodal focusing of the proposed lens in their work, as is demonstrated in COMSOL Multiphysics simulations, where all Lamb waves modes($S_0, SH_0 and A_0$), can be focused altogether. This is due to the fact that they develop an ad hoc model which allows to tune the refractive index profile for each mode separately by changing one of the three cells' variables, which are the two radiuses and its thickness. Furthermore, if the refractive index profile for each mode is correctly regulated, all waves can be focused at the same spot, which is an interesting feature to carry. As it has been demonstrated, there are different articles in literature covering the topic of metamaterials. In particular, there are different strategies available and already tested for changing properties across metamaterials. The effectiveness of some of these will be reviewed even in the next chapter, which focuses on energy harvesting powered by metamaterials.

Chapter 3

Energy Harvesting

In this chapter an overview on energy harvesting is presented. First, the state of the art of such practice is analysed, with the delineation of its main purposes and recent progress. After such a presentation, the attention is shifted back to our case of metamaterial based power scavenging, with the aim of searching the literature for energy harvesting applications which involve the use of metamaterials, to further comment on their potential application on this sector. Energy harvesting can be defined as the ability of scavenging power from an available external source, in order to collect it and reuse it for other purposes. In recent years, with the development of the internet of things, the amount of sensors used in everyday appliances is constantly growing, with purposes ranging from monitoring the health of structures to the use in domotics[16]. The most challenging task, at this point, is to provide a durable and reliable energy source for those devices. Until recent years, sensors were usually designed to be battery powered but, inevitably, this source of energy comes with some drawbacks. First of all, batteries have a limited lifetime, as the chemical reactions that creates energy becomes less efficient in time with degradation of its components. For this reason, they needs maintenance, which is not cost efficient. On top of that, they carry some environmental issues, linked with the difficulty of recycling those devices, which poses another point in favour of more green and eco-friendly alternatives. With the introduction of proper and reliable EH devices, the possibility of wirelessly powering those devices, without the use of an external energy source, becomes very intriguing. The exact reason why in the last decades research teams have grown an exponential interest toward this specific application, however, lies in the analysis of the state of the art of sensor production. With respect to even few years ago, sensors have become much smaller. From one side this means that the cost of a single chip goes down by much, since a wafer can host much more sensors. This is part of the reason why they are much more widespread nowadays. Not only that, but less bulky sensor generally need less power to work properly, and that is the exact reason why research in this topic has grown exponentially. If few years ago the proposed designs for EH devices scavenged insufficient powers, now those values may be enough[17]. Of course, scavenged power varies greatly considering that there are even different sources of energies available to be recycled via harvesting effect, each of them with their own strengths and weak points, all explored in literature: mechanical, wind power, thermal, radiofrequency or light energy harvesting[18].

Remembering that a very important role in scavenging is played by the transducer, which is the part responsible for converting the selected input in electrical power, between these alternatives solar energy seems the one generally capable of giving the highest power densities, in the order of micro-watts per square cm, compared to the others, which are generally less impressive[19]. Of course, solar energy is not always readily available, especially for indoor applications. At this point, other sources become more interesting. In the sensor and MEMS devices world, for instance, one of the most researched technique to date is vibration or motion based EH, which aims at converting existing vibrations, that naturally are present in these devices, to reusable energy. In this frame, the most used transducing technique is indeed piezoelectric transduction, which employs the natural coupling between mechanical strains and charge accumulation that is present in these materials, to produce and store power. Piezoelectricity is the main studied transduction mechanism as it is able to offer great power densities and can easily be implemented in a micro-fabrication process. In fact, growing piezoelectric films on top of MEMS is commonly done, using technologies such as pulsed laser deposition, sputtering or sol-gel technique[17]. Some drawbacks of this material are related to thin films fabrication, which have poor mechanical-electric coupling, and, sometimes, poor mechanical properties. Other transduction mechanism that could be exploited are electromechanical and electrostatic transduction, far less used[20]. In order to analyse and build a device that collects energy from vibrations, the main trade-off that needs to be highlighted is that the natural frequencies of vibrations, that naturally occur in environment, are very small. For example, vibrations from industrial machines are in the few hundreds Hertz range, human motion even an order of magnitude lower. So, if these sources of rather small frequency vibrations are to be exploited, we need to remember that scaling down the dimension of a device increases resonant frequencies, this means that often a trade-off between maximum scavenged power and object size must be attained. Since the aim of this master thesis is to explore which benefits would arise if a metamaterial based sonic lens is coupled to a harvester, such that an increase in energy output can be observed, a bibliographic research on this topic is presented. On this regard, some first attempts have already been proposed in literature. In particular, metamaterials and phononic crystals, exploited for their novel capabilities, have been employed in different forms, like: phononic crystal bandgap materials which exploit defect wave trapping[21]; focusing lenses[22]; funnels and parabolic mirrors[23]. If metamaterials employment for EH is not a new topic indeed, coupled applications that target both EH and sonic lenses are rather few. In the following pages, an overview on some papers that present some of these smart solution is presented, to see which is the true potential of metamaterial applications for EH. For example, in the work presented by Tae-Gon L. et al, the authors decided to exploit the advantages of acoustic black holes in order to trap waves in a point defect created ad hoc in the structure of the metamaterial itself[21]. This allows wave displacement and energy localization. Then, energy harvesting capabilities are reviewed, trying to reach a high generated output power. First, the device is numerically tested, in order to pose solid ground for the energy harvesting considerations. The artificial crystal, in this case, consists of an octahedral unit cell, like the one depicted in figure 3.1. The bulk material is Aluminium, where a hole with this shape is drilled. By usage of COMSOL Multiphysics (R) software, dispersion relations were calculated by application

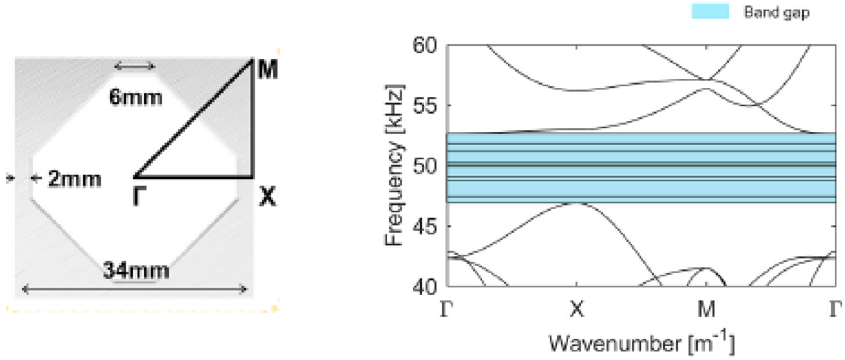

Figure 3.1: Left: Tae-Gon et al, 2020[21]: Representation of the unit cell employed in this work. Right: representation of the dispersion relation calculated via numerical simulations.

of Bloch-Floquet periodic boundary conditions, and the acoustic band structure for the crystal was obtained, showing a clear phononic bandgap, where waves of that frequency (between 47 and 52 kHz) cannot propagate. This is exploited to create a wave trapping structure: by inserting a defect in the crystal, in this case represented by a non drilled unit cell, some defect bands appear inside the previously opened gap, allowing to use the defect as an energy trapping point. The authors then made a simulation with a propagating wave at 50kHz, exactly the frequency of one of those bands induced by the defect presence. When the wave impinges the crystal, it propagates as an evanescent wave until the defect is crossed, and then the displacement of the wave is localized inside the defect, with no escape possibility, since the wave is surrounded by a crystalline structure that reflects that frequency. The position of the defect is not casual, but it has been calculated to give the best localization effect and placed in the

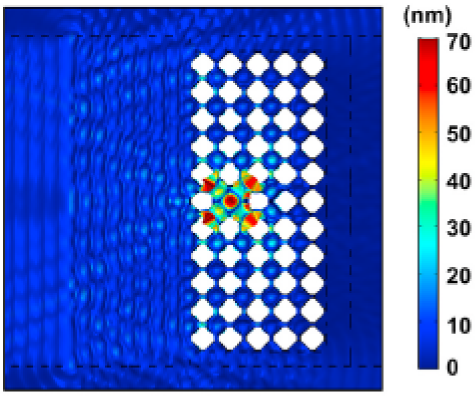

Figure 3.2: Tae-Gon L. et al, 2020[21]: Numerical simulations performed via COMSOL Multiphysics show the correct functioning of a wave trapping structure.

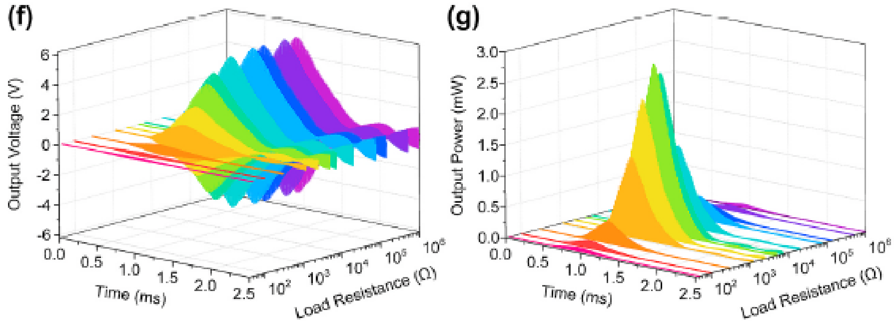

Figure 3.3: Tae-Gon L. et al, 2020[21]: Left: Output voltage registered from a piezoelectric harvester placed inside the metamaterial and right: output power registered in the same situation.

second row of a 5x11 grid. In fact, placing it before would break the symmetry of the phononic crystal, with no bandgap opening, while placing it in an inner position reduces the amount of energy stored, since the wave needs to cross as an evanescent wave a greater portion of the crystal and dispersion takes place. Numerical simulations reported here in figure 3.2. clearly show the localization effect taking place. The idea of the authors was then to employ a piezoelectric disk where the defect was placed, in order to analyse the performance of energy harvesting. The response was evaluated in time domain simulations measuring the output voltage and output power under different resistive loads. The results, reported in figure 3.3, showed that both voltage and power exhibit an increasing trend and reach a maximum value in time domain at 9ms, after which both tend to diminish. Increasing the resistance increases the output voltage, which tends toward its open circuit value, while the maximum power can be generated using the optimal electrical resistance of $4.8k\Omega$. Carrara et al. reviewed, in 2013, different possible metamaterial-based solutions to be employed for energy harvesting, testing them both via numerical simulation and experiments, owing to the confirmation of corresponding theoretical derivations[23]. Three structures have been reviewed: the use of a metamaterial mirror, the use of a 2D lattice with an imperfection, already cited in the previous paper example, and the use of metamaterials as funnels to waveguide vibrations and convey selectively energy to the harvester. Skipping the middle situation,already explained based on results from another paper, the focus will be now put on the other two methods. The first solution studied is the construction of a parabolic acoustic mirror, or PAM, which structure is reported in figure 3.4. Essentially, it consists in a row of cylindrical stubs placed to form a parabular plot, such that Lamb waves coming through, in particular planar A_0 waves, which are flexural, can be scattered from this configuration and concentrate at the focus of the parabola. The spacing of the stubs has been selected with the proper intent of creating a broadband device, capable of working at multiple frequencies. To activate the focusing effect, the spacing needs to be smaller or, at most, of the same order of magnitude of the λ of the incoming wave. Now, to make the numerical simulation, the source has been implemented in the software as a series of point loads which stimulate the plate with a 4 cycle sine burst. Image 3.5 shows the

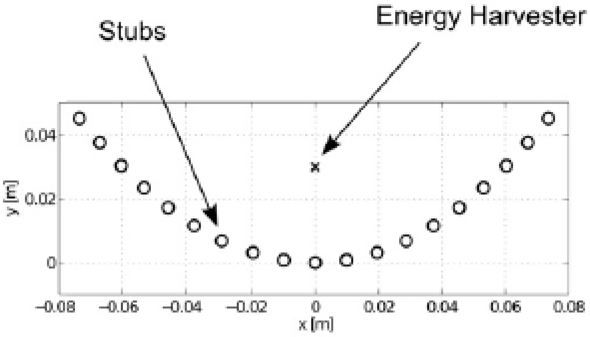

Figure 3.4: Carrara et al, 2013[23]: Schematic representation of the structure of a parabolic acoustic mirror (PAM).

reported results, where the maximum displacement is obtained at the parabola focal point, exactly where predicted. Then, experimental results are performed using the same configuration and using a line array of piezoelectric transducers, which confirms the behaviour predicted by simulations. By performing the same test at different frequencies and plotting the displacement graph on the x=0 line, as done in the right image of figure 3.5, a peak in normalized displacement, placed at point y=30mm and achieved at frequencies around 50kHz, can be highlighted. Going up in frequency a limiting point is reached, where λ becomes smaller that the stub spacing, so the device doesn't work properly anymore, as underlined before. Then, the piezoelectric harvester efficiency is tested, using a disk of given thickness and diameter, attached to an electrical load near to the estimated optimal load for energy harvesters, which is

$$R = \frac{1}{\omega C} \tag{3.1}$$

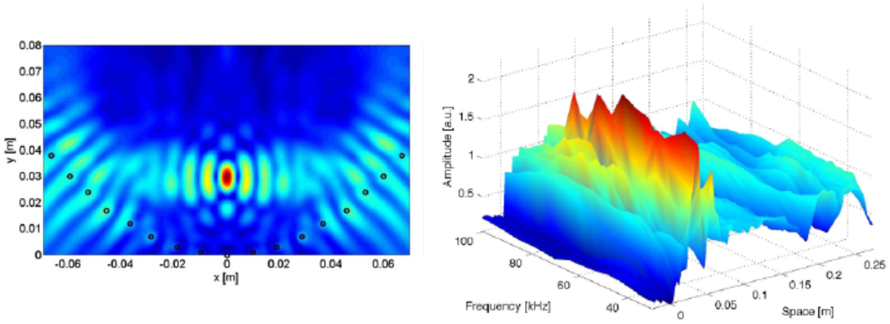

Figure 3.5: Carrara et al, 2013[23]: Left: Numerical simulation shows the correct focusing that PAM device brings when excited with A_0 waves. Right: Plot of the normalized displacement field, along the x=0 line, at different frequencies, showing the focusing point.

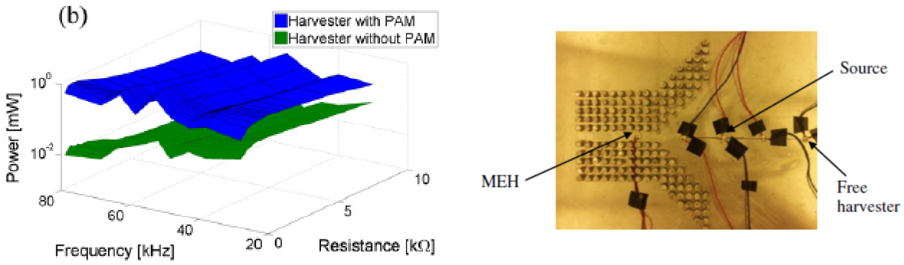

Figure 3.6: Carrara et al. 2013[23]: Left: Comparison between the harvester performance with the PAH and without. Right: Realization of the funnel device.

where ω is the excitation radial frequency and C the the piezoelectric material capacitance. Depending on the frequency analysed, the increase in output power, showed in the left image of figure 3.6, between using or not using the metamaterial device is substantial to say the least, with an average 1800% increase in output power. Passing on, next is discussed the third and last adopted solution described in this work, in which the employed metamaterials for EH is a waveguide that uses an acoustic funnel. In this case, the ability of metamaterials of creating bandgaps for inhibiting wave propagation is still exploited, but in a different manner. As opposed to the previous case, the metamaterial is formed by cylindrical stubs, now arranged in such a way to create a proper "channel", delimited by the absence of those stubs, where waves can selectively propagate, as shown in the right figure of image 3.6. At the end of this channel, a harvester is placed. The following designed metamaterial has two bandgap regions, between 30-60kHz and 90-130kHz. The metamaterial is then numerically tested at 100kHz to check its behaviour and, as expected, the A0 flexural waves cannot propagate in the region where the crystal lies, but only in the properly tailored "channel", as seen in figure 3.7. The last passage was, again, to test the performances of the harvester. In this case, harvested power increases, but not as much as it does with the previous configuration, stopping at a 2x maximum. Switching to metamaterial based lenses, one of the first tries has been performed by Tol S. et al. in 2016 who have developed, for instance, a metamaterial-based GRIN plate that is able to showcase focusing and collimation properties, here

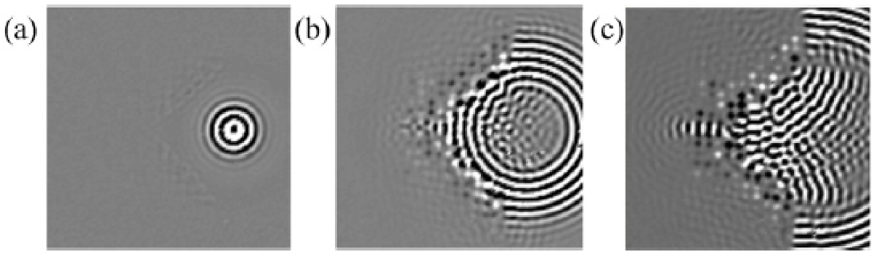

Figure 3.7: Carrara et al, 2013[23]: Numerical simulations showing the performance of the acoustic funnel structure, with waves propagating only in the designed hollow cavity. The three images are shot at different time frames.

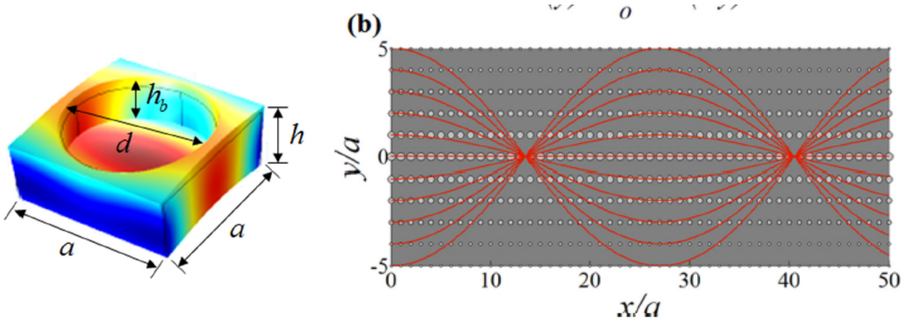

Figure 3.8: Tol S. et al, 2016[24]: Left: Representation of the unit cell used in this work for the realization of a GRIN lens. The blind hole has $h_b = 2.75mm$. Right: Graphical representation trajectories of impinging beams thanks to the grading of the unit cell's hole diameter.

exploited for enhancing EH capabilities[24]. In particular, the authors built a device by adopting a periodic structure with the unit cell depicted in figure 3.8. For changing the wave speed and achieving focusing, they decided to use a blind-hole structured unit cell, with blind hole diameter varying across the profile of the device. The profile used for achieving focusing is

$$n(y) = n_0 sech(\alpha y) \tag{3.2}$$

where α is the gradient coefficient, related to the focusing point, and n_0 is the gradient index value at the centre of the device, where waves are slower. After having calculated at which values of diameter corresponds which refractive index value n(r), the final device can be built. In image 3.8 the form of the ideal profile is visible on the right, with the representation of the calculated beam trajectories. Designed to be working at a frequency of 50kHz, the authors tested its working capabilities by performing an experiment exciting this GRIN material with a sonic wave from a line source made by piezoelectric transducers. Results, reported in image 3.9, show the capabilities of A0 waves to be focused, defocused after the first point and refocused at a much greater distance, as predicted by trajectory calculations. Going above or below the selected frequency gives similar results. However, since the refractive profile changes, authors reported a slight modification of the focusing points. If the α parameter increases, the focusing point position increases too and, vice versa, if α decreases, the position of

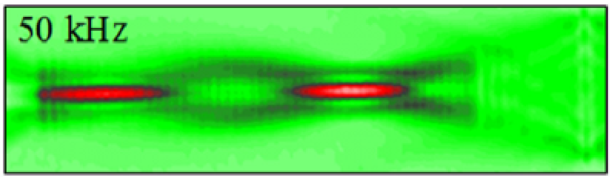

Figure 3.9: Tol S. et al, 2016[24]: Numerical simulation of the working principle of the GRIN lens, with the two focal points clearly visible at x= 13.5a and x=40.5a for f=50kHz.

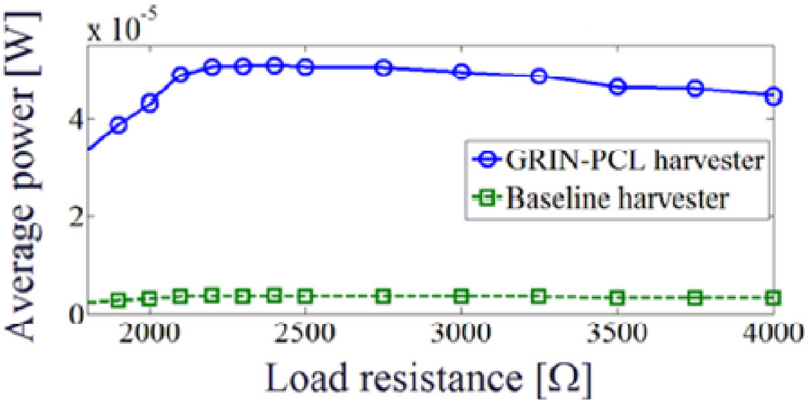

Figure 3.10: Tol S. et al, 2016[24]: Comparison between a baseline harvester and the same harvester with the presence of the GRIN plate.

the focusing point decreases too. Second, the harvesting performances are evaluated, using a given piezoelectric harvester and comparing the baseline situation with the enhanced one. In image 3.10 it can be observed that the lens brings an increase in harvested output power, in particular the efficiency increases 13.2 times comparing a baseline situation with the presence of the GRIN plate. The main reported limitation of this device is, indeed, its directional dependency, as the wave needs to have a very precise propagation direction, or focusing is not triggered, as the tuning of the refractive index is performed only along y-direction, keeping it constant along x. The same authors, Tol S. et al, tried to solve this problem in another paper, where they designed a Luneburg lens, always for the specific application in energy harvesting[11]. Also in this case, the authors first described the creation of the lens, then tested its performance. Since Luneburg lenses are omnidirectional devices, they are able to focus the impinging plane wave on the diametrically opposed point of the structure independently of the wave source position, so the main problem of GRIN plates is overcome. In order to realize such design, an unit cell with hexagonal symmetry has been used. The unit cell consists of an Aluminium made hexagon with a blind hole. The authors demonstrated that, by varying the diameter of the blind hole inside the unit cell, a different speed of travelling waves inside the crystal can be obtained, as shown by the dispersion relations in figure 3.11. They proceed then to define the refractive index of elastic waves as

$$n(r) = v/v_{\Gamma M} \tag{3.3}$$

where $v_{\Gamma M}$ is the speed of travelling waves inside the medium with a certain diameter, as obtained by dispersion relations. v, on the other hand, is the speed of waves calculated in a homogeneous plate of pure material with no holes. Since $v_{\Gamma M} < v$, it is true that, for every possible diameter, n>1. Once this relationship is known, it is necessary to know at each point of the device which speed value needs to be attained. To fulfil this goal, a theoretical refractive index profile is used. Since the presented device is a Luneburg lens, the refractive index should

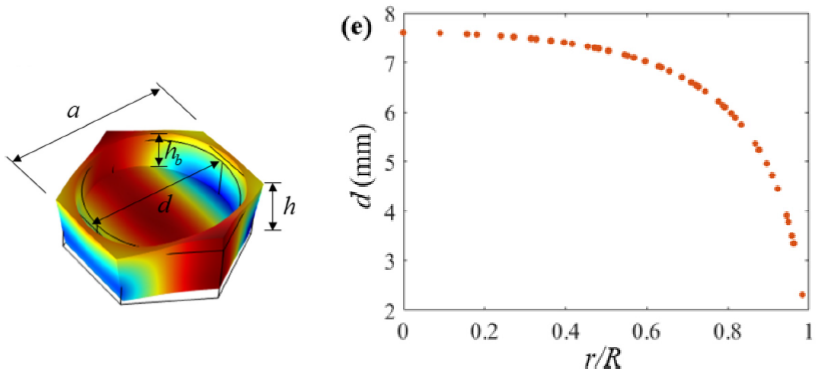

Figure 3.11: Tol S. et al, 2017[22]: Left: Graphical representation of the unit cell, characterized by hexagonal symmetry and a tunable blind hole. Right: Graph, built by the authors, which shows the correct value of diameter to use at each radial position r/R to match the refractive index value given by the lens profile.

vary radially. The employed formula is

$$n(r) = \sqrt{2 - \left(\frac{r^2}{R^2}\right)} \tag{3.4}$$

where r is the position of the selected unit cell and R is the lens radius. So, by knowing this information, the authors plotted the graph in the right of image 3.11, where the correct value of diameter for each r/R value is highlighted. Having thus finished the theoretical realization of the lens, the authors provide, in the paper, first the demonstration of its working principle, both by numerical and experimental means. Then, the illustration of the energy harvesting properties, by attachment of piezoelectric harvesters, is reported. First, for the demonstration of the working principle of the lens, numerical simulations using COMSOL Multiphysics® have been performed. The tested domain was an aluminium plate which contains the lens, excite by a sine burst load with 4

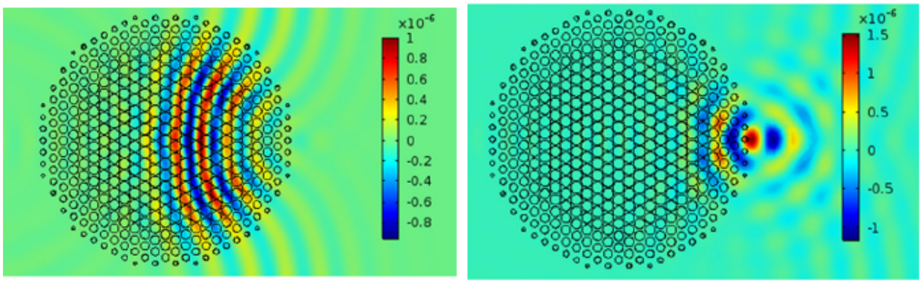

Figure 3.12: Tol S. et al, 2017[22]: Both figures show the behaviour of the numerically tested lens at two different time frames, in particular $t = 168\mu s$ for the left picture and $t = 212\mu s$ for the right image. The plotted value is the RMS wave field velocity in z direction.

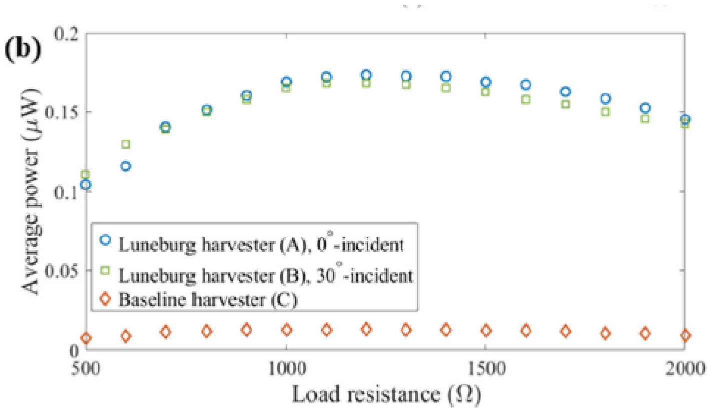

Figure 3.13: Tol S. et al, 2017[22]: Comparison between a baseline harvester and the two situations where the Luneburg lens is used. The gain between using and not using the lens is pretty clear.

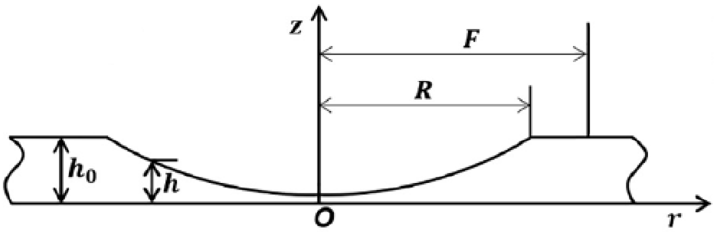

Figure 3.14: Zhao L. et al, 2020[25]: Base structure of a Luneburg lens for wave propagation control.

cycles centred at 50kHz. At the edges of the lamina absorbing boundary conditions have been implemented, in order to remove wave reflection at boundaries. Results are reported in figure 3.12, showing simulations at two different time steps. The authors noted that the phenomena is simulated correctly both via software and, performing an experiment on an aluminium plate in real life, results converge, with a focusing point located exactly at the end of the lens region, clearly visible in those images. The second step has been that of testing the performance of the harvester. For doing this, a baseline harvester has been placed both in the lens region and outside the lens region at the same distance from the line source, as illustrated in image 3.13. The idea here is to see how much the output power increases. Looking at figure 3.13, the authors reported that output power increases drastically with the usage of the lens at 50kHz. In fact, scavenged power increases 13 times. Last, an extremely recent work from Zhao L. et al is presented, who tested a different structure for a Luneburg lens and reviewed its EH capabilities[25]. In this case, the grading of the wave's velocity is performed by continuously changing the thickness of an aluminium plate, as depicted in figure 3.14. The effect is justified in the following way: the theoretical refractive index profile is estimated as

$$n(r) = \frac{\sqrt{F^2 + R^2 - r^2}}{F} \tag{3.5}$$

where F is the position of the focusing point, R the lens' radius and r the radial position of a point inside the lens. The A0 wave's phase velocity is also known as

$$c = \frac{\omega}{k} = \left(\frac{Eh^2\omega^2}{12\rho(1-\nu^2)} \right)^{\frac{1}{4}} \tag{3.6}$$

where E is the Young's modulus, ν is the Poisson's ratio and ρ is the material's density. Making the ratio between c in any point and c_0, the speed of A0 waves for an aluminium plate with thickness equal to the thickness of the external lamina it is clear that

$$n = \sqrt{\frac{h_0}{h}} \tag{3.7}$$

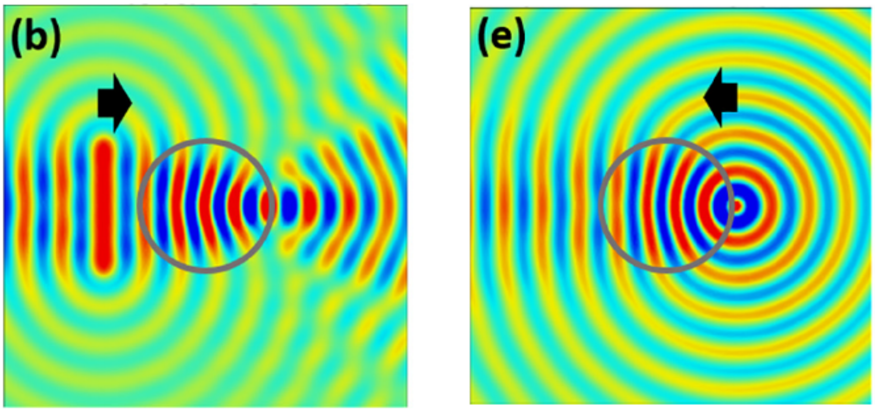

Figure 3.15: Zhao L. et al, 2020[25]: Numerical simulations show the working principle and the capability of the Luneburg lens. The lens works in two different ways, as it can be seen from the pictures. Left: A planar wavefront is localised on the diametrically opposed point. Right: A spherical wavefront is transformed into a planar one.

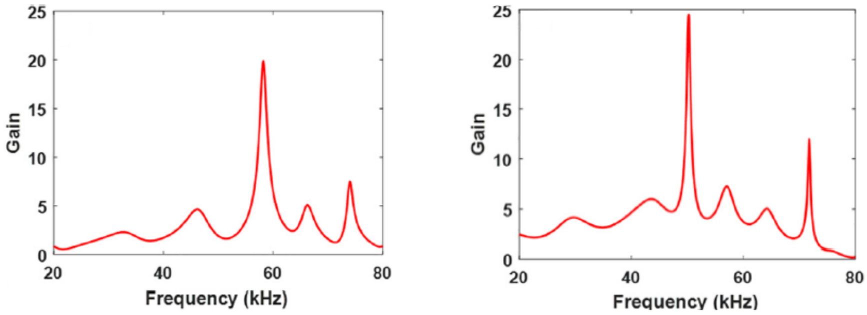

Figure 3.16: Zhao L. et al, 2020[25]: Comparison between the gain registered by left: numerical setup and right: experimental simulations.

using both the equations derived, we get

$$h(r) = \frac{h_0 F^2}{F^2 + R^2 - r^2} \tag{3.8}$$

The authors analytically studied the performance of this lens, deriving three lens types: if $F/R < 1$ the focusing point is inside the lens, if$F/R = 1$, the focusing point is at the lens' border, else is located after the lens' region. Going on to simulations, they tested the behaviour of all three types of lenses. Reporting in image 3.15 results for $F/R = 1$, the lens' behaviour is then shown. In particular, the authors demonstrated that the lens works on two opposite ways. It is able to focus plane wavefronts of A0 sound waves on the point opposite to the entrance one, fig b, but is even able to deviate spherical waves collimating them, as visible on the right image in figure 3.15. Experimental results, performed in an aluminium plate excited with piezoelectric transducers showed similar results. It has been demonstrated that the lens gives a 5x displacement magnitude increment with respect to a baseline situation. Having demonstrated its capabilities, EH is investigated next. Making both numerical and experimental investigations, the authors found that normalized voltage on a piezo harvester increases up to 300%, with peak gains of 20-24x depending on the used frequency, as shown in image.. The shift in peak is attributed, by the authors, to the discrepancy between simulation and experiment's material properties employed.

Chapter 4

GRIN lens prototype

The aim of this research project is to test different metamaterial based lenses for focusing elastic waves, in light of foreseeing a possible use in EH implementations. To achieve this goal, numerical simulations have been performed both to check their focusing capabilities and to test the potential of this peculiar application in energy harvesting. This chapter focuses on the demonstration of this goal for the GRIN lens prototype. First, in section 4.1, a deep description of the realization process is given, explaining all the steps that allowed to pass from the theoretical refractive index profile to the effective one given to the material. The subsequent part will analyse in detail the results of numerical simulations. In order to do such task, the lens will be analysed by a numerical simulation software, in particular COMSOL Multiphysics version 5.5. Frequency analyses, discussed in section 4.2, are going to be used to foresee which could be the behaviour at regime of the device for a given set of frequency. Time domain simulations, discussed in section 4.3, intend to simulate the propagation of the wave time frame by time frame, allowing to see the focusing at a precise time slot and a behaviour of the device closer to the real life one. Different materials will even be tested, with the precise purpose to control which is the influence of material properties on the displacement magnification ratio between a case where a lens is used and a case where a lens is not used.

4.1 Construction of the Lens

The GRIN lens presented in this work is built following the steps indicated by Pennec et al in their work, where a Luneburg lens and a GRIN device are tested for focusing[26],[27]. In particular, in these given set of papers the authors first go through the derivation of a model, called "Effective medium theory", which acts as a link between the ideal refractive index profile and the refractive index across the material's surface. Then, they numerically test the functioning of this device by usage of simulation software. The aim of this part will be the explanation of the effective medium theory, which will allow to construct the material with a correct refractive index profile. The aim of this theory is straightforward when looking at figure 4.1. Let's suppose to excite our real device, composed by a periodic arrangement of scatterers in a matrix and reported on the upper part of the picture, with an incident wave field ψ_0. As a consequence, the object will produce a scattered wave field ψ_{sc}, which depends on the incident field in the following way:

$$\psi_{sc} = T_{cls}\psi_0 \tag{4.1}$$

The so called T matrix of the cluster of scatterers has been introduced, which links the scattered and incident field and depends on the physical properties of the scatterers. The main object of this derivation is to demonstrate that the behaviour of these scatterers can be correctly replicated by a homogeneous material, represented in the bottom part of figure 4.1, which possesses unknown mechanical properties ρ_{eff}, ν_{eff} and D_{eff}, where D is the plate's rigidity which can be estimated as

$$D = \frac{E_b h_b^3}{12(1-\nu_b^2)} \tag{4.2}$$

In this newly conceived material it is still true that the scattered field and the incident one are linked by the T matrix, which in this case is called T_{eff}. The link between these two approaches lies in the study of the T matrix: in fact, if the excitation frequency is in the low frequency limit, it is true that

$$\lim_{\omega\to 0} T_{cls} = \lim_{\omega\to 0} T_{eff} \tag{4.3}$$

Since the left part is a known quantity, as the nature of the scatterer and their position are known, the effective T matrix can be calculated and, then, the effective material's properties, which will describe equivalently the material. In the low frequency limit, all the T matrix elements go to zero. For this reason, depending on the nature of the impinging wave, some terms will be predominant on others. Those will dictate the value of the effective material properties. For the case of elastic waves, the predominant terms are three, since we need

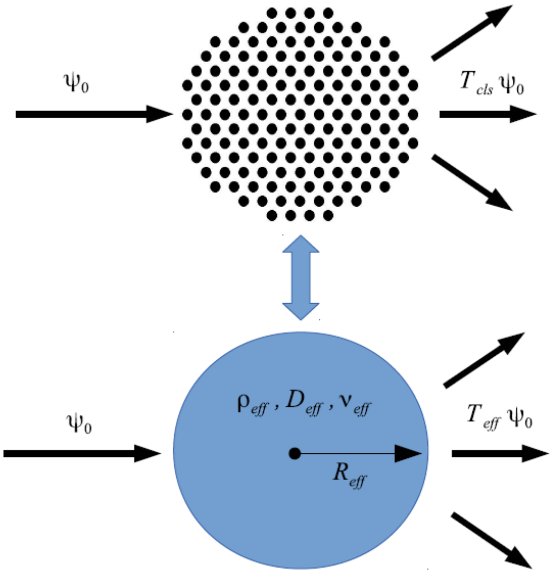

Figure 4.1: Pennec y. et al, 2014[27]: Graphical representation of the aim of the effective medium theory.

three material properties, and are T_0,T_1, and T_2. The derivation starts with another approximation: the wave field needs to have a wavelength larger than the thickness of the plate, such that this formula for wave displacement inside the material apply

$$-\frac{\partial^2}{\partial x^2}\left(D_b[\frac{\partial^2 W}{\partial x^2}+\nu_b\frac{\partial^2 W}{\partial y^2}]\right)-\frac{\partial^2}{\partial y^2}\left(D_b[\frac{\partial^2 W}{\partial y^2}+\nu_b\frac{\partial^2 W}{\partial x^2}]\right)-2\frac{\partial^2}{\partial x\partial y}\left(D_b(1-\nu_b)\frac{\partial^2 W}{\partial x\partial y}\right)=\rho h\frac{\partial^2 W}{\partial t^2} \tag{4.4}$$

Under the hypothesis that the background's parameters are constant and an harmonic time dependence on the field W is assumed, the equation can be simplified to

$$(D_b\nabla^4-\rho_b h_b\omega^2)W(x,y)=0 \tag{4.5}$$

where the incident field is expressed by

$$W_0=\sum_q[A_q^J J_q(k_b r)+A_q^I I_q(k_b r)]\exp^{iq\theta} \tag{4.6}$$

being a sum of Bessel functions of argument k_b, where

$$k_b^4=\frac{\rho_b h_b}{D_b}\omega^2 \tag{4.7}$$

On a similar manner, the scattered field and the field inside scatterers can be expressed as

$$W_{sc}=\sum_q[B_q^H H_q(k_b r)+B_q^K K_q(k_b r)]\exp^{iq\theta} \tag{4.8}$$

$$W_i=\sum_q[C_q^J J_q(k_a r)+C_q^I I_q(k_a r)]\exp^{iq\theta} \tag{4.9}$$

Next, boundary conditions are to be applied, and they give 4 equations that can be expressed as

$$X_1^0 A_q+X_q^{SC}B_q=X_q^a C_q \tag{4.10}$$

$$Y_q^0 A_q+Y_q^{SC}B_q=Y_q^a C_q \tag{4.11}$$

Matrices X^i and Y^i are 2x2 matrices, while A,B,C are vectors 2x1. Solving for C_q in one of them and substituting into the other yields, after some rearrangements,

$$B_q=-[Y_q^{SC}-Y_q^a(X_q^a)^{-1}X_q^{SC}]^{-1}\times[Y_q^0-Y_q^a(X_q^a)^{-1}X_q^0]A_q \tag{4.12}$$

Finally, form this matricial form equation, the expression which leads us to the T matrix can be obtained as

$$\begin{pmatrix}B_q^H\\B_q^K\end{pmatrix}=\begin{pmatrix}T_q^{HJ} & T_q^{HI}\\T_q^{KJ} & T_q^{KI}\end{pmatrix}\begin{pmatrix}A_q^J\\A_q^I\end{pmatrix} \tag{4.13}$$

The next step is calculating T for our case of interest. For flexural waves, that are A_0 Lamb wave modes in the plate, actually the predominant terms are only two, for $q=0$, and $q=2$. Being 2x2 matrices, though, the requirement of having still 3 independent components is preserved. It is found that

$$T_0\approx\frac{i\pi(k_b R_a)^2}{4}\begin{pmatrix}\Gamma_0^{11} & \Gamma_0^{12}\\2i/\pi\Gamma_0^{12} & 2i/\pi\Gamma_0^{11}\end{pmatrix} \tag{4.14}$$

$$T_2 \approx \frac{i\pi(k_b R_a)^2}{4}\begin{pmatrix} \Gamma_2 & \Gamma_2 \\ 2i/\pi\Gamma_2 & 2i/\pi\Gamma_2 \end{pmatrix} \tag{4.15}$$

where Γ_0^{11}, Γ_0^{12}, Γ_2 are

$$\Gamma_0^{11} = \frac{1}{2}\frac{\rho_a h_a}{\rho_b h_b} + \frac{D_b}{D_b(1-\nu_b)+D_a(1+\nu_a)} - 1 \tag{4.16}$$

$$\Gamma_0^{12} = \frac{1}{2}\frac{\rho_a h_a}{\rho_b h_b} - \frac{D_b}{D_b(1-\nu_b)+D_a(1+\nu_a)} \tag{4.17}$$

$$\Gamma_2 = \frac{1}{2}\frac{D_b(1-\nu_b)-D_a(1-\nu_a)}{D_b(3+\nu_b)+D_a(1-\nu_a)} \tag{4.18}$$

Arrived at this point, the last step is remembering that

$$\Gamma_q^{eff} = f\Gamma_q^{cls} \tag{4.19}$$

Substituting and making final rearrangements, the equations which will be exploited for effective parameter calculation are found as

$$\rho_{eff} = [1 + f(\Gamma_0^{11}+\Gamma_0^{12})]\rho_b \tag{4.20}$$

$$D_{eff}(1+\nu_{eff}) = \frac{1+\nu_b - f(\Gamma_0^{11}-\Gamma_0^{12})(1-\nu_b)}{1+f(\Gamma_0^{11}-\Gamma_0^{12})}D_b \tag{4.21}$$

$$D_{eff}(1-\nu_{eff}) = \frac{1-\nu_b-2f\Gamma_2(3+\nu_b)}{1+2f\Gamma_2} \tag{4.22}$$

The next step before proceeding with the construction of the GRIN device has been dedicated to reproduce the effect of this theory, proposed by the authors, by practically testing it to see if we manage to replicate the results presented on the paper by Pennec et al, 2016[27]. The authors tested it in three cases: Aluminium+Lead; Aluminium+Rubber, Aluminium+holes. The material properties used for the derivation are indicated in table 4.1. Using the data in these table, it has been possible to evaluate ρ_{eff}, ν_{eff}, D_{eff} and c_{eff}. Results are reported in figure 4.2 and 4.3. As is can be seen from the images, the trend for all these variables is different from one another. The only linear trend is the

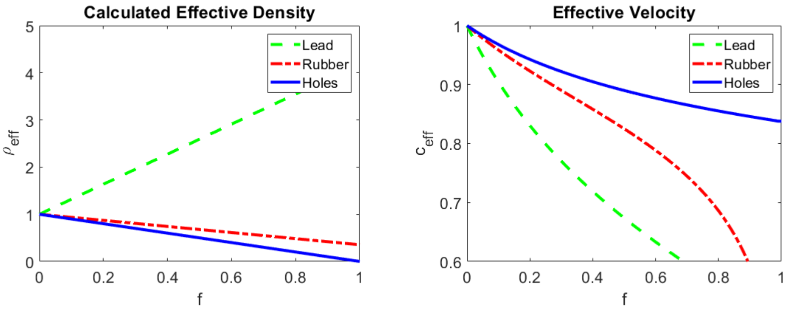

Figure 4.2: Graphical representation of the trend for effective parameters calculated by variation of the filling fraction of the inclusion. Left: effective density. Right: effective velocity.

Table 4.1: Material Properties for Aluminium, Lead and Rubber.

MATERIAL	**E [GPa]**	ν	$\rho[Kg/m^3]$
Al	70	0.35	2710
Pb	16	0.44	11340
Rubber	7e-4	0.45	960

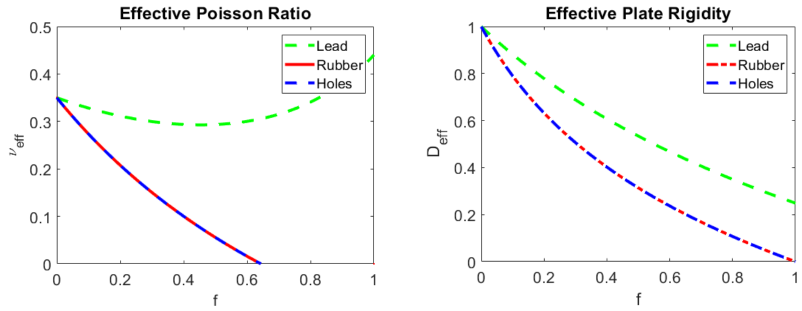

Figure 4.3: Graphical representation of the trend for effecive parameters calculated by variation of the filling fraction of the inclusion. Left: effective Poisson's ratio. Right: effective plate rigidity.

one followed by the density, which increases linearly from its value in the bulk material to its value in the inclusion as the filling fractions ranges from 0 to 1. The other variables follow a more complex trend. However, as noted before, the theory for flexural plates does not hold if the filling fraction is high, but only for low-mid filling fractions. Since our final goal is to build a GRIN device, it is mandatory to make sure that this effective material correctly reproduces elastic wave propagation in our medium. To do that, as even the authors did in one of their research projects, the dispersion relations of a crystal with a given filling fraction are to be compared with the estimated dispersion relation that this effective material provides. Let's start from the derivation of the analytical form of the dispersion relation in our effective case. If the hypothesis $\lambda > h$ still holds, it is true that the dispersion relations for lowest order Lamb modes in plates are parabolic for the antisymmetric A_0 mode. More precisely,

$$\omega = \frac{v_p h_b}{\sqrt{12}} k_A^2 \tag{4.23}$$

What is missing now is the form of v_p in the case of an effective medium. Remembering that, from previous derivations the dispersion relation for flexural waves in low frequencies is

$$\omega^2 = \frac{D}{\rho h_b} k^4 \tag{4.24}$$

For the effective material we have that

$$\omega^2 = \frac{D_{eff}}{\rho_{eff} h_b} k^4 = \frac{\bar{D}}{\bar{\rho}} \frac{E_b}{\rho_b(1-\nu_b^2)} \frac{h_b^2}{12} k^4 \tag{4.25}$$

which allows to identify v_p as

$$v_p^2 = \frac{\bar{D}}{\bar{\rho}} \frac{E_b}{\rho_b(1-\nu_b^2)} \tag{4.26}$$

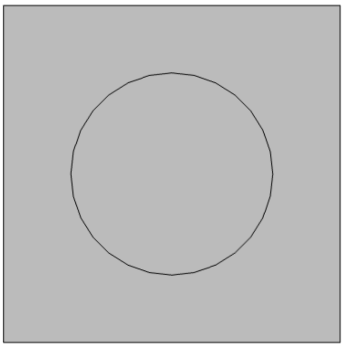

Figure 4.4: CAD representation of the unit cell employed in the construction of the GRIN lens, composed by a square with an inclusion of varying diameter.

It can be even demonstrated that the theory holds even for symmetric S_0 waves, which have an in plane motion. In fact, if the same low frequency limit is applied, for the S_0 mode it is true that

$$\omega = v_p k_S \tag{4.27}$$

Making an example with one of the materials used before, we calculate first the dispersion relation for a square-symmetry unit cell of aluminium with a lead inclusion of R=0.3a, then the dispersion relation for an aluminium matrix with a hole inclusion of the same radius, where a is the lattice constant, which means

$$f_{square} = \frac{\pi R^2}{a^2} = 0,2827 \tag{4.28}$$

A representation of the unit cell is given in figure 4.4. The out of plane thickness has been set to $h_b = 1mm$, such that low frequency conditions apply. After having calculated the value of k at the edges of the first Brillouin zone, we can calculate the trend of the dispersion relations for the effective case, reported

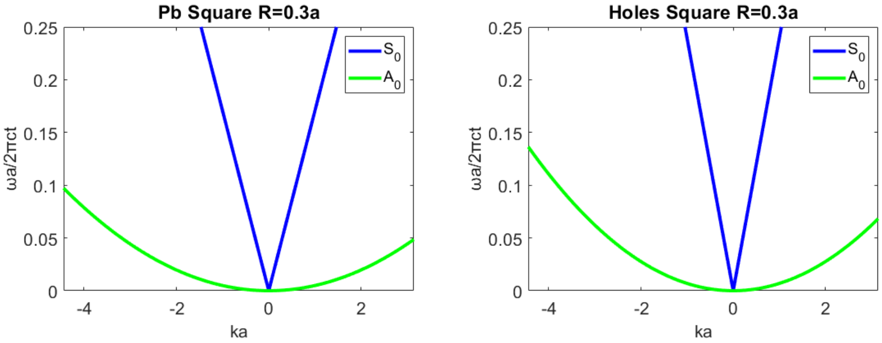

Figure 4.5: Graphical representation of the dispersion relations for A_0 and S_0 modes calculated via the guidelines given by Pennec Y, et al.[26],[27]. Left: silicon bulk material + lead inclusion of radius 3mm. Right: silicon bulk material + hollow inclusion.

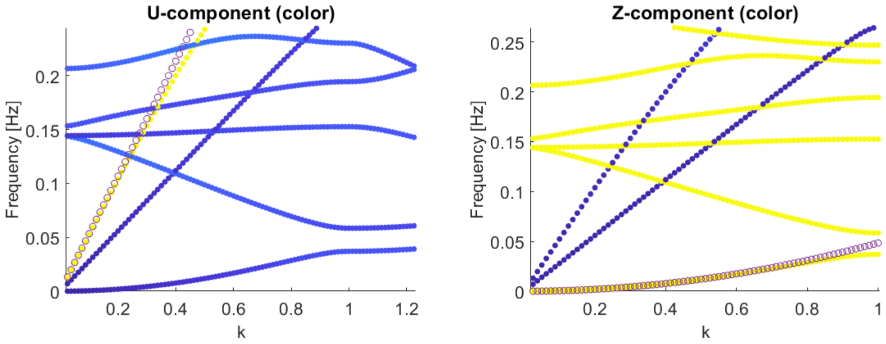

Figure 4.6: Dispersion relations calculated via numerical simulation for the unit cell represented in figure 4.4.

in figure 4.5. We can notice that in the right case the dispersion relations allow to get higher frequency values. After having done this task, a COMSOL simulation has been performed on the same unit cells to make a comparison between the real case and the effective one. An eigenfrequency simulation has been set for both cases, searching for the band structure by making a sweep of the k wavevector along the irreducible zone. The comparison between the theory and the simulation is reported, both in the case of lead and in the case of a hole inclusion, in figure 4.6. The yellow curve represents the dispersion relation calculated numerically, while the purple-dotted dispersion is the one calculated with formulas (4.23, 4.27). As the authors predicted, the agreement between the effective medium theory and the numerical simulation is very good, especially keeping the frequency low, as it has been done in the image. Some discrepancies are found at the Brillouin zone's edges but, overall, the agreement

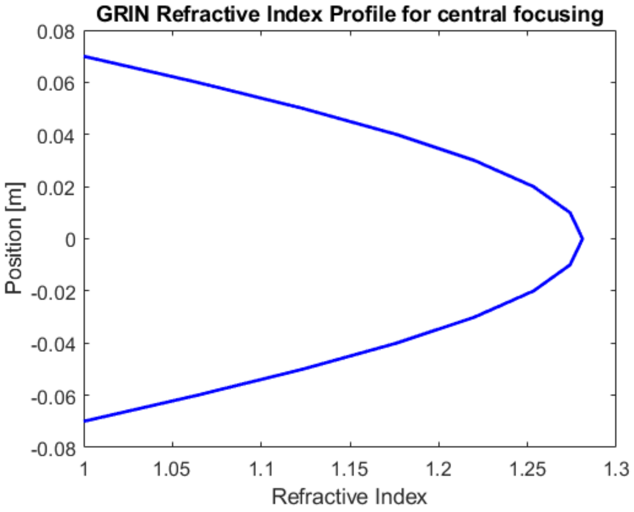

Figure 4.7: Graphical representation of the GRIN ideal refractive index profile if central focusing is wanted.

Table 4.2: Material Properties for Silicon and Lead.

MATERIAL	**E [GPa]**	ν	$\rho[Kg/m^3]$
Si	150	0.28	2330
Pb	16	0.44	11340

is very great. As such, the employment of this theory has been considered for the realization of the GRIN device since, once the effective material properties are known, the effective plate velocity for a given Lamb wave mode can be calculated and, then, the refractive index, which can be locally tailored. That is, of course, if we employ the low frequency limit and filling fractions do not grow too much. As explained in chapter 2, a GRIN plate, to focus waves on a given point, needs to have a change in the refractive index that follows the law

$$n(y) = n_0 sech(\alpha y) \tag{4.29}$$

$$\alpha = \frac{\pi}{2x} \tag{4.30}$$

where n_0, is the refractive index at the centre of the device, since is y-axis symmetric, and x is the focusing point. Let's suppose to build a GRIN plate of 30x15 unit cells. Depending on the focusing point, the refractive index profile is going to change. Supposing that the focusing point is on the centre of the device, once x is known, the theoretical refractive index profile can be derived in all the device. Then, there is the need to match this theoretical distribution to the real index of the device, so a law that tells us how the refractive index changes in the plate has to be found. However, since we are dealing with 2 different modes with two dispersion relations, actually two refractive indexes are to be modulated, one for the S_0 mode and the other for the A_0 mode. In particular

$$n_{S_0} = \frac{v_{pb}}{v_p(y)} \tag{4.31}$$

$$n_{A_0}^2 = \frac{v_{pb}}{v_p(y)} \frac{h_b}{h(y)} \tag{4.32}$$

where v_p is the plate velocity of the given material with an inclusion of unknown radius, $v_p b$ is the plate velocity of the bulk material of which the plate is composed, $h(y)$ the thickness of the plate a t a given position and h_b the thickness of the plate outside the lens zone. Building the device with the purpose of focusing A_0 and S_0 waves at the same spot, it follows that $n_{S_0} = n_{A_0}$. So, the plate velocity term can be used to tailor the speed of symmetric waves, while the thickness of the plate can be used for tailoring the speed of flexural ones. Having solved for v_p and h_b, the final step is to track back which value of f gives this plate velocity, to calculate the value of the effective parameters, to be used in the analysis. At this point, the GRIN plate can be fully built. Supposing to build the plate with silicon as a base material and lead as inclusions, table 4.2 reports the material properties employed for both pure materials, while table 4.3 reports calculated data for the construction of the device with central focusing. Now, since one of our main aim is to practically check the effectiveness of this effective theory, other devices are going to be tested, following the same guidelines. To demonstrate the focusing capabilities, two other devices with

Table 4.3: Data for Silicon and Lead GR-IN lens which focuses waves at x=15a

y[m]	**n(y)**	$v_p[m/s]$	**f**	**R[mm]**	**h[mm]**	**E [GPa]**	ν	$\rho[Kg/m^3]$
0	1.2809	6524.9	0.102	1.801	7.807	130.03	0.244	3247.70
a	1.2739	6560.7	0.099	1.778	7.850	130.50	0.245	3225.13
2a	1.2533	6668.5	0.092	1.711	7.979	131.88	0.247	3158.53
3a	1.2202	6849.5	0.080	1.596	8.195	134.12	0.251	3051.08
4a	1.1762	7105.8	0.064	1.429	8.502	137.16	0.256	2907.77
5a	1.1233	7439.9	0.045	1.196	8.902	140.90	0.263	2734.98
6a	1.0639	7855.8	0.023	0.861	9.399	145.22	0.271	2539.89
7a	1	8357.9	0	0	10	150	0.280	2330

Table 4.4: Data for Silicon and Lead GR-IN lens which focuses waves at x=12a

y[m]	**n(y)**	$v_p[m/s]$	**f**	**R[mm]**	**h[mm]**	**E [GPa]**	ν	$\rho[Kg/m^3]$
0	1.450	5764.0	0.162	2.271	6.897	115.85	0.226	3789.62
a	1.438	5813.5	0.158	2.239	6.956	116.68	0.227	3749.08
2a	1.4017	5962.7	0.145	2.148	7.134	119.01	0.231	3636.45
3a	1.3449	6214.2	0.125	1.995	7.435	122.84	0.237	3456.25
4a	1.2717	6572.4	0.099	1.771	7.864	128.11	0.245	3217.49
5a	1.1866	7043.3	0.068	1.471	8.427	134.48	0.255	2942.68
6a	1.0947	7635.1	0.035	1.048	9.135	141.88	0.267	2640.85
7a	1	8357.9	0	0	10	150	0.28	2330

Table 4.5: Data for Silicon and Lead GR-IN lens which focuses waves at x=20a

y[m]	**n(y)**	$v_p[m/s]$	**f**	**R[mm]**	**h[mm]**	**E [GPa]**	ν	$\rho[Kg/m^3]$
0	1.1550	7236.43	0.056	1.341	8.658	136.97	0.259	2839.07
1a	1.1514	7258.76	0.055	1.323	8.685	137.29	0.260	2825.55
2a	1.1409	7325.89	0.052	1.280	8.765	138.06	0.261	2794.02
3a	1.1236	7438.23	0.045	1.197	8.890	139.51	0.263	2735.45
4a	1.1002	7596.48	0.037	1.078	9.089	141.42	0.266	2658.87
5a	1.0713	7801.61	0.026	0.910	9.334	143.83	0.270	2564.26
6a	1.0376	8054.89	0.014	0.656	9.637	146.76	0.275	2451.64
7a	1	8357.89	0	0	10	150	0.28	2330

Table 4.6: Data for Silicon and holes GR-IN lens which focuses waves at x=15a

y[m]	**n(y)**	$v_p[m/s]$	**f**	**R[mm]**	**h[mm]**	**E [GPa]**	ν	$\rho[Kg/m^3]$
0	1.2809	6524.90	0.660	4.583	7.807	31.06	-0.0328	792.20
1a	1.2739	6560.71	0.635	4.496	7.85	33.76	-0.0249	850.45
2a	1.2533	6668.54	0.575	4.278	7.979	40.55	-0.005	990.25
3a	1.2202	6849.55	0.480	3.909	8.195	52.34	0.0293	1211.60
4a	1.1762	7105.75	0.363	3.399	8.502	69.03	0.0769	1484.21
5a	1.1234	7439.95	0.237	2.747	8.902	90.699	0.1364	1777.79
6a	1.0639	7855.80	0.114	1.905	9.399	117.399	0.2048	2064.38
7a	1	8357.89	0	0	10	150	0.28	2330

silicon and lead are built. In particular, the aim here is to control that a theoretical change in the focusing point is followed even by numerical simulations. More precisely, table 4.4 reports data for a GRIN device built by setting the focusing point at x=12a from the lens' left edge, while table 4.5 reports data for a GRIN device with focusing point at x=20a from the lens' left edge. After having built the device for a given couple of materials, in particular silicon and lead, one of our last aim is to check the accuracy of this model if we change the pair of materials from the one used by the authors. In particular a GRIN lens, with central focusing only, is built with silicon as base material and hollow inclusions. This particular choice has been made because, if one has to think of a possible prototype, a silicon plate with through hollow inclusions is much easier to produce that its counterpart with lead inclusions, which will be more difficult to fabricate and test in real life. Table 4.6 reports data for such GRIN device.

4.2 Frequency Domain Analysis

Having described both the working principles of GRIN lenses and the procedure used to obtain the refractive index profile from the effective medium theory, the following step is to perform analyses on such designs using a numerical simulation software, in particular, COMSOL Multiphysics. In this section the focus has been put on analysing the GRIN design in the frequency domain. When in the frequency domain, the software gives back, as result, the regime response of the system under the influence of a frequency-dependent load. In the following pages, different tests have been carried out. The first one is dedicated to the trial of the focusing capabilities of the device: to do such task a lens, made by silicon and lead, is tested with three different focusing points set (at the centre of the lens, at x=12a and x=20a), so with three different refractive index profiles. To further underline the power of the effective medium theory, each one of this device with different focusing points will be tested in two configurations: as a "layered device" and as a real one. The real device is built by drawing each single unit cell with the required inclusion diameter for the focusing effect to take place. On the other hand, the layered device has been built by creating a plate composed by different homogeneous layers with properties equal to that of the effective material. A comparison between the geometries of the two devices can be appreciated in image 4.8. If the effective material theory really holds well, it is expected that the two geometries give back similar results for all focusing positions here analysed. Then, after having reviewed focusing properties, the next effort is dedicated to demonstrate if, as teased in the theoretical section of the effective medium theory, the device shows focusing capabilities in a broad frequency span. The choice of materials used in these first tests is justified by the fact that the authors, which presented this effective medium theory, tested this exact combination, such that we should expect the devices to work properly. After having tried the exact same setup, a different pair of materials will be put in comparison, to clearly see if, first, it works as expected and, then, to see which could be the most suitable for a prototype realization. Before seeing the proper final results of the analysis, a description on the different geometry tested and how boundary conditions have been set is required. The geometry of the GRIN device, in both real and layered configurations, is a 15x30cm rectangle. To test it, it has been embedded in a silicon homogeneous plate with thickness 1cm and radius 35cm. An overview of the geometry tested can be seen in figure 4.9. The input, in the frequency domain, has been simulated

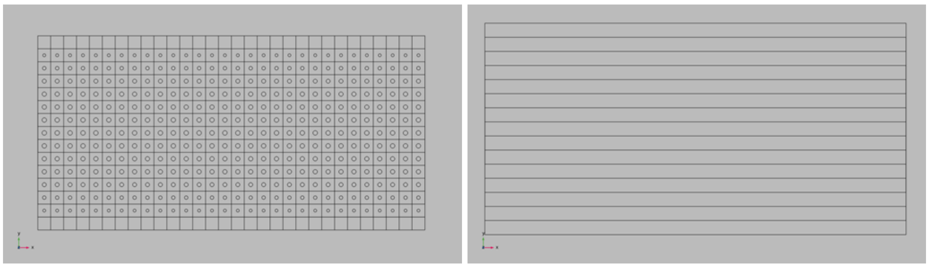

Figure 4.8: Comparison between the two GRIN devices analysed here. Left: real device. Right: layered device built thanks to the effective medium theory.

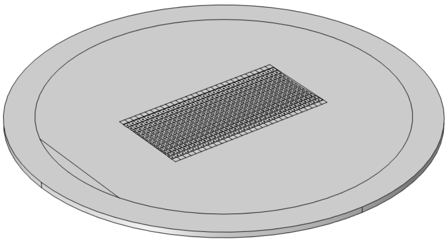

Figure 4.9: CAD representation of the whole domain used to test the GRIN lens.

as a prescribed displacement, at a given frequency, in a predetermined direction. In other words, if the aim of the test is to check the functioning of the device for the A_0 mode, a prescribed displacement in the z direction will be imposed while, for the S_0 modes the displacement will be imposed in the x direction. Of course, being in the frequency domain, imposing a fixed displacement is translated in analysing the response of a sinusoidal input with a given frequency at regime. The input has been imparted along the line highlighted in blue in figure 4.10. To generate such line, an internal cylinder of radius 30cm has been built and cut with a vertical plane distant x=-29cm from the centre of the device. The testing frequency for these devices has been selected according to the guidelines given by the authors of the text which proposed the use of the effective medium theory for these devices[26]. In particular, the authors decided to test the device

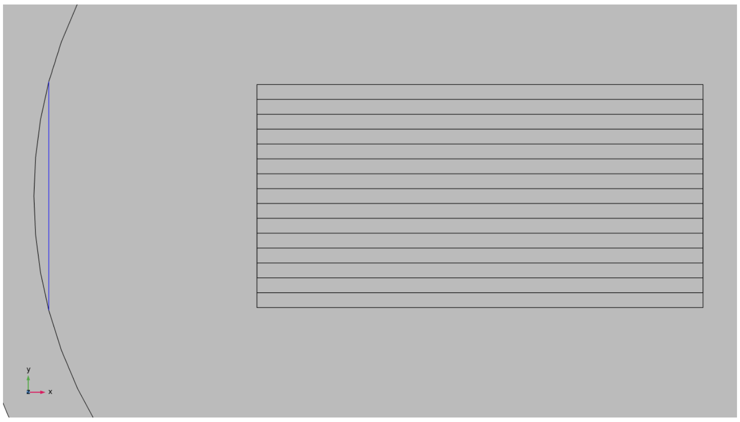

Figure 4.10: Graphical representation of the region where prescribed displacements are set.

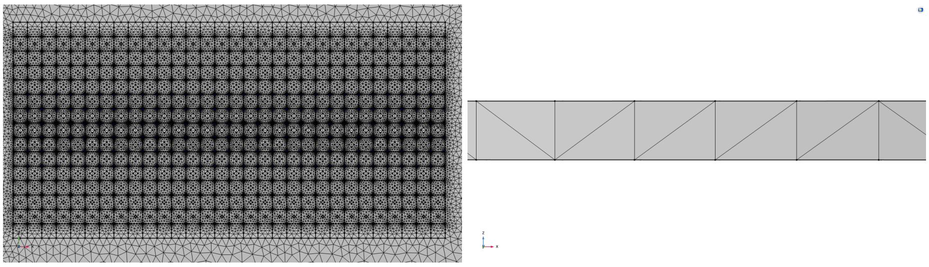

Figure 4.11: Graphical representation of the mesh used for the test of the real device.

for the A_0 and the S_0 waves at the same wavenumber $ka = 1$, meaning

$$f_{A0} = \frac{\omega}{2\pi} = \frac{v_p h_b}{2\pi\sqrt{12}} k_A^2 = 38399 Hz \tag{4.33}$$

$$f_{S0} = \frac{\omega}{2\pi} = \frac{v_p k_S}{2\pi} = 133019 Hz \tag{4.34}$$

For what concerns the applications of boundary conditions, absorbing boundary conditions have been applied along the thickness of the more external cylinder. This has been imposed with the precise purpose to eliminate reflection of incident waves at the external boundary. This allows us to concentrate on the focusing phenomena, avoiding that reflected waves perturb the reproduction of the focusing capabilities. Before starting with the overview, a final word is brought up on the different meshes used in these devices. Different devices with different focusing points have been used, so their meshes will differ slightly from one another, but the main concepts expressed here are valid for all of them. The mesh for the real device and central focusing is reported in figure 4.11. This mesh has been created by setting a "finer" element size in COMSOL Multiphysics and by building a free tetrahedral mesh on it. This leads to the pictured results. The mesh is not very refined, especially in the xy plane, but the available amount of RAM in our PC didn't allow to do better, so this is what will be used for simulations. Along the thickness of the device there is only one element, as the image clearly show, but is considered enough for our simulation. In fact, when dealing with wave phenomena, usually 6 or 7 elements per unit wavelengths are needed for the correct reproduction of results and, since our wavelength is

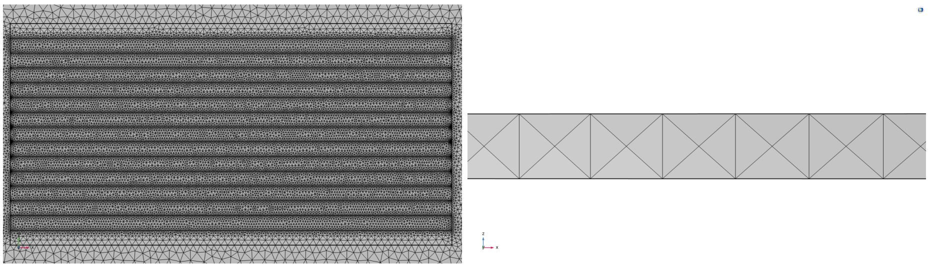

Figure 4.12: Graphical representation of the mesh used for the test of the layered geometry.

$\lambda = 6.28cm$, this limit is checked. For what concerns the mesh of the layered geometry, it is reported in figure 4.12. This time, the simpler geometry allowed to get more refinement in the xy plane. In fact, this mesh has been built by setting an "extra fine" element size in COMSOL, then another free tetrahedral mesh has been built with that setting. Along the thickness there is still only one element but, since the tested wavelength is the same for both geometries, the same conclusion is reached. Starting with the review of results, the first one presented are those of the device with central focusing (at x=35cm). We start from the analysis of the S_0 mode. In image 4.13 the surface plots, where it is plotted the absolute value of displacement in x direction, give an overview on the functioning of the device. It can be noticed that both geometries allow the phenomena to be correctly reproduced as the wave, which impinges from the left, is correctly focused at the centre of the device. To perform a more quantitative comparison between the two geometries, an ad hoc plot is reported in image 4.14, where the absolute value of displacement in the x direction is

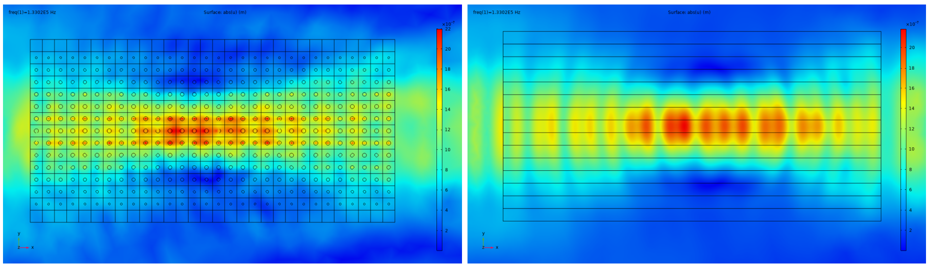

Figure 4.13: Surface plot showing the absolute value of displacement, along the x direction, for a GRIN plate which aims at focusing S_0 waves. Left: real device. Right: layered device.

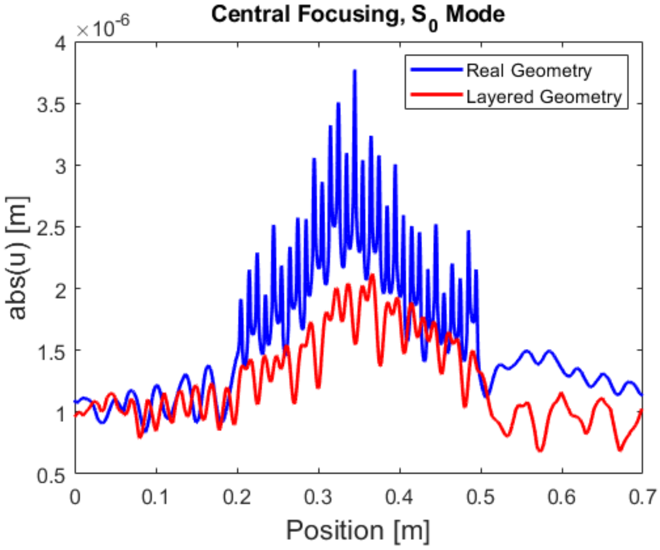

Figure 4.14: Superposition of two line plots, drawn at y=0, of the absolute value of displacement, along the x direction, for the two different geometries tested.

plotted along the y=0 line for both geometries. This allows to better compare the displacement trend across the whole domain. We can see that, although the phenomena is correctly reproduced by both designs, predicted trends are a bit different. In particular, what changes is the magnification effect of the lens. Since we are imposing a prescribed displacement with a maximum value of $1\mu m$, the lens in the real configuration gives back an amplification of 3.8x, while the layered design stops at 2.2x. Not only that, but even the position of the focusing point is different. While the real geometry places it at x=34.5cm, the layered geometry places it at x= 36.5cm, with the prediction of the real geometry much more close to the ideal configuration, which is x=35cm. Before investigating this discrepancy, we analyse the lens even with the A_0 wave, to test if the anomaly is present in both flexural and in plane waves or is limited only to one of those. In figure 4.15 the surface graphs that report the absolute value of displacement, now along the z direction, are reported for the two different geometries. Even in this case, both geometries correctly reproduce the

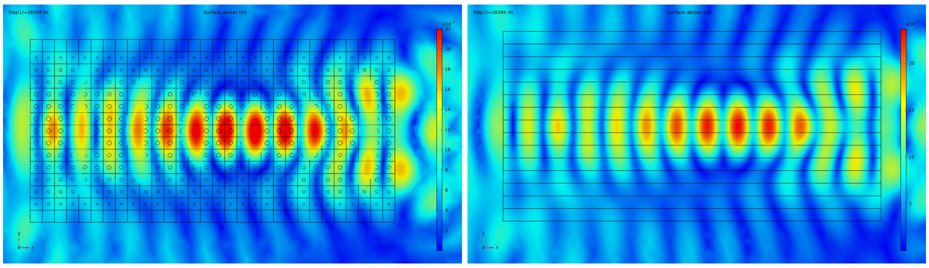

Figure 4.15: Surface plot showing the absolute value of displacement, along the z direction, for a GRIN plate which aims at focusing A_0 waves. Left: real device. Right: layered device.

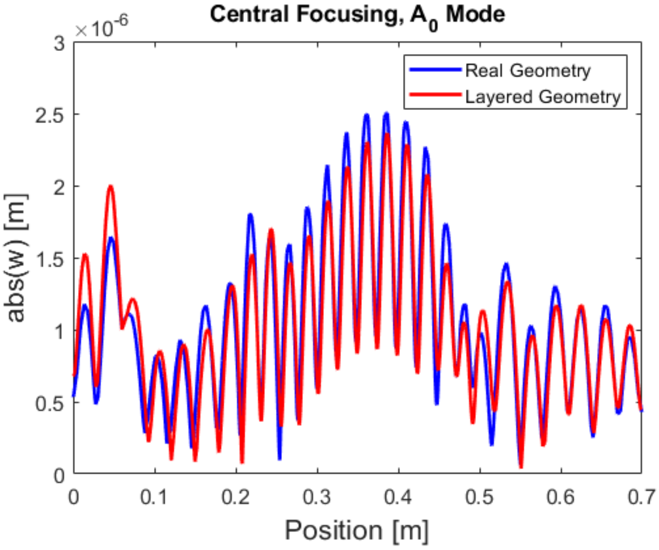

Figure 4.16: Superposition of two line plots, drawn at y=0, of the absolute value of displacement, along the x direction, for the two different geometries tested.

phenomena, as the analyses predict red spots at the centre of the device, which is correct. In this case, though, the agreement between the different analyses seem much better even by looking at this first plot. For more precise assessments, a plot which compares the absolute value of displacement, along the y=0 line, for both geometries is reported in figure 4.16. Here it can be noticed that practically the two designs report the same expected results, with almost no discrepancy in displacement magnification, which is set at 2.5x. Even more appreciated is the fact that the expected focusing point is the same in both cases, with the peak positioned at x=36cm. Having registered this profound discrepancy between analyses of the S_0 and A_0 waves, before going on testing the other devices a reflection will be brought on the possible reason for that. Of course the two geometries are different, but the main point of using those two configurations is exactly for them to reach convergence and report similar results. While this is clearly true for the A_0 mode, it is not for the S_0 mode. An explanation could lie in the accuracy of the mesh. In particular, while the analysis with the A_0 wave could be at regime, maybe the ones with the S_0 mode are simply just not. This is supported even by the fact that the two geometries share the same amount of finite elements along the thickness, which should influence flexural A_0 wave propagation, while the number along the plane is different. To further confirm this hypothesis or not, we try building an alternative mesh on the layered device, since the simpler geometry should allow better refinement. The new mesh is composed by extruded elements rather than free tetrahedral elements, to further increase element density along the thickness. A comparison between the two meshes built with the layered geometry device is proposed in image 4.17. It can be noticed that the mesh used up to this point has only one element along the thickness of the device, which is not much but, as already noted, sufficient to satisfy the limit of at least 6 finite elements per tested wavelength. On the right, the exactly opposite situation is represented, where 13 elements are placed along the thickness of the device. The number is so high for a question of need. In particular, to build this mesh the software required to slice the geometry for every different height of the central lens, as each layer has its own height which triggers A_0 focusing. This constraints the lens to already have 8 elements in a region of 1.5mm over the total thickness of 1cm. In the remaining region, 5 elements are placed. The analysis have been performed with the same boundary conditions and the same prescribed displacement as before. In figure 4.18 the absolute value of displacement, over the y=0 line,

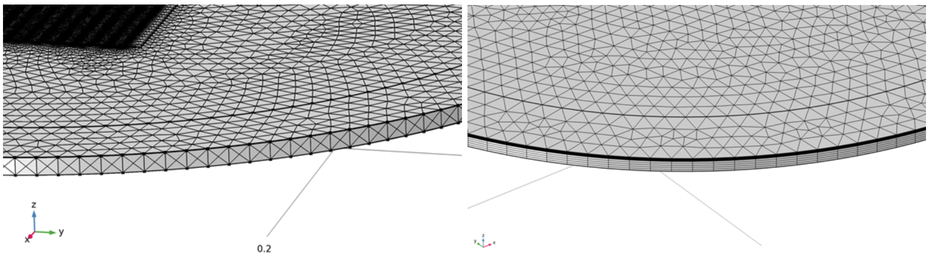

Figure 4.17: Overview of the density of elements, along the thickness of the device, for the two different meshes used in the simulation. Left: old mesh. Right: new mesh.

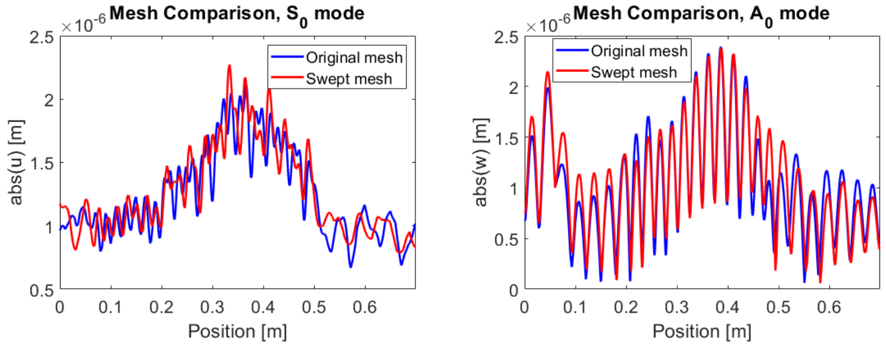

Figure 4.18: Comparison between different line plots of absolute value of displacement obtained via the usage of different meshes. The left figure shows the comparison for the S_0 mode, while the comparison for the A_0 mode is displayed on the right.

is plotted and compared for both the new and the old mesh over the S_0 case on the left and the A_0 case on the right. The main differences can, again, be noted for the S_0 case. In fact, the A_0 analysis shows a satisfying level of agreement, both in terms of displacement magnification and focusing point accuracy, even with this high difference in finite elements along the z direction. This level of accuracy is not reached for S_0 analysis. To a certain extent, the analysis worsened, as the displacement peak is placed at a coordinate x=32.5cm. This confirms the initial suspect: A_0 waves accuracy is influenced by the amount of elements in the thickness. Being both the old and new mesh at convergence, no crucial discrepancies are revealed. This is not true for the S_0 wave propagation simulation. In this case, the limiting factor is the density of elements along the xy plane, which changes much more across different meshes, hence the more relevant differences. So, if we try to make the mesh denser in the xy plane for the layered geometry, instead of making it denser along the thickness,

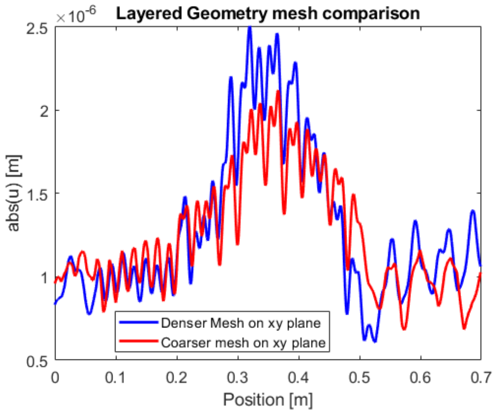

Figure 4.19: Superposition of two line plots, drawn at y=0, of the absolute value of displacement, along the x direction, for two different tested meshes on the layered geometries.

pushing it to the limit supported by our computer, the situation should better even for S_0 waves. Results for this test are reported in figure 4.19. As predicted, the analysis changed a bit, but the overall behaviour of the device has not changed dramatically. There, it can be noticed that the main difference lies in the amplification factor predicted, which changes from 2.2x in the original mesh, represented in red, to a 2.5x for this new denser mesh in the xy plane. Having confirmed that the layered geometry mesh is at perfect convergence for A_0 mode and reproduces results which are reliable for the S_0 mode, the next step to better the comparison would be, of course, to test if a refinement in the xy plane for the real mesh betters the problem of discrepancy. Sadly, for performing this operation a higher quantitative of RAM is needed on the pc used for simulations, so this last test could not be performed for the final confirmation. Having concluded with the design which proposes focusing at the centre of the device, the next test is to shift the focusing point on the left, to x=32cm. Due to the need of focusing waves before the middle point, the refractive index changes more abruptly between subsequent layers, with thickness and diameter variations which will be more pronounced, compared to the previous case. The analysis still is based in the frequency domain and has the same prescribed displacement and absorbing boundary condition applied. Having already discussed the effectiveness of each different meshes, here the ones that have been found optimal in the previous case are reused, to ensure accuracy and to make more fair the comparison between different focusing points. In image 4.20 the results for the S_0 mode are reported, where the surface plot for the absolute value of displacement along the x direction is shown, on the left for the real geometry and on the right for the layered one. The phenomena is correctly reproduced even in this case. The focusing point shifts on the left, as it was intended, for both cases, highlighting that the theoretical shift in focusing point is followed by a practical one, which is a remarkable result not highlighted in the paper with a correspondent numerical analysis. To make a more precise comparison, figure 4.21 reports the superposition between line plots of the absolute value of displacement, registered along the line y=0, for both geometries. This graph, though, shows even greater discrepancies than the previous one drawn for the central focusing case for the S_0 mode. In particular, the accuracy is better for the layered case, where the focusing point is estimated around x=33cm against the theoretical x=32cm. The real device, on the other hand, places the focusing point at x=28cm, further from the ideal position. On the other hand, the

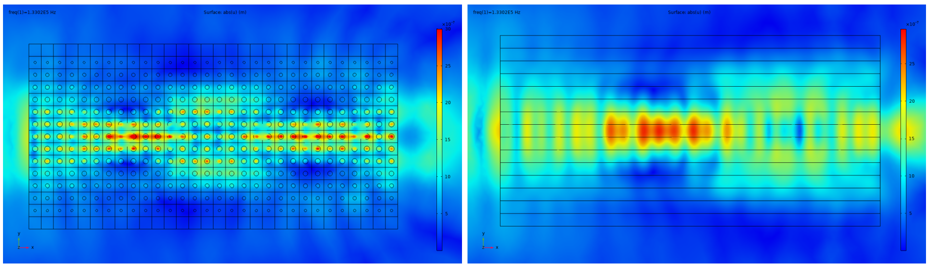

Figure 4.20: Surface plot showing the absolute value of displacement, along the x direction, for a GRIN plate which aims at focusing S_0 waves at x=32cm. Left: real device. Right: layered device.

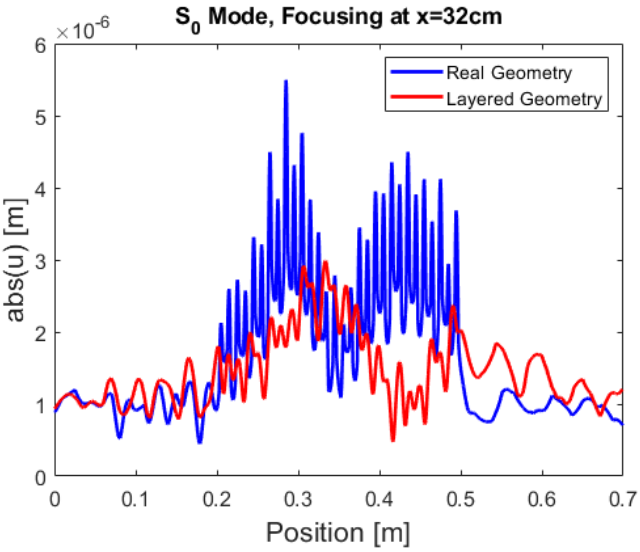

Figure 4.21: Comparison of line plots of absolute value of displacement, computed at y=0, for the device which focuses S_0 waves at x=32cm.

amplitude of displacement is greater in the real case, with almost a 6x magnification with respect to the maximum amplitude of the sinusoidal input given, compared to the layered geometry amplification, which stops at 3x. It is to be noted that, however, a similar problem with displacement amplification was detected even for the central focusing case, probably due to the poorly refined mesh in the real geometry. Having discussed the performances for the S_0 wave propagation case when the focusing point is changed, the same review is done for the A_0 wave propagation. In figure 4.22 the surface plot which reports the absolute value of displacement for the real and layered case are reported. From this graphs, it can be noticed that the shift in focusing point is correctly reproduced even for A_0 waves. In figure 4.23 the graph which superimposes the line plot of absolute value of displacement at y=0 for both real and layered case is reported. In particular, it is found that the accuracy of reproduction of the focusing point is very great, with an estimated point of x=31.5cm. The over-

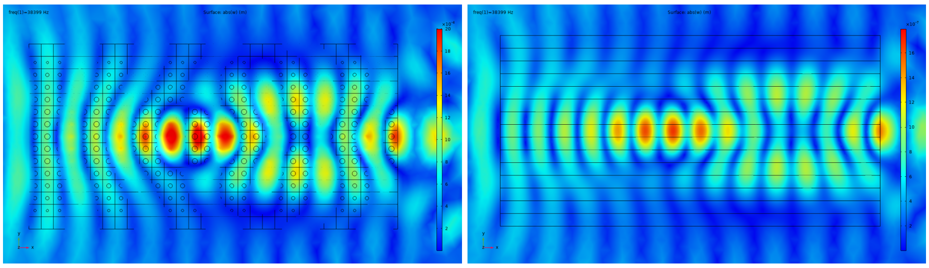

Figure 4.22: Surface plot showing the absolute value of displacement, along the z direction, for a GRIN plate which aims at focusing A_0 waves at x=32cm. Left: real device. Right: layered device.

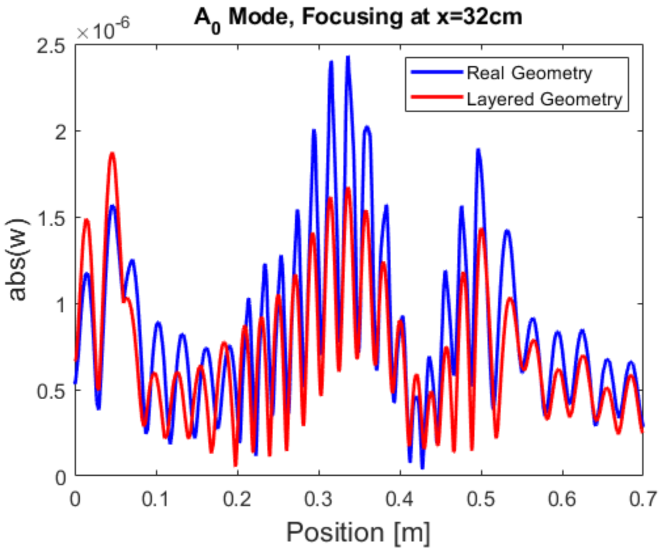

Figure 4.23: Comparison of line plots of absolute value of displacement, computed at y=0, for the device which focuses A_0 waves at x=32cm.

all very great accuracy of result reproduction for the A_0 mode was underlined even for the device with central focusing. This time though, the amplitude of displacement is a bit different even here, with a higher 2.4x magnification predicted by the real geometry, compared to the 1.6x predicted by the layered one. Overall, though, the flexural A_0 mode is still better simulated than the radial in plane S_0 one, probably due to the mesh problems already cited before. The last device which has to be tested is the one where the focusing point is moved to x=40cm, so waves are supposed to be focused after the centre of the device. To obtain this effect, the refractive index needs to vary more mildly between layers. Translated in simpler terms, this means that both the thickness of the unit cells and the inclusions' diameters variations between subsequent layers are going to be smaller that for the central case, so tolerances here are going to be crucial. Again, the boundary conditions and the prescribed displacement imposed are still the same. Starting, as always, from S_0 waves, figure 4.24 reports surface

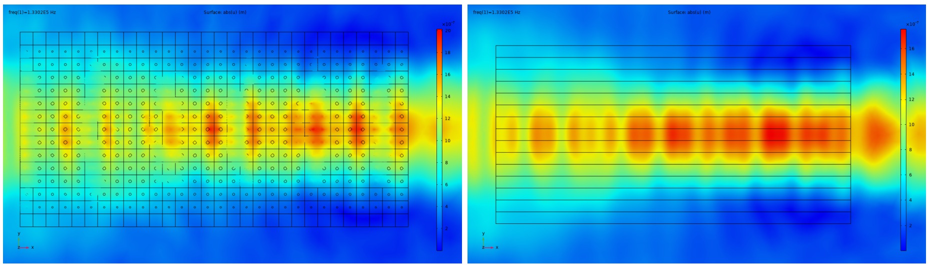

Figure 4.24: Surface plot showing the absolute value of displacement, along the x direction, for a GRIN plate which aims at focusing S_0 waves at x=40cm. Left: real device. Right: layered device.

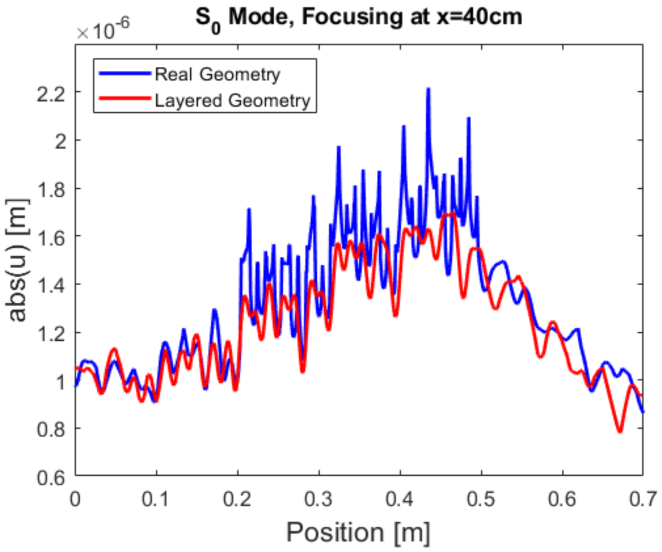

Figure 4.25: Comparison of line plots of absolute value of displacement, computed at y=0, for the device which focuses S_0 waves at x=40cm.

plots of the absolute value of displacement for the two different geometries. On the left the reported results are for the real device, while results on the right are for the layered one. This time, though, the phenomena is reproduced with a far worse accuracy in both designs. Although it does not appear as clear by looking only at the surface plots of displacement, it becomes more visible in figure 4.25, where the line plot of absolute value of displacement, along the y=0 line, is reported for both cases. In fact, here it can be noticed that the accuracy of reproduction of the focusing point is decreased. The layered device places it at x=45cm in spite of x=40cm, while the real device performs even worse, placing it at x=50cm. Again, even the amplification of displacement, with respect to the maximum amplitude given by the input, is different. The real device manages, even here, to grasp a greater magnification at 2x, compared to the 1.6x of the layered one, so overall pretty mild amplifications are registered. Before taking final conclusions even on this design, the performances of the A_0 waves

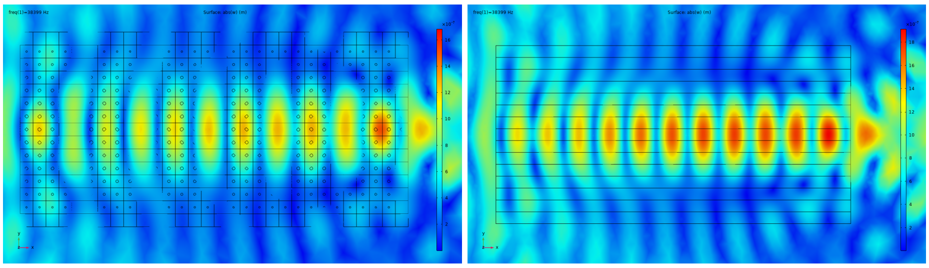

Figure 4.26: Surface plot showing the absolute value of displacement, along the x direction, for a GRIN plate which aims at focusing A_0 waves at x=40cm. Left: real device. Right: layered device.

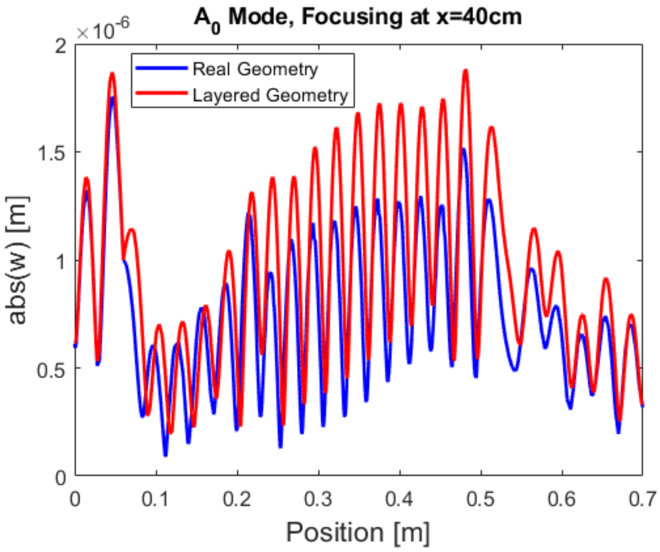

Figure 4.27: Comparison of line plots of absolute value of displacement, computed at y=0, for the device which focuses A_0 waves at x=40cm.

are reviewed. In figure 4.26 the surface plot which reports the absolute value of displacement in the out of plane direction is reported. On the left the real device is shown, while on the right the layered one is reported. In this case, there are some major problems even for the A_0 mode, already clearly visible from the surface plots, which fail to show clearly a displacement concentration in one precise spot over the geometry of the device. Again, let's refer to the line plot graph comparison, reported in figure 4.27, which allows to make more quantitative considerations. First, it can be noticed that the two analysis are much similar: in fact, a part from a small difference in maximum displacement value reached, which is very minimal however, the two analysis are comparable. The problem here lies in the ability of the numerical simulation to correctly represent the phenomena, which fades. This can be evinced by noticing that there is no clear peak in those graphs, while the behaviour of the lens is pretty flat overall. Not only this but, actually, we have that the maximum amplitude of displacement is reached outside the lens zone for both cases, so it cannot be attributed to the lens' amplification characteristics. As such, since numerical simulations have failed either to correctly reproduce the phenomena in this last device or to give substantial magnification effects, both for the S_0 and A_0 wave, we can conclude that this last prototype does not work as intended. The reason for this behaviour is attributed to the dimension of inclusions' diameters and different layers' thicknesses variations. Due to the focusing point being placed farther away from the device's centre, as it has been pointed out before, we have to use smaller inclusions and smaller height variations. Being the variations between a layer and the other very small, in the order of μm for both radiuses and diameters, a possible explanations is that those variations are too small for the phenomena to be correctly reproduced. This is even supported by the reported analysis, which show an almost flat behaviour, which seems suggesting that the device is made of evenly built layers. Then, even if such device worked, the very strict tolerances would have made it very hard to make. Briefly concluding this part dedicated to focusing properties, it can be stated that the best design is the one that allows to focus waves at the centre of the device. There, especially for the flexural A_0 waves, the agreement between the two tested geometries is almost perfect. The device which focuses waves before the centre is good and works as intended, though with general less precision. The last device, as noted, does not work as expected. Next, before analysing different couples of materials, efforts have been employed in the reproduction of the validity range for the GRIN lens. The authors, which described in their work the "effective medium theory", reported two limits in wavelength for this kind of devices to work properly[26]. The maximum working wavelength, so the minimum frequency, is set such that the wave should be smaller than the device's dimensions, not to have diffractive effects predominate over refraction. For ensuring this in our case

$$\lambda \leq 15a \tag{4.35}$$

On the other hand the minimum working wavelength, so the maximum working frequency, is set such that the wave has to be higher that at least 3 or 4 unit cells. This limit is strictly related to the effective medium theory requirements which, for working properly, requires a low frequency limit to be applied. Otherwise, the homogeneous approximation does not hold correctly. This can be translated into

$$\lambda \geq 3a \tag{4.36}$$

Remembering that, for the S_0 and the A_0 the dispersion relation is different, in particular

$$f_{A0} = \frac{\omega}{2\pi} = \frac{v_p h_b}{2\pi\sqrt{12}} k_A^2 \tag{4.37}$$

$$f_{S0} = \frac{\omega}{2\pi} = \frac{v_p k_S}{2\pi} \tag{4.38}$$

it follows that the ranges for flexural A_0 waves and symmetric S_0 waves will be different. For each device working with A_0 waves, this means that $7kHz < f < 170kHz$ while, for each device working with S_0 waves, this means that $55kHz < f < 280kHz$. Our next goal will be to test this ranges, to see if the effective medium theory holds correctly and if the real and homogeneous devices report similar working ranges. Having already concluded that the best device for focusing is the one with central focusing, the analysis will be proposed only for such prototype. Simulations have been conducted in the frequency domain with the same settings already mentioned before. The only difference is that now we make a sweep for different frequencies with a step of 2.5kHz to search the limit of validity predicted by numerical software. The first tested range will be the S_0 range. Starting the overview with the real geometry, results of the analysis indicate a much more shallow range, which shows the correct functioning for frequencies between $110kHz < f < 150kHz$. Although this device does show that more than a single frequency can be used for focusing, which is indeed a very appealing characteristic for a possible prototype, we are far from the complete range theorized by the authors. The analysis of the lowest functioning frequency is reported in figure 4.28. Here, in particular, it can be noticed that, even if the device works and simulates a gradual displacement amplification, the simulated maximum point is heavily shifted from its theoretical position of x=35cm, being collocated at x=39.5cm. The magnification effect is good, with a 2.5x with

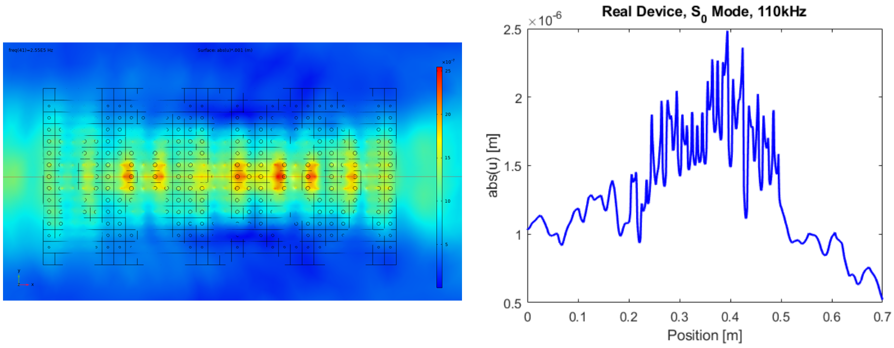

Figure 4.28: Plots of the absolute value of displacement, along the x direction, for the Si+Pb real device testing the S_0 mode at f=110kHz.

respect to the maximum amplitude of the given input. The higher frequency limit for the real device and the S_0 mode is reported in figure 4.29. In this case, the overall predicted trend agrees better with theoretical derivations. In fact, even here we have gradual amplification of displacement toward the simulated maximum, placed at x=36.5cm, so less far from the theoretical point than in the previous analysis. The displacement magnification effect is registered as 3x. Outside this range, the behaviour worsens badly. To practically demonstrate this, figure 4.30 reports the line plot of absolute value of displacement, drawn at y=0, at the frequencies correspondent to the theoretical limits. It is pretty clear that, in both cases, the device fails to correctly simulate the intended behaviour. In the theoretical low frequency limit, plotted here in green, the behaviour becomes completely flat, with no focusing detected at all. In the theoretical high frequency limit, reported here in the light blue plot, the device also fails to catch the correct behaviour, with peaks arising in zones where they are not supposed to be present. Before making final conclusions on the functioning of the S_0 range, the analysis of the device with layered geometry is reported. What strikes the most here is that the frequency range is much more wider. In fact, the device works as intended for frequencies $115kHz < f < 252kHz$. The minimum working frequency is similar to the one detected by the real de-

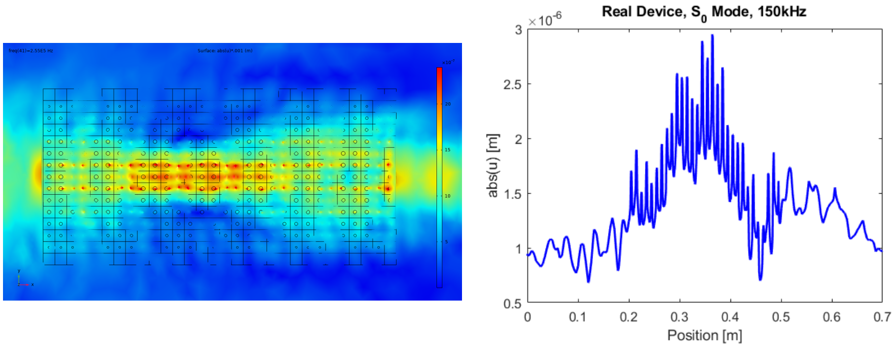

Figure 4.29: Plots of the absolute value of displacement, along the x direction, for the Si+Pb real device testing the S_0 mode at f=150kHz.

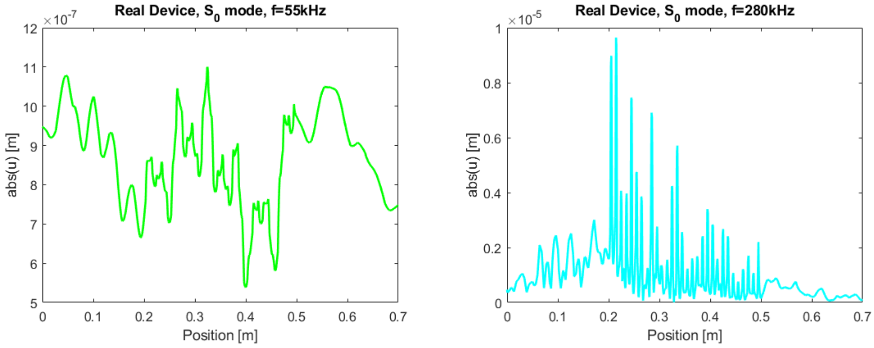

Figure 4.30: Line plots of absolute value of displacement, along the x direction and taken at y=0, for the Si+Pb real device testing S_0 waves at frequencies correspondent to theoretical frequency limits. Left: 55kHz. Right: 280kHz.

vice even before, and its results are reported in figure 4.31. It can be noticed that the focusing point is reached by gradual amplification, which is a good reproduction of the phenomena. The maximum amplitude of displacement is achieved at x=37cm, so on the right from the theoretical point, and the amplification factor is not that wide, stopping at 2.2x. However, this was true even for the real geometry, so the two geometries show similar results for the low limit in frequency. The higher limit, on the other hand, is almost completely matched. Some upper frequencies are missing, but still theory is much better reproduced here than it was in the real device. Figure 4.32 reports results for that limit, found to be f=252kHz. At this frequency the focusing behaviour is still present, but some problems are starting to show in the analysis. The maximum is reached, precisely, at x=34cm, with an almost 3.4x magnification effect with respect to the maximum amplitude of the given input. The fact that the device is starting to show its limits, though, is represented by the fact that, both in correspondence to the entrance and the exit of the GRIN lens, peaks arise, which should not be there. Not only that, but the displacement magnification effect registered there is not even negligible, almost matching that of the central peak. To demonstrate, even in this case, that the original range is

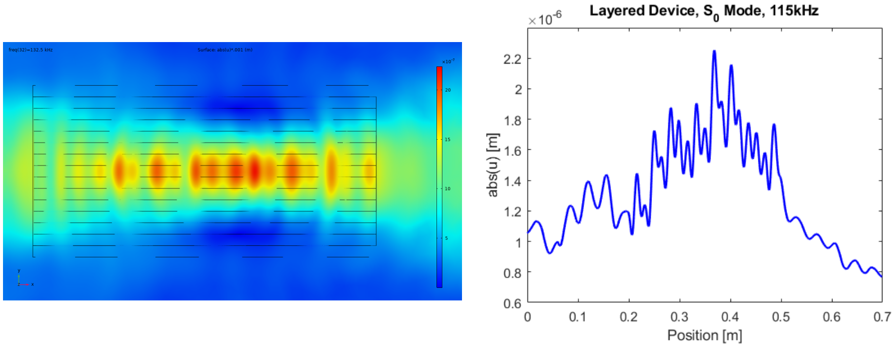

Figure 4.31: Plots of the absolute value of displacement, along the x direction, for the Si + Pb layered device testing the S_0 mode at f=115kHz.

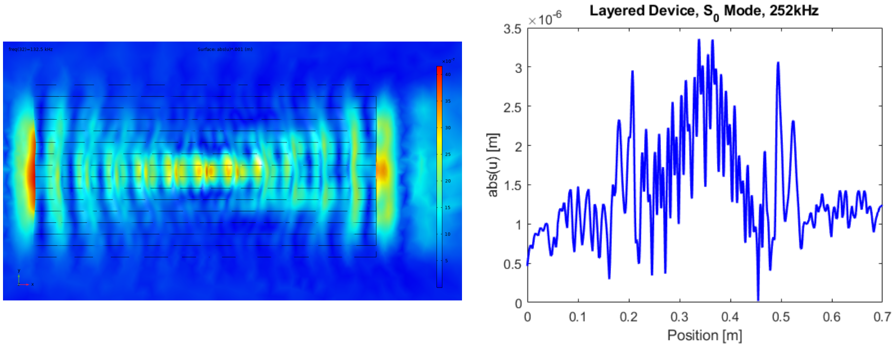

Figure 4.32: Plots of the absolute value of displacement, along the x direction, for the Si+Pb layered device testing the S_0 mode at f=252kHz.

not completely matched, figure 4.33 reports the line plot of absolute value of displacement, drawn at y=0, for the frequency limits predicted by the theory. The theoretical low limit, reported in the green graph, shows the same problem highlighted before for the real device, as the simulation completely fails to grasp the behaviour of the lens. This time though, on the theoretical upper frequency limit, the behaviour is somewhat caught, as a maximum is registered at coordinate x=36.5cm, with an overall displacement trend which resembles the correct one. The reason for which the upper frequency limit was trimmed to 252kHz lies in the fact that some frequencies, between 252kHz and 265kHz, didn't allow the phenomena to be grasped. To conclude this analysis on the S_0 range, table 4.7 reports a comparison between the frequency limits found by numerical software and the ones found by theoretical derivations. While the lower limit in frequency is not matched by either geometries, the upper one is much better represented by the layered geometry. In particular, results of the layered device are very good if we put them in perspective by calculating the wavelength at which the frequency found corresponds. Computing it for $f = 252kHz$ results in $\lambda = 3,32a$. This is, however, still in line with what the authors said, as they predicted a minimum wavelength of either 3 or 4 unit cells. This proves

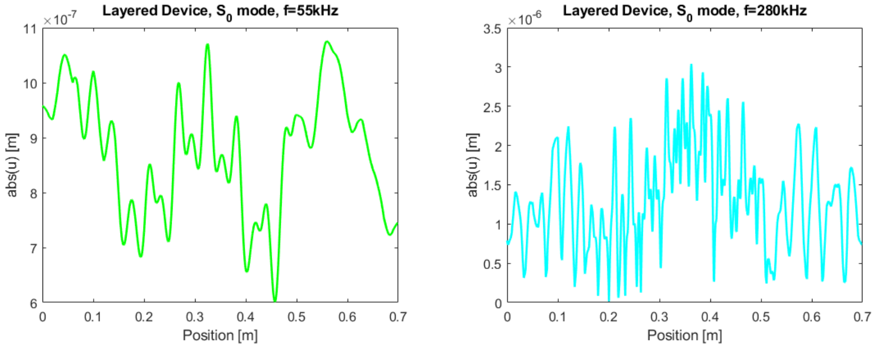

Figure 4.33: Line plots of absolute value of displacement, along the x direction and taken at y=0, for the Si+Pb layered device testing S_0 waves at frequencies correspondent to theoretical frequency limits. Left: 55kHz. Right: 280kHz.

Table 4.7: Comparison between theoretical ranges and discovered ones, for the S_0 mode, on the Silicon and Lead device focusing waves at the centre.

Theoretical Range	**Real Geometry**	**Layered Geometry**
55kHz<f<280kHz	110kHz<f<150kHz	115kHz<f<252kHz

that, at least for S_0 waves on the layered geometry, the found limit of roughly $\lambda > 3.3a$ fits with theoretical derivations. For the real device the upper limit in frequency falls around $\lambda = 5.5a$, so less promising. For the minimum frequency, so the maximum wavelength, both devices predict a frequency around 110kHz, which can be translated to $\lambda = 7.5a$, exactly half the theoretical limit. The last conclusion is that, again, the real device accounts for phenomena in a less elegant and precise way than the effective device but, again, this is probably due to a more coarse mesh employed in such case. Concluded the discussion on S_0 waves, the same comparison is made for the A_0 wave propagation. As before, the comparison starts from the analysis of the device with real geometry which, again, predicts a range of frequencies shallower than the theoretical one. Figure 4.34 reports results for the found minimum limit, which is 20kHz. Looking at the aforementioned graphs, it can be noticed that the device works, but with some remarks to be made. The focusing point is placed around the theoretical position, being located at x=36cm, so a good fit is found. However, the amplification effect is much less striking. In fact, in the left image it can be appreciated that the red zone, indicating higher displacement magnitudes, is much more spread over the whole lens. Even the line plot confirms that the amplification effect is present, but the difference in peak heights inside the device is not that remarkable. Having acknowledged this behaviour, the one at the upper frequency limit is described, reported in figure 4.35, which is found to be 90kHz. Here, the focusing point is concentrated in a smaller area, located at a coordinate x=33cm. The most impressive result here is the displacement amplification factor, which reaches 5x, a very promising result. The trend inside the device is even good, as the maximum amplitude reached at the device's centre overcomes strongly the displacement trend in other points of the device, as it should be. To further demonstrate that the theoretical limit is not matched by the analysis, simulations made at the frequencies belonging to the theoretical

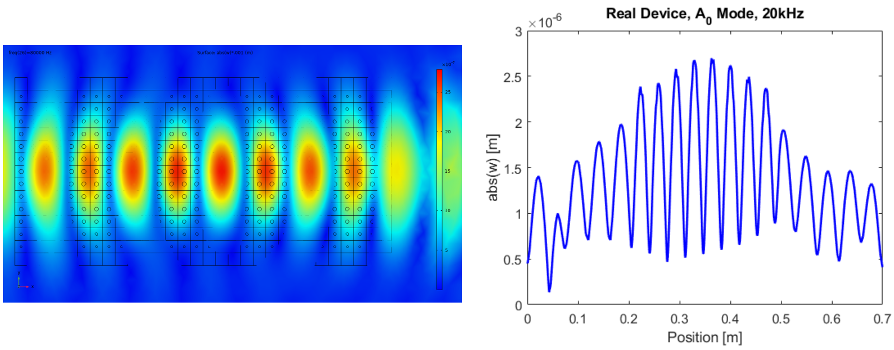

Figure 4.34: Plots of the absolute value of displacement, along the z direction, for the Si+Pb real device testing the A_0 mode at f=20kHz.

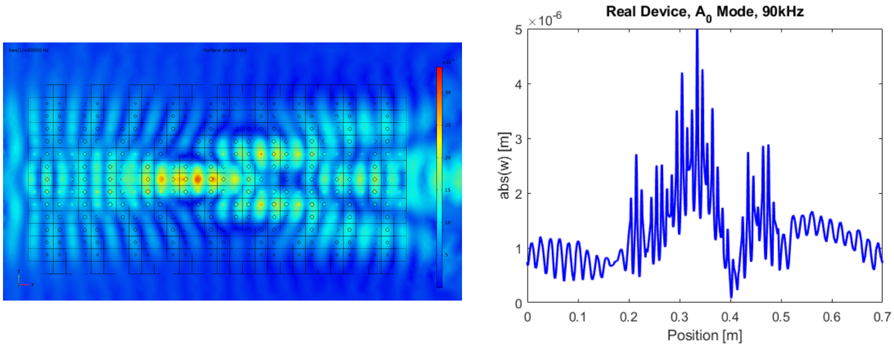

Figure 4.35: Plots of the absolute value of displacement, along the z direction, for the Si+Pb real device testing the A_0 mode at f=90kHz.

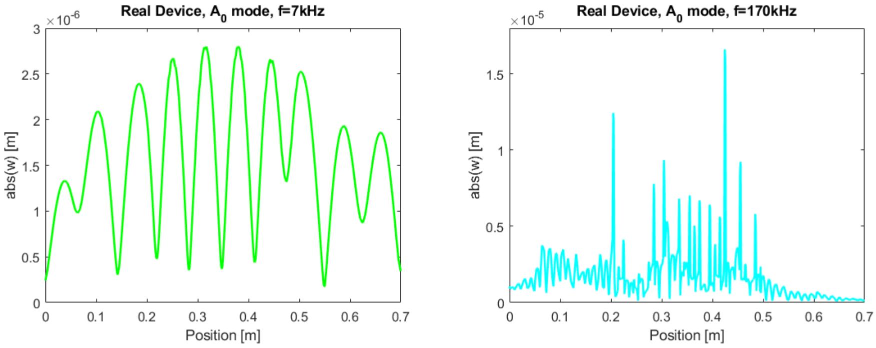

Figure 4.36: Line plots of absolute value of displacement, along the z direction and taken at y=0, for the Si+Pb real device testing A_0 waves at frequencies correspondent to theoretical frequency limits. Left: 7kHz. Right: 170kHz.

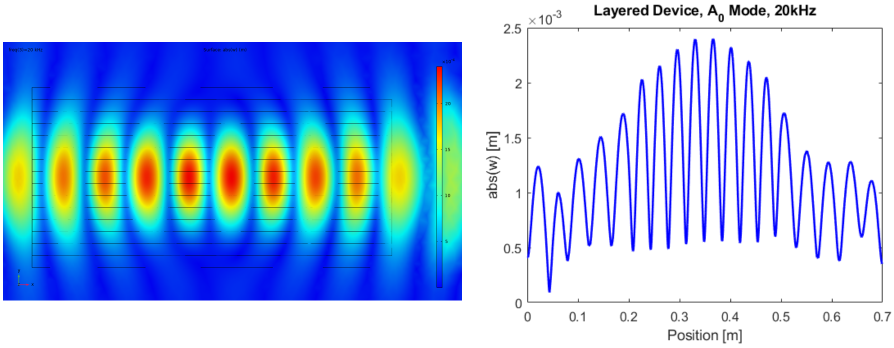

Figure 4.37: Plots of the absolute value of displacement, along the z direction, for the Si+Pb layered device testing the A_0 mode at f=20kHz.

range are reported in figure 4.36. The low frequency limit, reported in the green graph, shows the correct behaviour, although the effect is spread over a larger area. The range has been reduced, though, because some frequencies between the theoretical limit and the reported one completely diverge from the intended

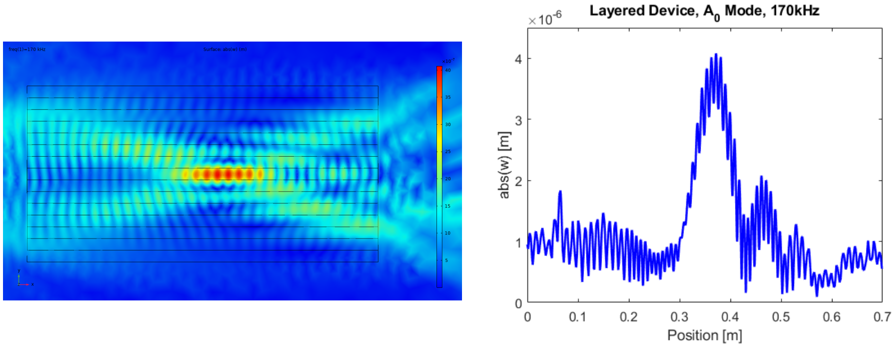

Figure 4.38: Plots of the absolute value of displacement, along the z direction, for the Si+Pb layered device testing the A_0 mode at f=170kHz.

behaviour. The higher limit, on the other hand, predicts peaks not in the correct position, and are not attributable to the lens' effect. Having described the real device, the last step is to comment the layered one. Like it has been found for the S_0 wave propagation analysis even here, for A_0 waves, the layered device behaves better. However, differences between the two tested devices are much less pronounced for the A_0 mode. Starting from the low limit of the layered device for the A_0 mode, it is found to be 20kHz. Results of the simulation at that frequency are reported in figure 4.37. This time what strikes is that the analysis is practically the same performed with the real geometry, as the same strong points and limitations are found. In particular, at this frequency the device works, has a focusing spot placed at x=36cm but, as underlined before, the increment between the displacement at the lens' edge and the one at the centre is very shallow, underlining that the device brings a very small amplification. In fact, the overall magnification effect at the peak is registered as 2.5x. Figure 4.38 reports results for the upper frequency limit of this last configuration tested. This time, the upper frequency limit is perfectly matched, with the

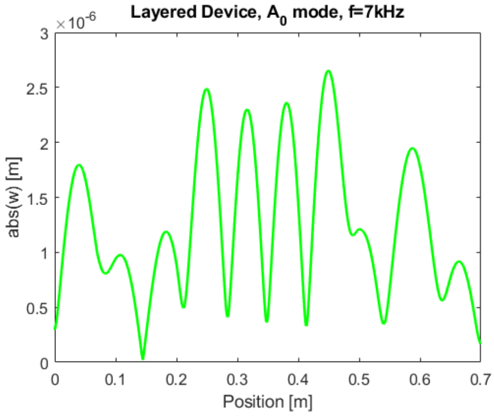

Figure 4.39: Line plot of absolute value of displacement, along the z direction and taken at y=0, for the Si+Pb layered device testing A_0 waves at the theoretical low frequency limit.

Table 4.8: Comparison between theoretical ranges and discovered ones, for the A_0 mode, on the Silicon and Lead device focusing waves at the centre.

Theoretical Range	**Real Geometry**	**Layered Geometry**
7kHz<f<170kHz	20kHz<f<90kHz	20kHz<f<170kHz

analysis at $f = 170kHz$ showing a correct behaviour. In fact, in this case it can be noticed that the peak is strongly localised at the centre of the lens, with an absolute maximum reached at x=36cm. The overall trend of the analysis across the device is also great, with a sharp amplification predicted only at the focusing point, as it should be. Figure 4.39 reports the line plot of absolute value of displacement for the case belonging to the theoretical frequency limits. This time, the only non matched limit was the lower one, reported in the green graph. The device shows a flat behaviour, with no focusing detected. Finally, table 4.8 recaps the discovered ranges for the A_0 device and puts them in comparison with the theoretical ones. Once again, the real device shows a lower range reproducibility than the layered one. In particular, the layered geometry is able to almost correctly grasp the whole behaviour, missing only some low frequencies. The low frequency limit is the same for both geometries, placed at f=20kHz, which corresponds to $\lambda = 8.7a$. Even this time the maximum working wavelength is around half the ideal limit. As it has been underlined before with the analysis of the devices at $ka = 1$, generally speaking A_0 mode simulations results between the two different geometries show a better degree of convergence that the correspondent S_0 mode results. Having tested the focusing properties and the accuracy of this lens, the next step will be dedicated to testing this configuration with different pairs of materials. In particular, up to this point the pair of materials silicon + lead has been tested. However, if this design is supposed to be built and not only theorized, a practical realization of a prototype with such different material will be particularly challenging and, if it is even possible, most probably it will not be cost efficient. This premise poses ground for testing the usage of different pairs of materials, to find one that will be more suitable for a prototype realization. The most obvious choice, even thinking at a possible application in MEMS and micro-devices world is using silicon coupled with hollow inclusions, as existing manufacturing processes for MEMS already allow to build such structures. The next part is dedicated to the analysis of the device built with this pair of materials. For reference, results will be compared with the previous case with central focusing, which showed to be the most consistent and precise overall. For this exact reason and to make the comparison as fair as possible, even the new device is set to focus waves at its centre. The setting of the analysis has not changed by any means: the same absorbing boundary conditions are applied, to eliminate the interference of reflected waves inside the domain. Even the prescribed displacement is set in the same manner. For what concerns the mesh used, the same discussion made above for the silicon and lead device apply. In particular, both devices have been tested by using a free tetrahedral mesh. However, the layered one was built using an "extra fine" element size, while the real geometry allowed only for the use of "finer" element size. Remembering that the frequency at which the analysis is lead depends on the plate velocity of the external homogeneous layer, even this parameter doesn't change, as the bulk material is still silicon.

As a reminder, the frequencies are

$$f_{A0} = \frac{\omega}{2\pi} = \frac{v_p h_b}{2\pi\sqrt{12}} k_A^2 = 38399Hz \tag{4.39}$$

$$f_{S0} = \frac{\omega}{2\pi} = \frac{v_p k_S}{2\pi} = 133019Hz \tag{4.40}$$

As usual, we start this comparison from the analysis of the S_0 mode. The simulation at the given frequency is shown in figure 4.40 for both the real device, shown on the left, and the layered device, shown on the right. As the two images clearly show, the device works correctly even in this case with different materials. The focusing point is correctly predicted in both analysis and visible in both images. To make more precise assessments, a comment on the line plots which represent the absolute value of the amplitude of displacement, reported in figure 4.41, is brought up. Of course, being the inclusions empty in this case, the line plot is not made at y=0, because the plot will be constantly interrupted by the hole's presence, but is made at a slightly lower coordinate, at y=-0.5a=-5mm. There it can be noticed that the two trends are not identical but share

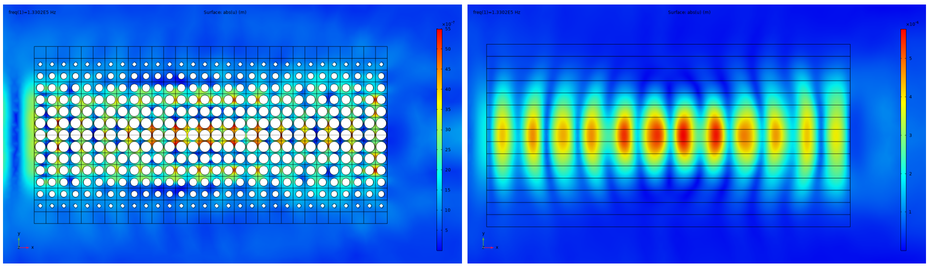

Figure 4.40: Surface plots showing the absolute value of displacement, along the x direction, for a Si+Holes GRIN lens with central focusing when testing the S_0 mode. Left: real device. Right: layered device.

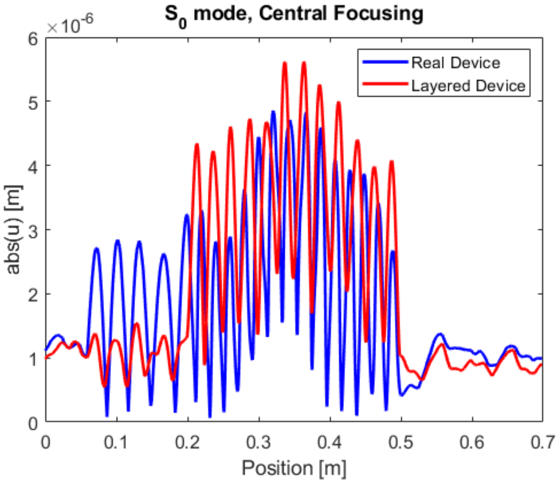

Figure 4.41: Comparison of line plots of absolute value of displacement, computed at y=0, for the Si+holes device testing the S_0 mode.

similar traits. In particular, the focusing point is predicted, in both geometries, at the coordinate x=36cm, so near its theoretical position at x=35cm. The maximum amplification is different in the two cases, being 5.5x in the layered geometry and 4.75x in the real case. Overall, the analysis shows a good trend, and the phenomena is correctly reproduced. After this promising premise, the next step is to evaluate the performances of the A_0 mode. In figure 4.42 are reported the surface graphs where the absolute value of displacement, along the z direction, can be seen at comparison for both geometries. Even in this case, the behaviour of the device is correctly reproduced by both geometries. The focusing point is clearly visible in red and the effect of deviation and focusing is correctly reproduced by both geometries. As usual, to make more precise comparisons we look at the line plot of the absolute value of displacement, taken at the y=-5mm line, reported here in figure 4.43. As it was noted for the previous devices, even here for the device with holes the A_0 mode comparison shows an overall better agreement between the test fo different geometries. In

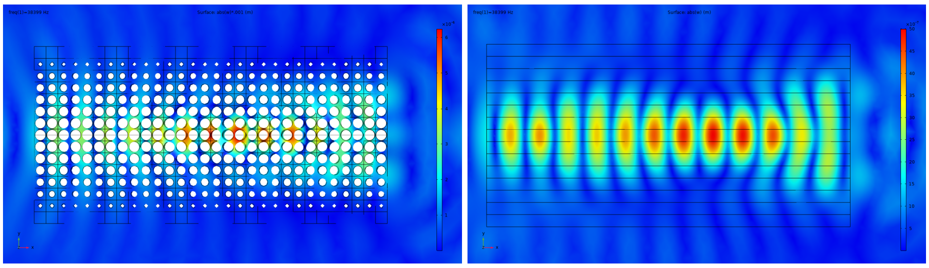

Figure 4.42: Surface plots showing the absolute value of displacement, along the z direction, for a Si+Holes GRIN plate with central focusing when testing the A_0 mode. Left: real device. Right: layered device.

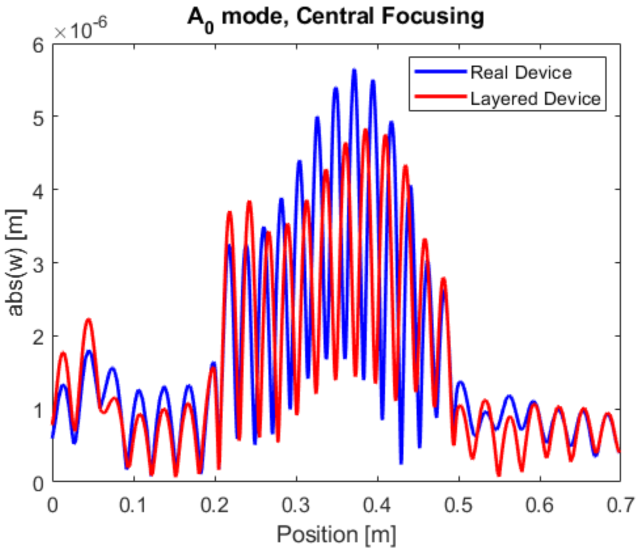

Figure 4.43: Comparison of line plots of absolute value of displacement, computed at y=0, for the Si+holes device testing the A_0 mode.

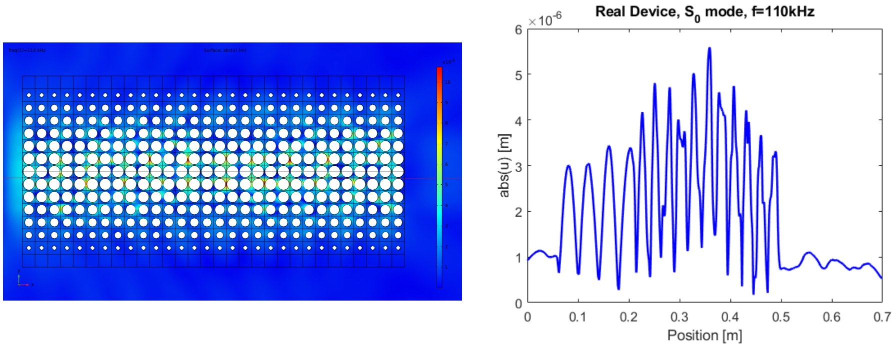

Figure 4.44: Plots of the absolute value of displacement, along the x direction, for the Si+Holes real device testing the S_0 mode at f=110kHz.

particular, the trend reproduced is the correct one for both, as the focusing point is present and visible, though a little bit shifted from the theoretical position. In the real device the focusing point is at x=37cm, while on the layered device is at x=37.5cm. The amplification effect is visible and the device behaves as supposed. Even here there is a small difference for what concerns the amplitude of displacement prediction, here higher on the real device, which predicts a 5.5x with respect to the layered one, which predicts a 5x magnification effect. So, for what concerns analysis at the wavenumber $ka = 1$, results are good. To further test even this design, the frequency range behaviour is tested next. Again, since the bulk material is the same in both devices, the theoretical ranges calculated before do not change. As done previously, the first tests report the range simulated by the real device with the S_0 mode. Similarly to what has been found for the device with lead inclusions, the range of the real device with the S_0 mode is particularly shallow. Figure 4.44 reports the lower limit in frequency found by numerical simulations, which is 110kHz, far from the theoretical one. Looking at both plots reported, it can be deduced that the focusing point is present at a reasonable coordinate, being placed at x=36cm. The magnification effect on the displacement amplitude, given by the lens, is great, with a predicted 5.5x amplification. There only strange element is a zone

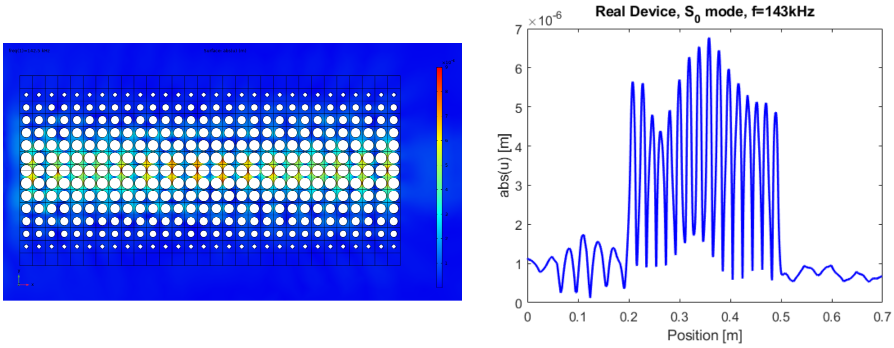

Figure 4.45: Plots of the absolute value of displacement, along the x direction, for the Si+Holes real device testing the S_0 mode at f=143kHz.

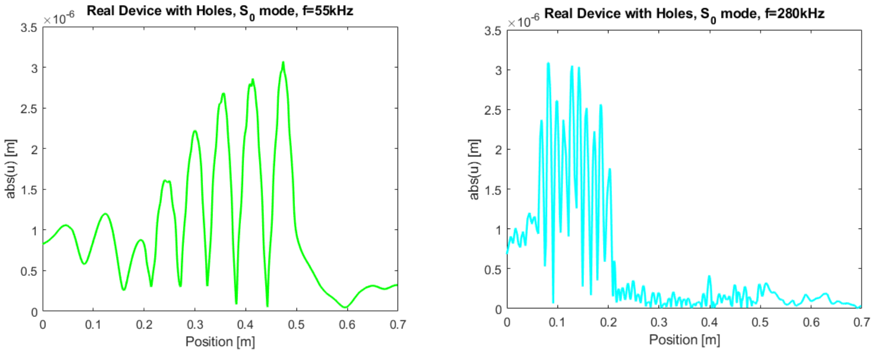

Figure 4.46: Line plots of absolute value of displacement, along the x direction and taken at y=0, for the Si+Holes real device testing S_0 waves at frequencies correspondent to theoretical frequency limits. Left: 55kHz. Right: 280kHz.

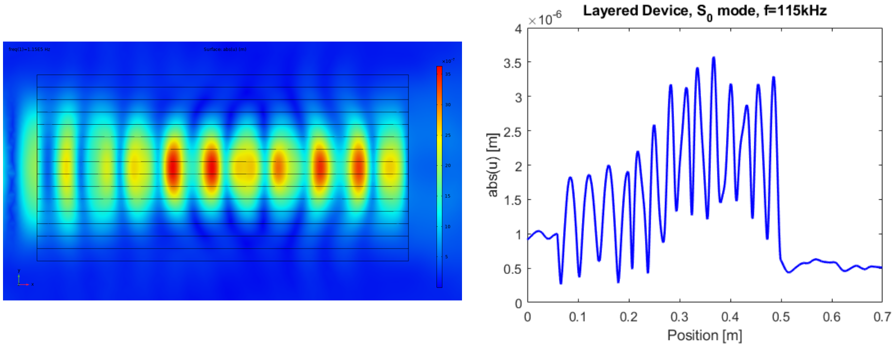

Figure 4.47: Plots of the absolute value of displacement, along the x direction, for the Si+Holes layered device testing the S_0 mode at f=115kHz.

outside the device which behaves abnormally, as a pretty high displacement is registered even before the lens is encountered, which should not be present in the final analysis. However, after the lens is encountered, the magnification effect is triggered as it should be. Figure 4.45 reports the plots of the absolute value of displacement for the upper limit in frequency found by numerical simulations, which is 143kHz. Here it can be noticed that the simulation is starting to show some problems. The focusing point is present, even at a great coordinate, being placed at x=35.5cm. The effect of the device is clear and visible, but some peaks at the device are starting to be predominant. To demonstrate that the device doesn't work outside this shallow frequency limit, simulations at frequencies equal to the theoretical limit are reported in figure 4.46. The theoretical low limit in frequency, represented by the green line plot, focuses waves at the wrong point, placing it at the lens' end rather than in the middle. The upper limit, on the other hand, behaves even worse, as an effect is registered before the lens, where no phenomena should be present, while inside the lens the behaviour is completely flat. Passing on to the review of the S_0 mode propagation on the layered device, the following is found. The range predicted by simulations is closer to the ideal one, but still not completely matched. Figure 4.47 reports the

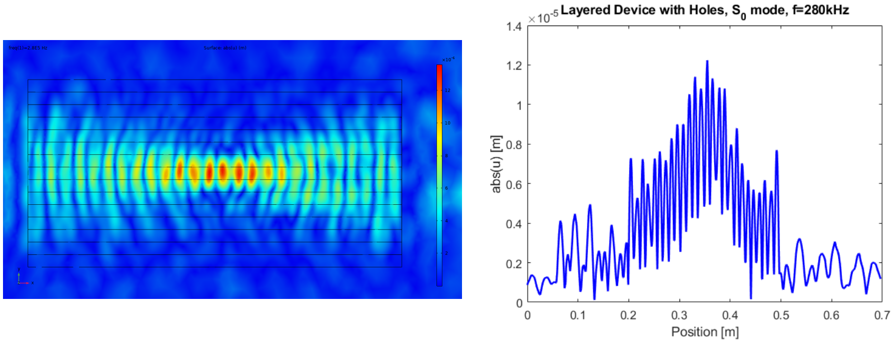

Figure 4.48: Plots of the absolute value of displacement, along the x direction, for the Si+Holes layered device testing the S_0 mode at f=280kHz.

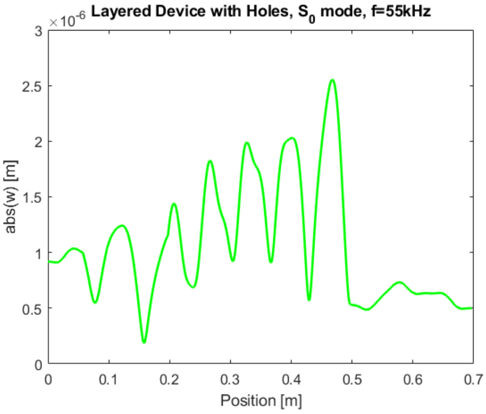

Figure 4.49: Line plot of absolute value of displacement, along the x direction and taken at y=0, for the Si+Holes layered device testing S_0 waves at the frequency correspondent to the theoretical low frequency limit of 55kHz.

absolute value of displacement for the lower frequency limit, found to be 115kHz.

In particular, it can be noticed that, at this frequency, the focusing point is present and at a coordinate x=36.5cm, not so distant from the theoretical point. The problem is, again, that the displacement peak at the middle is less localized, with the surrounding areas presenting a similar value of displacement. The upper frequency limit, on the other hand, is matched at 280kHz. Looking at the results for this analysis, reported in figure 4.48, what strikes the most is the expected magnification effect, set to be 12x, a very promising result indeed not matched by any simulation made here. There overall trend is also very good. Is worth to mention, though, that for some frequencies around this limit

Table 4.9: Comparison between theoretical ranges and discovered ones, for the S_0 mode, on the Silicon and holes device.

Theoretical Range	**Real Geometry**	**Layered Geometry**
55kHz<f<280kHz	110kHz<f<143kHz	115kHz<f<280kHz

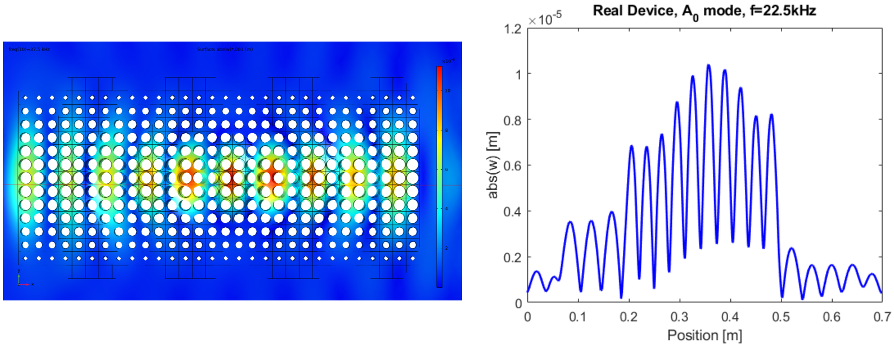

Figure 4.50: Plots of the absolute value of displacement, along the z direction, for the Si+Holes real device testing the A_0 mode at f=22.5kHz.

the behaviour at the lens' edge starts to become anomalous since peaks start to arise even there. To demonstrate that the low frequency limit is not matched, results of simulation at that frequency is reported in figure 4.49, where is clear that the device does not focus waves on the correct position. Concluding the discussion for S_0 waves, table 4.9 reports a comparison between the theoretical ranges and the ones found by numerical simulation software. Similar conclusions to the ones already reported for the silicon and lead device can be made. In particular, the real device shows a shallower range than the layered device, probably due to the coarser mesh. The lower frequency limit is similar for both devices, corresponding to a wavelength $\lambda = 7.5a$. The main difference lies in the upper frequency limit. While the layered device matches the upper limit, so still around the theoretical limit, the real device places such limit at a much larger wavelength, precisely $\lambda = 5.84a$. Having discussed the range for the S_0 waves, the final discussion is dedicated to the comparison of ranges for the A_0 waves. Starting the overview with the real geometry, the lower frequency limit is not matched, as the minimum working frequency is found to be 22.5kHz. Figure 4.50 reports the surface plot of the absolute value of displacement for the analysis at that precise frequency value. There it can be noticed that the maximum amplification value is reached at the centre of the device, precisely

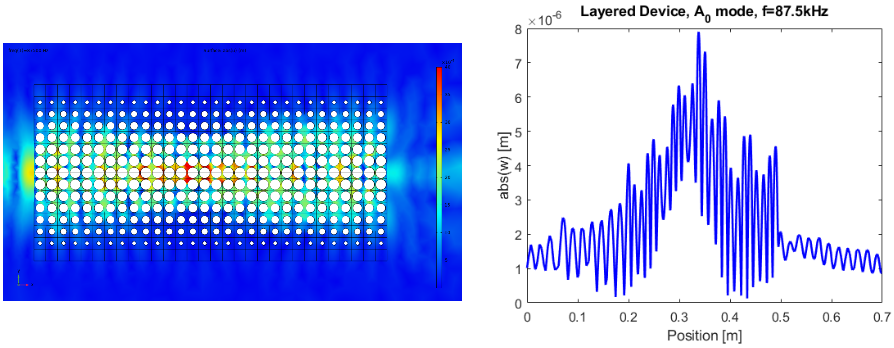

Figure 4.51: Plots of the absolute value of displacement, along the z direction, for the Si+Holes real device testing the A_0 mode at f=87.5kHz.

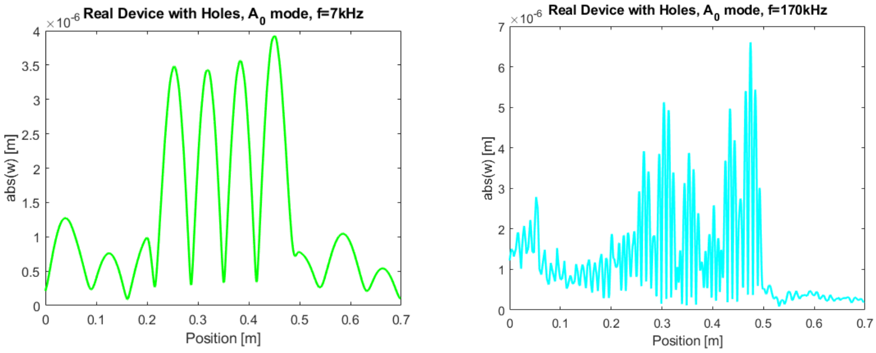

Figure 4.52: Line plots of absolute value of displacement, along the z direction and taken at y=0, for the Si+Holes real device testing A_0 waves at frequencies correspondent to theoretical frequency limits. Left: 7kHz. Right: 170kHz.

at x=36cm. Even here the amplification effect predicted by the device is much more promising, arriving at a 10x with respect to the maximum amplitude of displacement given by the input. Again, the only problem encountered here is that the device shows a bit of amplification even before the lens is met. However, inside the device, the behaviour is the expected one. Even the upper frequency limit is not matched, particularly analysis work until the frequency 87.5kHz is reached. The response of the device at that frequency is reported in figure 4.51. In particular, the focusing point is still clearly visible, and the central peak is very sharp and localised, being placed at x=34cm. Even the general trend is very great this time, as the displacement amplification effect is reached gradually along the lens. Even here, to further demonstrate that theoretical limits are not matched, figure 4.52 reports results for simulations at the theoretical frequency range. The low theoretical limit, represented in green in the image, shows an almost flat behaviour, as if no lens was present. The upper theoretical frequency limit, represented in the light blue graph, does not show focusing, as the trend of displacements inside the device do not follow the correct trend. Before making final considerations, the performances of the layered device are commented. The layered device, as always, is able to grasp

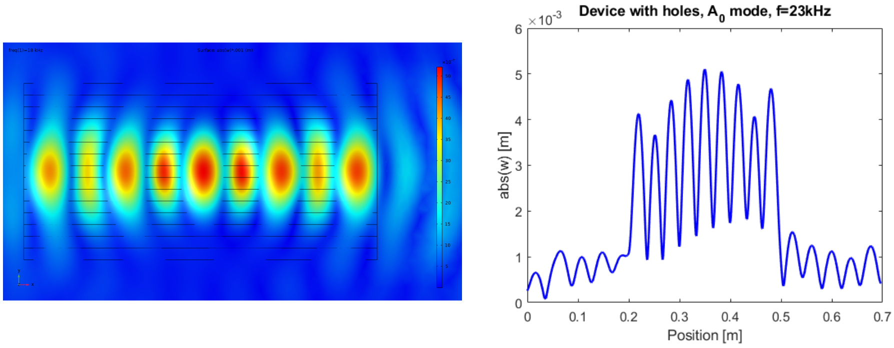

Figure 4.53: Plots of the absolute value of displacement, along the z direction, for the Si+Holes layered device testing the A_0 mode at f=23kHz.

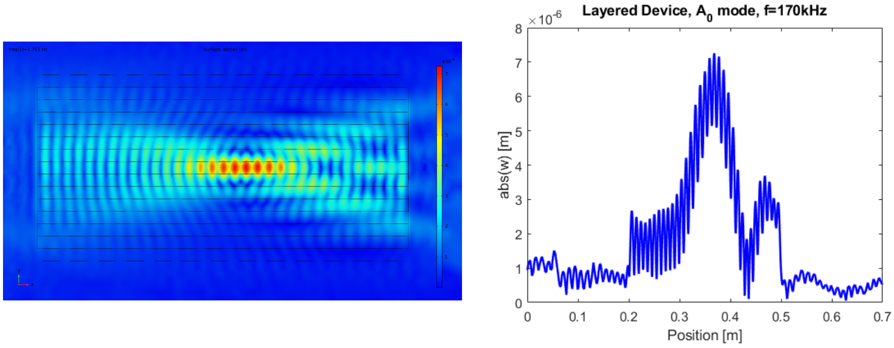

Figure 4.54: Plots of the absolute value of displacement, along the z direction, for the Si+Holes layered device testing the A_0 mode at f=170kHz.

the functioning of the device more correctly. In particular, the lower limit in frequency is still missed, as the analysis places it at 23kHz. Its results are reported in figure 4.53. There, it can be noticed that a focusing effect on the centre is present. However, the difference in displacement between the edges of the device and the centre is much less pronounced. This analysis is very similar to the correspondent one for the real device, underlining once again that A_0 waves simulations tend to converge better between different geometries. Even here, for the layered geometry, the upper frequency limit is completely matched, being placed at 170kHz, and its results are reported in figure 4.54. The result for the high frequency limit is particularly promising. In fact, the focusing point is very localized, and the displacement amplification is reached gradually, as it should be. The displacement amplification value is even great, reaching a 7x value. Figure 4.55 reports results for the analysis at the theoretical frequency limit, to further confirm the conclusions reported here. As the upper frequency

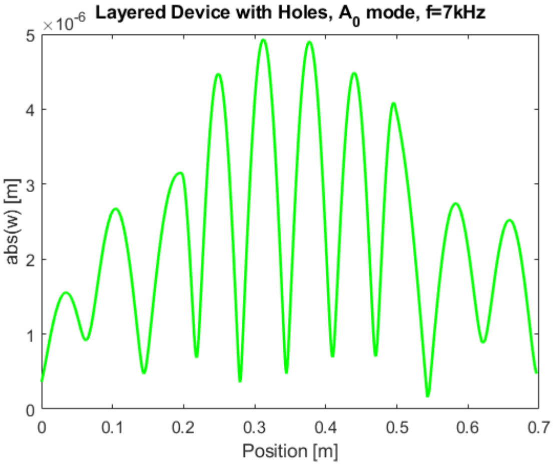

Figure 4.55: Line plot of absolute value of displacement, along the z direction and taken at y=0, for the Si+Holes layered device testing A_0 waves at the frequency correspondent to the theoretical low frequency limit of 7kHz.

Table 4.10: Comparison between theoretical ranges and discovered ones, for the A_0 mode, of the Silicon and holes device.

Theoretical Range	**Real Geometry**	**Layered Geometry**
7kHz<f<170kHz	22.5kHz<f<87.5kHz	23kHz<f<170kHz

limit is matched, only the lower limit analysis will be reported here. As it is clearly visible from the image, also this time the behaviour is not bad, but it has been removed from the range since, even here, frequencies between 7 and 23kHz fail to show the correct behaviour. Table 4.10 reports a comparison between the theoretical limits and the ones found by numerical simulation software. One again, the layered device performs better due to its more refined mesh. As it was discovered for the device with lead, the A_0 mode is overall better represented even in the real device, where it is able to show a broader frequency limit than it predicts for the S_0 waves. The low frequency limit of 23kHz corresponds to a wavelength of $\lambda = 8.1a$, a bit more than half the theoretical limit. The upper frequency limit, for the real device, is set at f=87.5kHz, which corresponds to $\lambda = 4.1a$, which is not that bad if we recall that the authors of the theory predicted a minimum working wavelength of 3 or 4 unit cells. Still, the behaviour does not match the one of the layered geometry, which is able to match the limit completely. Having concluded even the comparison for the Si+Holes device, some conclusions can be made. The two devices share many treats, for example both have some frequency range reproducibility issues, especially on the real device. In terms of working capabilities, both are very good. The only consistent difference between the two is that the device with holes predicts, on average, much greater displacement amplifications, which is a very appreciated feature, considering that, if one has to think of building a prototype, making it with through holes and silicon would be much easier than doing it with lead. The only remark made here is that the central holes of the Si+holes device reach a filling fraction of f=0.6, which is a mid to high filling fraction. Remembering that the device does not work for high filling fraction, the only potential problems were related to working capabilities issues but, since simulations showed a good behaviour, this concerns should not be problem at all.

4.3 Time Domain Analysis

Having concluded the part dedicated to the overview of each GRIN device capabilities, in the next pages the attention will be put on time domain analysis. In this case, simulations aim at reproducing the behaviour of the device giving, as an output, the focusing of the GRIN lens as it evolves in time. This types of analysis are closer to what happens in real life, so they usually allow to visualize better the phenomena. This time, two analysis will be conducted in the time domain. The first simulation is dedicated, again, to the correct visualization of the focusing point, to check if informations found before are in agreement with what will be found in time domain analysis. The second test, on the other hand, aims at testing the wide frequency range functioning of the device more thoroughly. In fact, it has been demonstrated that the device works in a frequency range wide enough. The next step is to check if it is able to correctly recognise and focus a non monochromatic input, so a multi-frequency wave inside the working range of the device. For what concerns the setting of the analysis, it has not changed: the same boundary conditions apply. This means that absorbing boundary conditions are implemented alongside the external thickness of the cylinder to avoid that waves, on this boundary, can reflect and interfere with the phenomena. What will change in both tests, with respect to frequency analyses, is the application of the given input. In fact, for the focusing test, a sine burst input will be given, composed of 4 cycles of sinusoidal displacement centred at a precise frequency. For the second test, a sinusoidal displacement which changes frequency in time is given. Figure 4.56 reports the graphical representation of both inputs. Both test will be carried only on the silicon and lead device, focusing waves on the centre, and on the layered geometry, to further test the potential of the design presented by the authors of the "effective medium theory". Having described the setting of the analysis, results are reported. Starting with the focusing point test, the performances of the S_0 mode are reviewed first. For this test, remembering the conclusions that were made on the mentioned device, a sine burst centred at f=133kHz is tested. Figure 4.57 shows the instant at which the sine burst input is focused in this configuration. It can be noticed that the behaviour is the one expected: in

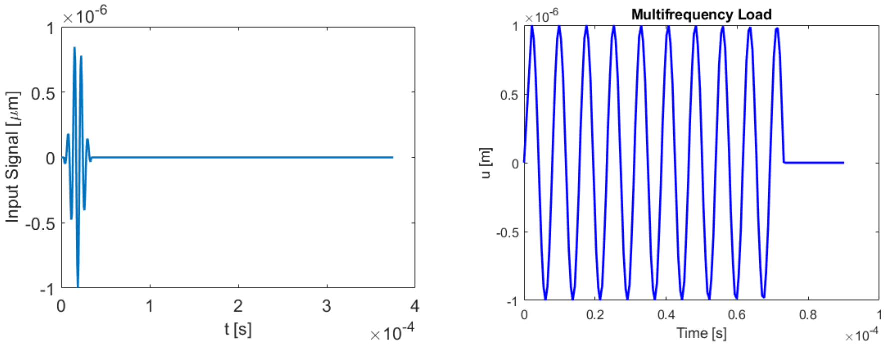

Figure 4.56: Graphical representation of the different inputs used for time domain analysis. Left: sine burst input used for the focusing test. Right: multi-frequency input used for the second test.

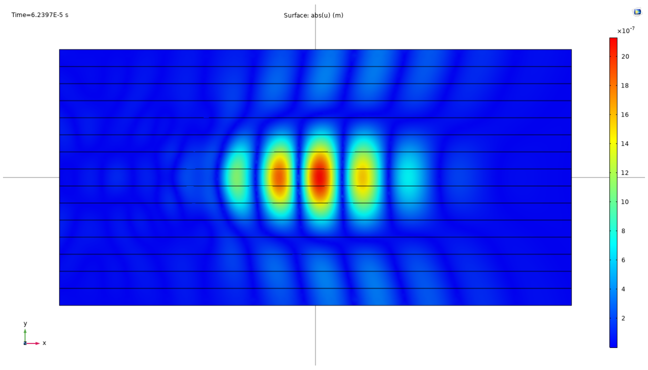

Figure 4.57: Surface plot showing the absolute value of displacement, along the x direction, registered in the S_0 mode analysis at time $t = 6.23 \times 10^{-5}$

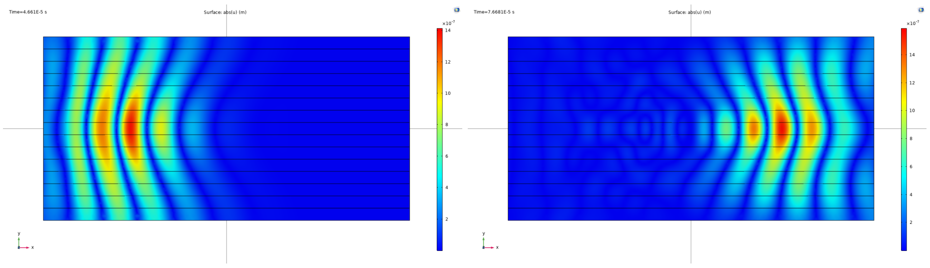

Figure 4.58: Surface plot showing the absolute value of displacement, along the x direction, registered in the S_0 mode analysis at two different time frames. Left:$t = 4.661 \times 10^{-5}$. Right: $t = 7.668 \times 10^{-5}$

plane S_0 waves are focused at the correct spot. The amplification effect, which had an amplitude of displacement of $1\mu m$ maximum, is roughly 2.2x, matching what has been found in frequency analysis. Even the overall trend is correctly reproduced, as the maximum displacement value at the centre of the device is reached by gradual amplification. Figure 4.58 helps visualise the phenomena in a better way: waves enter the GRIN lens from the left. There, thanks to the different effective properties of each layer, the wave is bent as a consequence of the refractive index tuning and is focused on the central spot. After that, waves exit from the device almost as collimated as they were at the entrance. Overall, the agreement between this simulation and the correspondent one in frequency domain is great. Going on with th analysis, the A_0 wave propagation behaviour is tested next. In particular, this time the sine burst was centred at frequency 170kHz, as it proved to be the most promising from the analysis of ranges. Figure 4.59 reports the instant at which focusing is achieved Even in this case, the behaviour reproduced is exactly the expected one and converges to the informations found in the frequency analysis. The focusing point is sharp and localised, and predicts an amplification effect of 3.5x, reached gradually. This time the predicted amplitude of displacement is a bit lower than the theoretical maximum in the frequency analysis, which placed the amplification at 4x. However, keeping in mind that the input between the two simulations is different, the result found is not bad at all. Looking at figure 4.60, even here

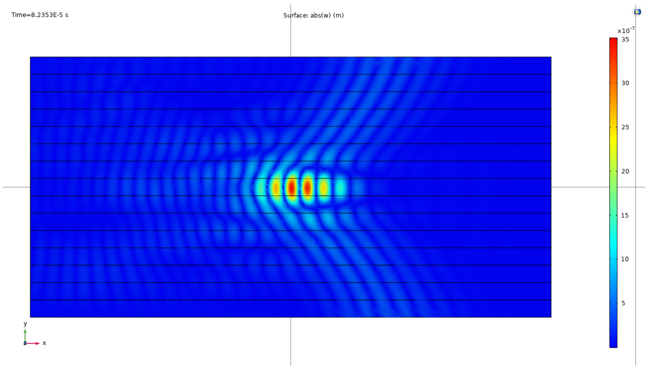

Figure 4.59: Surface plot showing the absolute value of displacement, along the z direction, registered in the A_0 mode analysis at time $t = 8.23 \times 10^{-5}$.

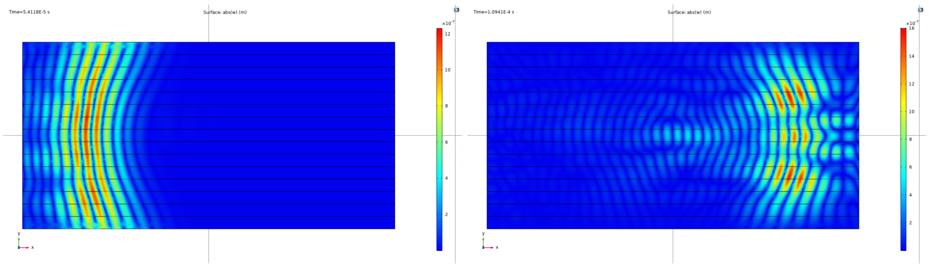

Figure 4.60: Surface plot showing the absolute value of displacement, along the z direction, registered in the A_0 mode analysis at two different time frames. Left: $t = 5.43 \times 10^{-5}$. Right: $t = 1.04 \times 10^{-4}$

it can be seen that the device is working correctly: waves enter on the left, are bent thanks to the refractive index profile, and exit from the device collimated, as the two pictures at different time frames show. Having confirmed that informations between time and frequency domains converge, the next step will be dedicated to the use of a multi-frequency load, like the one depicted in figure 4.56. These loads have been obtained in MATLAB using the chirp function. Essentially, the load starts, at time $t_0 = 0$, at a precise value of frequency, which is increased linearly up to a second time frame value t_1. For both the test of the S_0 and the A_0 mode, a multi-frequency load which varies in time of 10kHz will be tested. Of course, being the frequency ranges of the two modes different, the tested frequency window and the t_1 value will be different. In particular, for the S_0 mode, a load which varies between 130kHz and 140kHz will be used, with $t_1 = 7.31 \times 10^{-5}$. For the A_0 mode, on the other hand, a load which ranges from 40kHz to 50kHz will be applied, with $t_1 = 2.56 \times 10^{-4}$. Starting the review of results with a comment on the S_0 mode, figure 4.61 reports surface plots of the absolute value of displacement, along the x direction, taken at two different time frames. In particular, the time frame on the left represents the moment at which waves start crossing the centre of the device, while the time frame on the right represents the last time frame at which waves cross the centre. It is clearly visible that focusing in evident in both images, and this means that the feature of the lens, so focusing properties, are maintained throughout the

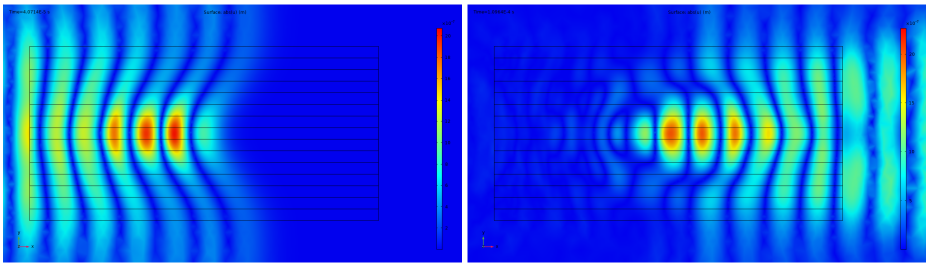

Figure 4.61: Surface plot showing the absolute value of displacement, along the x direction, registered in the S_0 multi-frequency analysis at two different time frames. Left: $t = 4.07 \times 10^{-5}$. Right: $t = 1.09 \times 10^{-4}$.

whole analysis, which was exactly the aim of this test. Having confirmed the behaviour for the S_0 mode, the last step will be dedicated to testing the A_0 mode. Results for the A_0 mode are reported in figure 4.62. Here, it can be appreciated that the same considerations made on the S_0 mode still apply: the focusing behaviour is present and clearly visible in both images. This means that focusing is maintained throughout the whole analysis, from the first time step at which waves cross the centre of the device, to the last one. This last analysis demonstrated that even a non monochromatic input can be correctly recognised by the device and focused, which is a great feature, given that not always monochromatic inputs are available in the environment to be exploited.

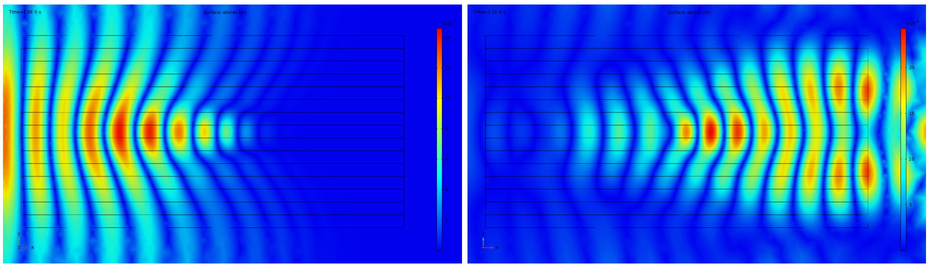

Figure 4.62: Surface plot showing the absolute value of displacement, along the z direction, registered in the A_0 multi-frequency analysis at two different time frames. Left: $t = 7.9 \times 10^{-5}$. Right: $t = 3.3 \times 10^{-4}$.

Chapter 5

Luneburg lens prototype 1

This chapter is dedicated to the analysis of the numerical simulation results for one of the two Luneburg lenses tested in this work. In particular, as it will be explained shortly, this lens has been built exploiting the same guidelines followed for the GRIN lens, so the same effective medium theory still applies. In particular, section 5.1 deals with an overview on the theoretical model used for this lens. Since it has already been explained in chapter 4, here only the major differences between the two devices, hence the refractive index profile, will be treated in more detail. Section 5.2 deals with the analysis and comment of the results for this device developed in the frequency domain, making comparisons between layered and real geometry, with the addition of some new tests performed here concerning the directionality of the input in an omnidirectional lens, like this one. Then, section 5.3 deals with time domain simulations, aimed at the verification of convergence between what has been discovered before in frequency. A part of the discussion will be reserved to the test of a beam for wave energy localization and, possibly, energy harvesting.

5.1 Construction of the Lens

The aim of this section is to explain all the theoretical passages which allow to build the final design for the first prototype of Luneburg lens. Such lens has been built following the same effective medium theory proposed by Pennec et al. in 2007[26, 27] and already explained in the previous chapter for the construction of GRIN lenses. As such, since the derivation has already been reported there, here the focus will be particularly put on all the differences that arise between this design and the previous one. A first change manifests in the definition of the unit cell, which now is a rhombus and can be observed in figure 5.1. This was done to respect the particular symmetry of this lens. Luneburg lenses, as it has been cleared in Chapter 2, are omnidirectional devices, which means that their working principle is maintained notwithstanding the direction from which the input arrives. This feature descends form their radial symmetry, hence the need for a change of definition in the unit cell, as the construction of the device becomes easier with this type of symmetry. Since the geometry of the unit cell has been changed, now the filling fraction definition changes

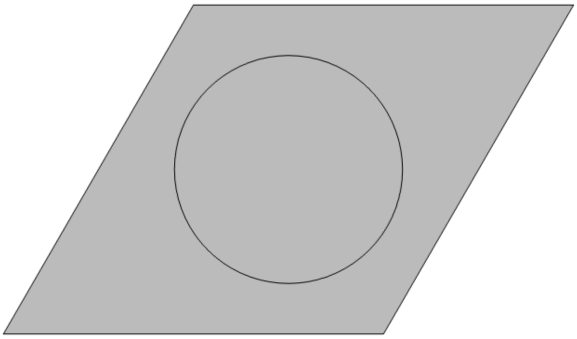

Figure 5.1: CAD representation of the unit cell employed in this chapter for the construction of a Luneburg lens.

accordingly, becoming

$$F = \frac{2\pi(d/2)^2}{\sqrt{3}a^2} \tag{5.1}$$

where a is the lattice constant and d is the diameter of the inclusion added in the unit cell. Having cleared this point, the goal now is to create the device by matching the refractive index profile generated by the change in the inclusion's diameter to a theoretical one coming from an ideal profile. As it has been explained before, the refractive index of a Luneburg lens that focuses planar

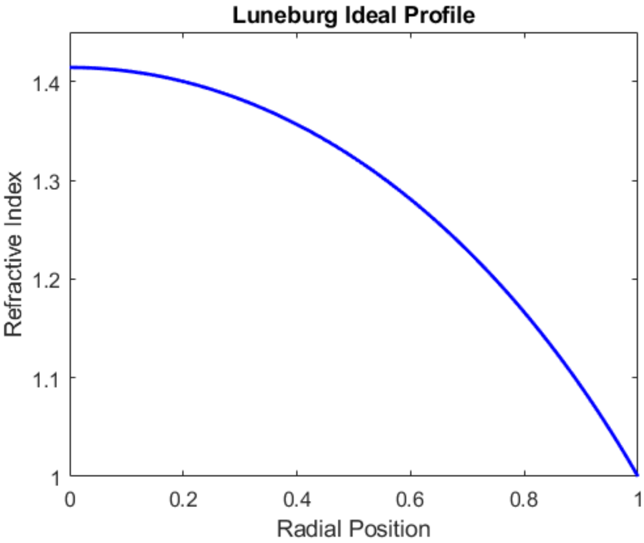

Figure 5.2: Graphical representation of the ideal profile of a Luneburg lens versus the radial position inside the lens.

wavefronts on the opposing point with respect to the entrance one is

$$n(r) = \sqrt{2 - \left(\frac{r}{R}\right)^2} \tag{5.2}$$

where r is the radial position of the unit cell inside the lens and R the lens' radius. A graphical representation of this profile versus the radial position inside the lens is proposed in figure 5.2. Having defined the theoretical profile, the following step is to define the refractive index inside the lens to tailor it accordingly. One of the advantages of this effective medium theory lies in the ability to tune independently the refractive index for two separate Lamb wave modes: the S_0 mode and the A_0 mode. If our final device has to focus both types of waves on the same spot, as it was done for the GRIN plate, the two refractive indexes have to be matched across the whole device. Being the dispersion relation of the two waves different, their index definition will change accordingly: in particular we have that

$$n_{S_0} = \frac{v_{pb}}{v_p(r)} \tag{5.3}$$

$$n^2_{A_0} = \frac{v_{pb}}{v_p(r)} \frac{h_b}{h(r)} \tag{5.4}$$

where v_p is the plate velocity term, which depends on the plate's rigidity and its density, h is the plate's thickness and the subscript b denotes material properties of the background material. To be able to set both refractive indexes to the same value, the S_0 mode's index is regulated first. So we search, at a given position, for the plate velocity's value which is able to grant that index tuning. Once it has been identified, the last step is to tune the A_0 mode's refractive index by changing the thickness of the plate locally, as now the plate velocity is a given

Table 5.1: Material Properties values for Silicon, Lead and Aluminium.

MATERIAL	**E [GPa]**	ν	$\rho[Kg/m^3]$
Si	150	0.28	2330
Pb	16	0.44	11340
Al	70	0.35	2710

Table 5.2: Data for the Silicon and Lead Luneburg device

y[m]	**n(y)**	$v_p[m/s]$	**f**	**R[mm]**	**h[mm]**	**E [GPa]**	ν	$\rho[Kg/m^3]$
0	1.4142	5909.92	0.149	2.178	7.071	118.26	0.229	3672.49
a	1.4107	5924.75	0.148	2.170	7.089	118.45	0.230	3663.48
2a	1.4	5969.92	0.144	2.141	7.143	119.20	0.231	3627.44
3a	1.3820	6047.55	0.138	2.096	7.236	120.34	0.233	3573.38
4a	1.3565	6161.52	0.129	2.026	7.372	122.06	0.236	3492.29
5a	1.3229	6317.97	0.117	1.930	7.559	124.41	0.239	3384.17
6a	1.2806	6526.41	0.102	1.802	7.809	127.40	0.244	3249.02
7a	1.2288	6801.55	0.083	1.625	8.138	131.30	0.250	3077.83
8a	1.1662	7166.83	0.061	1.388	8.575	136.09	0.258	2875.11
9a	1.0909	7661.66	0.033	1.025	9.170	142.22	0.268	2627.33
10a	1	8357.89	0	0	10	150	0.28	2330

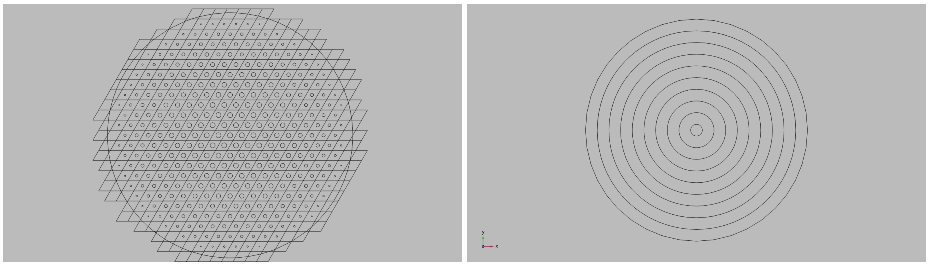

Figure 5.3: CAD drawings of the two different geometries of the Luneburg lens. Left: real device. Right: layered device.

term already calculated. Having done that, the value of every variable that is needed to define our effective material can be obtained, since the needed filling fraction at a given point is known, so simulations can be started. Following what has been done by the authors, the studied device was created with a unit cell made of silicon with lead inclusions. Their material properties are reported in table 5.1, while the derived effective medium properties are reported in table 5.2. The idea, at this point, was to try and build a different lens based on a more convenient pair of materials, like it has been done for the GRIN plate. The obvious choice, even here, was to try the same base material, so silicon, with hollow inclusions. There was, however, a problem. Supposing that the filling fraction can range from 0 to 1, the effective plate velocity term for silicon and hollow inclusion, normalized with respect to the background value, ranges from 1 to 0.72. Since this precise refractive index profile requires a maximum index of 1.414, we have that $v_p(y)/v_{Si} = 0.7$, which is unreachable and, so, this pair of material is not suitable for the construction of a Luneburg lens with this refractive index profile. The obvious subsequent thought was to change the bulk material, in order to try match the plate velocity value needed. A try has been done with aluminium and holes as inclusions. In this case, the plate velocity value is reached, but only for filling fractions far too high. Remembering that the effective medium theory holds for low to mid filling fractions, we expect such built device to not show focusing. Generally speaking, using hollow inclusions here is made very hard since the plate velocity, with respect to the use of a solid material, changes more subtly. The plate velocity is defined as

$$v_p^2 = \frac{\bar{D}}{\bar{\rho}} \frac{E_b}{\rho_b(1-\nu_b^2)} \tag{5.5}$$

where values with a bar are normalized with respect to their background value. If we want the velocity term to drop, D has to drop too but ρ has to increase. This is exactly why lead inclusions are so good in terms of design: increasing the filling fraction allows to have a decreasing rigidity and an increasing density. With holes, both background terms are set to zero, so the overall decrement in v_p value is more gradual. Having cleared that holes employment with this design is rather impossible, to be able to build a different design we have to switch back to the usage of two solid materials. The issue of this configuration, however, remains, as the combination of two solid materials is usually more difficult to realize, if one has to think of a possible prototype. For this reason, the trial of a different material combination has been eventually scrapped for this design.

Table 5.3: Data for Silicon and holes Luneburg device

y[m]	**n(y)**	$v_p[m/s]$	**f**	**R[mm]**	**h[mm]**	**E [GPa]**	ν	$\rho[Kg/m^3]$
0	1.4142	5909.92	N.A.	N.A.	7.071	N.A.	N.A.	N.A.
a	1.4107	5924.75	N.A.	N.A.	7.089	N.A.	N.A.	N.A.
2a	1.4	5969.92	N.A.	N.A.	7.143	N.A.	N.A.	N.A.
3a	1.3820	6047.55	N.A.	N.A.	7.236	N.A.	N.A.	N.A.
4a	1.3565	6161.52	0.913	5.017	7.372	7.10	-0.103	202.71
5a	1.3229	6317.97	0.799	4.693	7.559	17.21	-0.0731	468.33
6a	1.2806	6526.41	0.660	4.265	7.809	31.06	-0.033	792.20
7a	1.2288	6801.55	0.502	3.720	8.138	49.49	0.021	1160.34
8a	1.1662	7166.83	0.337	3.048	8.575	73.14	0.088	1544.79
9a	1.0909	7661.66	0.168	2.152	9.167	104.83	0.173	1938.56
10a	1	8357.89	0	0	10	150	0.28	2330

Table 5.4: Data for Aluminium and holes Luneburg device

y[m]	**n(y)**	$v_p[m/s]$	**f**	**R[mm]**	**h[mm]**	**E [GPa]**	ν	$\rho[Kg/m^3]$
0	1.4142	3836.42	0.958	5.138	7.071	1.49	-0.096	115.18
a	1.4107	3846.04	0.945	5.104	7.089	1.93	-0.093	149.05
2a	1.4	3875.37	0.906	4.998	7.143	3.36	-0.083	254.74
3a	1.3820	3925.76	0.850	4.841	7.236	5.49	-0.067	406.50
4a	1.3565	3999.74	0.767	4.598	7.372	8.86	-0.042	631.43
5a	1.3229	4101.30	0.662	4.272	7.559	13.54	-0.007	915.98
6a	1.2806	4236.61	0.550	3.894	7.809	19.18	0.035	1219.50
7a	1.2289	4415.22	0.418	3.395	8.138	26.97	0.092	1577.22
8a	1.1662	4652.34	0.280	2.778	8.575	37.05	0.161	1951.20
9a	1.0909	4973.56	0.140	1.965	9.167	50.53	0.246	2330.60
10a	1	5425.51	0	0	10	70	0.35	2710

Table 5.2 and 5.3 still report material properties' data for the two discarded devices with holes. Figure 5.3 shows the silicon and lead device built with two different strategies: as a layered device and in its real configuration.

5.2 Frequency Domain Analysis

Having described in detail the derivation which leads to the calculation of the correct refractive index profile to realize this lens, the next step will be the review of some results. Even here, results will be split into time and frequency domain analysis, starting with the description of the latter. As it has been declared before, these analysis mainly aim at correctly reproducing the behaviour of the lens, to see if the design works or if there are problems to work out. The representation of the whole domain tested is reported in figure 5.4, which is composed of an external cylinder of radius 35cm where, at the exact centre, the lens is placed. To correctly reproduce the behaviour of the lens, absorbing boundary conditions have been set along the external thickness of the cylinder, to ensure that waves hitting that boundary are not reflected back into the domain. Essentially, this measure is taken to avoid that wave reflections at boundary can interfere with the focusing phenomena. The input is given, as for the previous

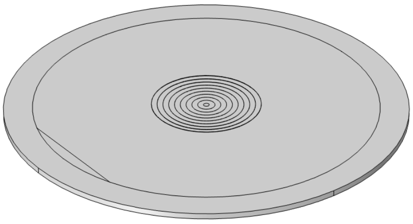

Figure 5.4: CAD drawing of the whole domain on which simulations have been performed.

analysis of the GRIN lens, as a prescribed displacement with a maximum amplitude of $1\mu m$ at a given frequency. To simulate planar wavefronts, an internal cylinder of radius 30cm was created and sectioned with a vertical plane placed at coordinate x=-28cm. If the test involves A_0 waves focusing, the displacement is given along the z direction while, if it involves S_0 waves, the displacement is set along the x direction. For more clarity, the line on which the displacement is set is highlighted in blue in figure 5.5. If the device works as intended, planar wavefronts are to be focused at point x=45cm. Following the guidelines given by the authors that presented and tested the effective medium theory[26], this device has been tested first at a frequency which corresponds to a wavenumber $ka = 1$, where a is the lattice constant, in this case set to $1cm$. Substituting this value inside the dispersion relation for S_0 waves, it is found that

$$f_{S_0} = \frac{\omega}{2\pi} = \frac{v_p k_S}{2\pi} = 133019Hz \tag{5.6}$$

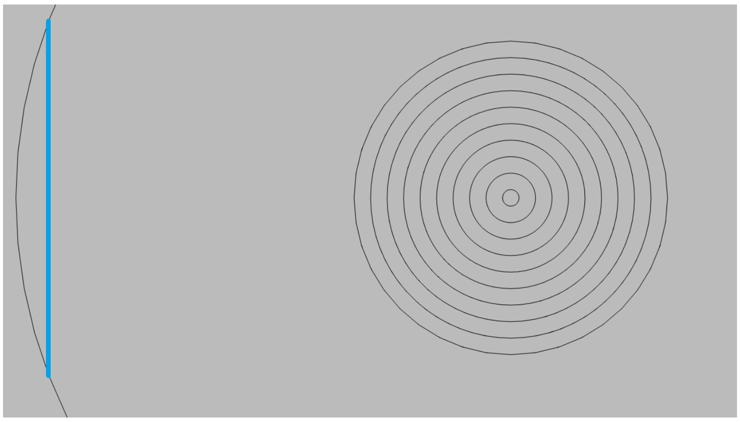

Figure 5.5: Representation of the zone where the load is applied to the structure.

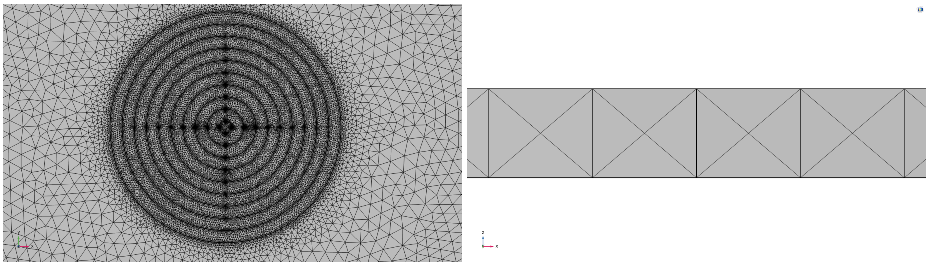

Figure 5.6: Graphical representation of the mesh used for the layered Luneburg device.

while, for the A_0 waves we have that

$$f_{A_0} = \frac{\omega}{2\pi} = \frac{v_p h_b}{2\pi\sqrt{12}} k_A^2 = 38399Hz \tag{5.7}$$

Before the comment of results is brought up, the meshes used for those simulations are presented. The mesh used for the layered device is reported in figure 5.6. This mesh has been built by using a free tetrahedral mesh and setting in COMSOL an element size of "extra fine", which leads to the reported distributions. It can be noted that there is only one element along the thickness of the device. Considering that the wavelength is, for ka=1, $\lambda = 6.28cm$ and that, for representing correctly results in numerical simulations, at least 6-7 elements per unit wavelengths have to be modelled inside the device, the situation seems good. The mesh for the real device was harder to create, as the particularly complex geometry didn't allow too much refinement with the available RAM in our PC. The correspondent mesh is reported in figure 5.7. This mesh has been built by setting an "extra fine" element size on the surface of the device with the "edge mesh" command, which was then exploited to create a free tetrahedral mesh. Even here, along the thickness there is only one element but, since the tested wavelength is equal to the case of S_0 waves, is considered sufficient even in this case. Having cleared that, let's start the overview from S_0 waves. Figure 5.8 reports the comparison between the analysis made on the real device and on the layered device. Overall, the behaviour is correctly grasped by both geometries. There are, however, some differences. By looking at the aforementioned results, it is pretty clear that the focusing point is more localized in the real analysis. On

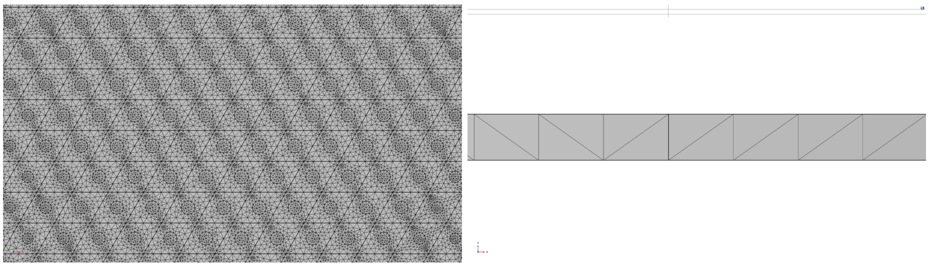

Figure 5.7: Graphical representation of the mesh used for the real Luneburg device.

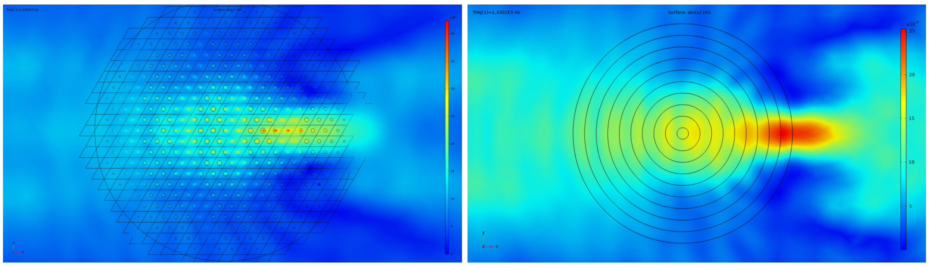

Figure 5.8: Graph of the absolute value of displacement registered, along the x direction, for the S_0 wave propagation case when $ka = 1$. Left: real device. Right: layered device.

the other hand, the layered analysis proves to be more in line with what should occur in theory since focusing is predicted at the lens' edge, though it seems distributed along a greater area. To further comment on those findings, the line plot of the absolute value of displacement along x, at y=0, is reported in figure 5.9 for both geometries. For what concerns the trend of displacement across the whole device, the analysis gives back satisfactory results in both geometries, as the maximum point is reached by gradual amplification, rather than with a more abrupt behaviour. What has been underlined before on the focusing point position is even more evident here. While the real geometry reproduces a focusing point at x=40cm, so with a 5cm discrepancy over theoretical derivations, the layered device places it at x=43cm, a much better fit. Another difference between the two analyses lies in the amplification of displacement registered: while the real device predicts a 3.5x magnification, with respect to the maximum amplitude of displacement of the input, the layered geometry predicts a 2.2x. Having discussed the behaviour of the device for ka=1 and the S_0 mode, before making final considerations, the next step is to review the A_0 mode at the same wavenumber. In figure 5.10 the surface plot showing the absolute value

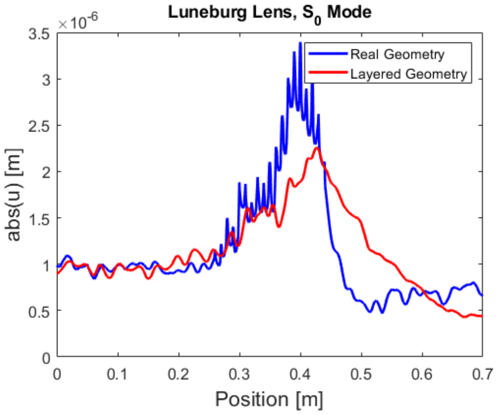

Figure 5.9: Comparison of the absolute value of displacement, in the x direction and calculated along the y=0 line, for the two different geometries testing the S_0 mode at ka=1.

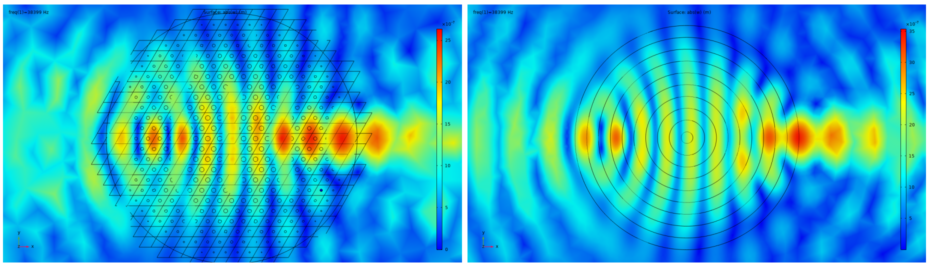

Figure 5.10: Graph of the absolute value of displacement registered, along the z direction, for the A_0 wave propagation case when $ka = 1$. Left: real device. Right: layered device.

of displacement, along the z direction, for both real and layered geometry is reported. For the A_0 case it can be noticed that the two simulations are better in agreement, as it was already underlined even for the GRIN plate, probably due to a mesh which is more toward convergence than it is for the S_0 mode. In particular, the analyses show similar strong points and flaws. The focusing point is correctly localized at the end of the device for both, placed at x=44cm, while the theoretical point is located at x=45cm, so the theory-simulation agreement on this front is good. The greatest problem encountered involves the overall displacement trend inside the device. In fact, this becomes clearer by looking at figure 5.11, which proposes a comparison between the line plots, graphed on the y=0 line, of the absolute value of displacement, along the z direction, for both geometries. While it has already been stretched that the focusing point position is good, the behaviour before reaching the focusing point is a bit unusual here, as an amplification is registered even toward the entrance of the device, and its magnitude is not even negligible. In fact, if the focusing point predicts a 3.1x magnification effect with respect to the maximum displacement amplitude given as input, which was $1\mu m$, such point shows a 2.9x increment, which should not

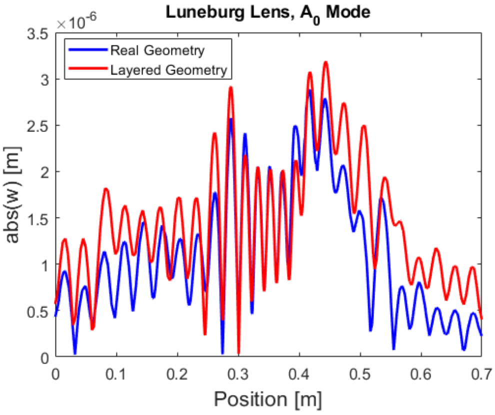

Figure 5.11: Comparison of the absolute value of displacement, in the z direction and calculated along the y=0 line, for the two different geometries testing A_0 waves when ka=1.

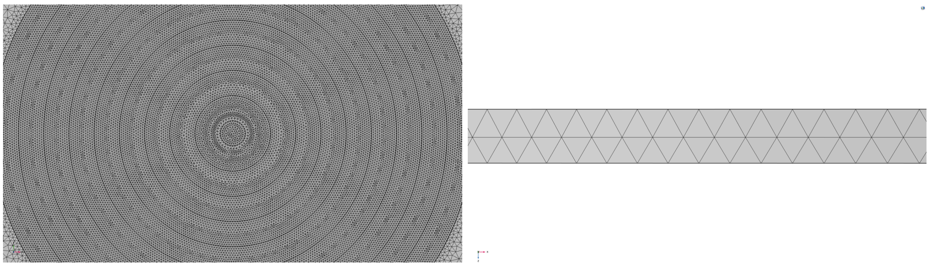

Figure 5.12: Graphical representation of the refined mesh for the layered device.

be as prominent as it is. However, on the bright side, both devices show similar trends, apart from the small discrepancies in displacement magnitude, which indicates a convergence for the two meshes for A_0 wave propagation. Concluding, this first frequency analysis showed a behaviour which is in line with what has been found before for the GRIN device: while the S_0 mode tends to show larger discrepancies testing the two different geometries, the two A_0 mode analyses tend to agree better. This behaviour is attributed, even here, to the poor mesh of the real device which, especially for the bad refinement in the xy plane, shows its limits. Although it is able to predict greater displacement magnification values than the one of the layered device, the overall predicted behaviour is further from the ideal one. To better sustain this conclusion, a refinement on the layered mesh is proposed, since it's easier to produce denser meshes with homogeneous layers than it is for the real device. In particular, the "new mesh" for the layered device is proposed in figure 5.12. It can be noticed that the mesh has been refined manually both in the xy plane, where it was built by using a free triangular mesh on the surface as a base for a free tetrahedral one, and even along the thickness, where the number of elements doubles, going to two. Testing only the S_0 mode, since is the only one with severe discrepancies between geometries, in figure 5.13 a comparison between line plots of absolute

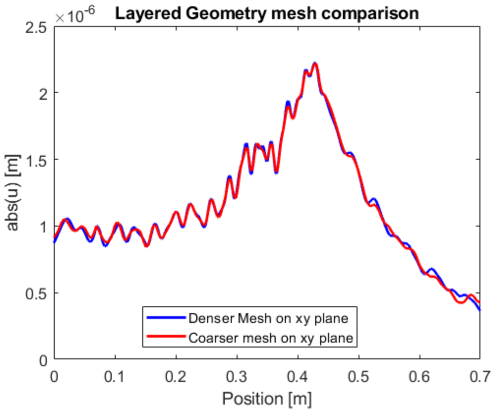

Figure 5.13: Graphical comparison of the absolute value of displacement, along the x direction, drawn at the y=0 line, between the two differently built meshes testing the S_0 mode at ka=1.

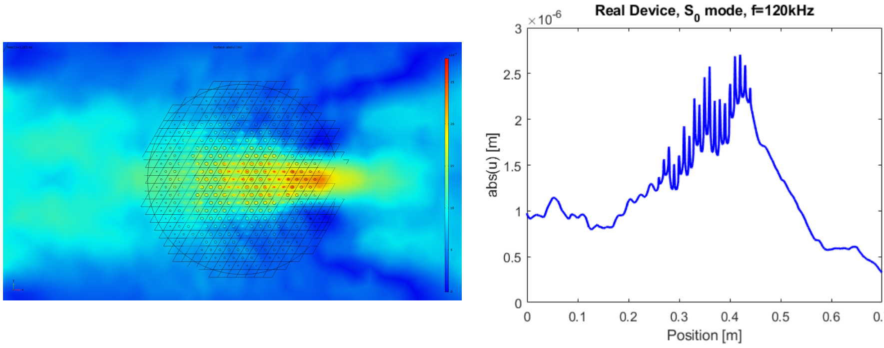

Figure 5.14: Plots of the absolute value of displacement, along the x direction, when testing the S_0 mode on the real device at a frequency of 120kHz.

value of displacement along the x direction, taken at y=0, is proposed. We can clearly see that, no matter the great refinement that has been made on the mesh, results are absolutely the same. So, the poor agreement is attributed to the real device but, again, with the given computer further refinement on that mesh is not possible. Going on with the analysis, the next step is to review the frequency ranges of those devices. As before, the aim is to see if, first, the frequency range validity is confirmed by numerical simulations or if discrepancies arise. Second, we check the range to see if the behaviour, this time especially for the A_0 mode, can be bettered at other frequencies. For what concerns ranges, as it has been explained in chapter 4 for the GRIN device, the effective medium theory places two constraints on the minimum and maximum wavelength for the device to work properly. The minimum constraint in wavelength is set such that $\lambda \geq 3 - 4a$, otherwise the homogenization theory cannot correctly simulate the device. The maximum is set to avoid that diffraction dominates over refraction, as $\lambda \leq 20a$, which is the total dimension of the device. Taking into account that the range will be different, as the two dispersion relations are unequal, it is obtained $4kHz < f < 170kHz$ for the A_0 mode and $42kHz < f < 280kHz$ for the S_0 mode. Starting with an overview of the performances of the S_0 mode, we consider the real device. In this case, results are poor, to say the least. The

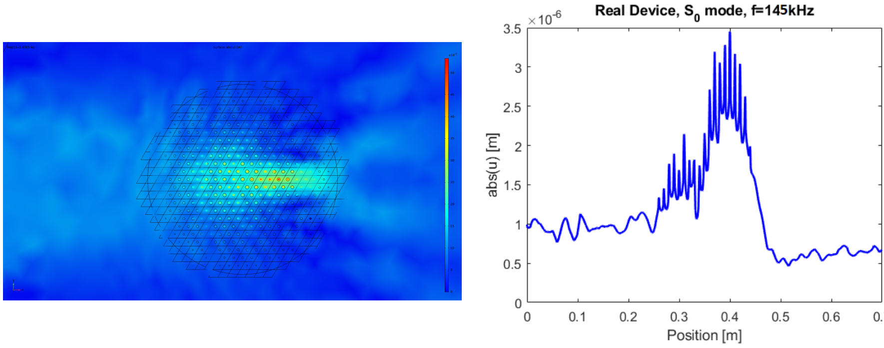

Figure 5.15: Plots of the absolute value of displacement, along the x direction, when testing the S_0 mode on the real device at a frequency of 145kHz.

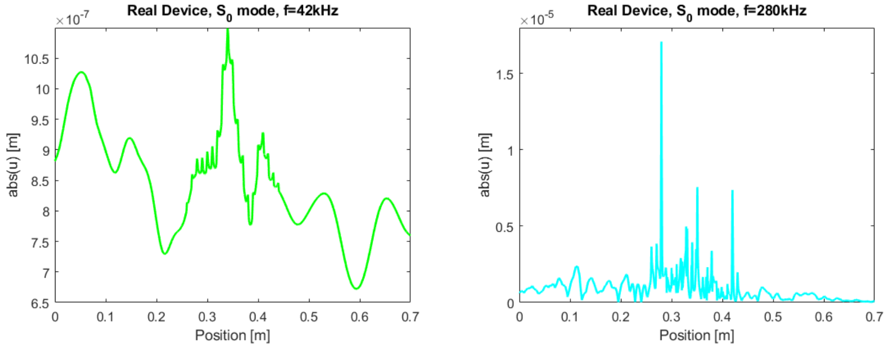

Figure 5.16: Simulation results showing the absolute value of displacement along x, at the y=0 line, for the real geometry device testing the S_0 mode at frequencies correspondent to the theoretical limits. Left: lower theoretical limit. Right: upper theoretical limit.

minimum limit is found to be 120kHz and its results are reported in figure 5.14. In this case, the focusing point is shifting a bit toward the edge of the lens, at x=42cm, so a slightly better fit than the $ka = 1$ case. However, here some peaks in the centre of the device start to arise with amplitudes which are not negligible, a clear sign that the accuracy of reproduction of results is starting to fade. On the other hand, the highest frequency at which the device works is 145kHz, for which the results are reported in figure 5.15. It can be noticed that, although the device works, it shares the same problems underlined in the overview of the working principle for $ka = 1$. Especially, the focusing point is a bit shifted from its theoretical position, positioned at x=40cm, but the magnification effect of 3.5x and the gradual increment in displacement amplitude are a good fit. Although the overall behaviour of each single analysis for S_0 waves in the real device is not the worst seen, still this results seems poor, at least compared to the theoretical range, much more wider. To further prove that the range is more shallow, figure 5.16 reports line plots, of absolute value of displacements, for the real geometry and the S_0 wave propagation test at the limiting frequencies predicted by the theoretical range. At the low theoretical

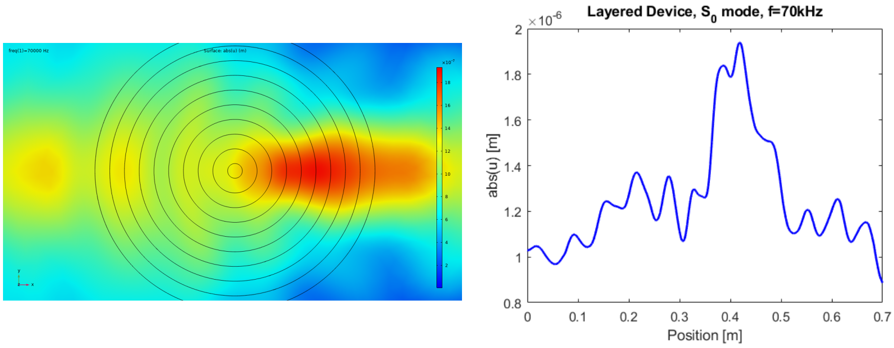

Figure 5.17: Plots of the absolute value of displacement, along the x direction, when testing the S_0 mode on the layered device at a frequency of 70kHz.

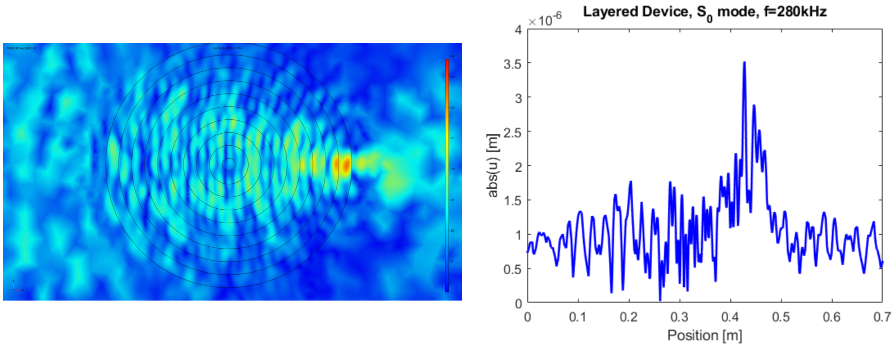

Figure 5.18: Plots of the absolute value of displacement, along the x direction, when testing the S_0 mode on the layered device at a frequency of 280kHz.

frequency limit, represented by the green plot, the analysis shows completely wrong behaviour, with no amplification registered at all, as the maximum amplitude reached is equal to the maximum given as input. On the other hand the upper frequency limit, represented by the light blue plot, shows a behaviour which is not intended, with very sharp and localised peaks not to be attributed to focusing. Switching to the layered device description, always for the analysis of the S_0 mode, the following is found. The low limit is not matched, and the lowest frequency with acceptable results, reported in figure 5.17, is 70kHz. At this frequency, the peak is still clearly visible, although spread over a greater area. The magnification of displacement is going down a bit, compared to the result for high frequencies, with an expected 2x. The upper limit, on the other hand, is correctly matched, as reported in figure 5.18. In particular, from the images it is pretty evident that the focusing point is present and placed at a reasonable coordinate, with x=43cm. The magnification effect predicted is very good, with a 3.5x with respect to the maximum amplitude of the load given. It can also be noted, however, that the overall trend of the analysis starts to

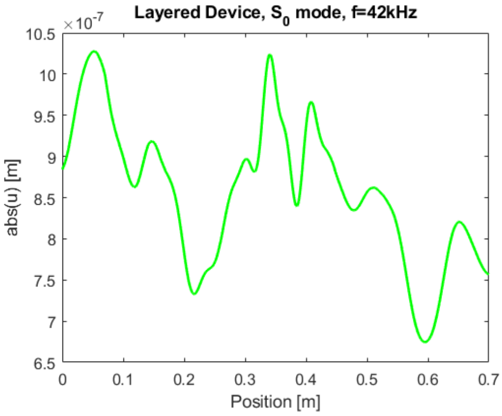

Figure 5.19: Simulation result showing the absolute value of displacement along x, at the y=0 line, for the layered geometry device testing the S_0 mode at a frequency correspondent to the theoretical lower limit.

Table 5.5: Comparison, between theoretical ranges and discovered ones, for the S_0 mode.

Theoretical Range	**Real Geometry**	**Layered geoemetry**
42kHz<f<280kHz	120kHz<f<145kHz	70kHz<f<280kHz

become more blurry, especially looking in the left image of figure 5.18, meaning that effectively this setup is starting to show some difficulties in the numerical simulation, emphasizing the limit of the homogenization theory employed here. To further emphasize that the theoretical low frequency limit is not matched, figure 5.19 reports results of the simulation at that frequency value, which is 42kHz. From the green plot, it is pretty clear that the lens does not work, as the peak is absent and, again, no magnification of displacement is detected anywhere in the device. To summarize better results for the S_0 mode propagation, table 5.5 proposes a comparison between the ranges found with numerical simulations and the one found by theoretical derivations. The difference between the two geometries here is particularly evident: while the real device predicts a shallower range, the layered one allows to reproduce way better the phenomena. Focusing on the real device, the low frequency limit corresponds to $\lambda = 6.96a$, while the maximum limit in frequency corresponds to $\lambda = 5.76a$. On the other device, the low frequency limit of 70kHz corresponds to $\lambda = 11.93a$, a much better fit. The reason for this is attributed to the poorly refined mesh of the real device, compared to the one of the layered device. Having reviewed the S_0 mode, we go on by analysing the A_0 mode. The first device analysed, again, will be the real geometry. Sadly, even in this case the real device fails to match the theoretical lower frequency limit, which is found to be 20kHz and corresponds to a wavelength of $\lambda = 8.7a$. Particularly, in this case the simulation, reported in figure 5.20, is starting to show its limitations. As it was underlined for the analysis at ka=1, simulations at low frequency for the A_0 mode tend to show peaks even before the focusing point, as it can be noticed even here, which is a clear sign that the analysis is diverging from its intended behaviour. Another remark of this conclusion derives from the comparison of the heights of the two peaks present, which is very similar. Figure 5.21 reports the results for the upper frequency limit, found to be 90kHz, so even the upper limit in frequency

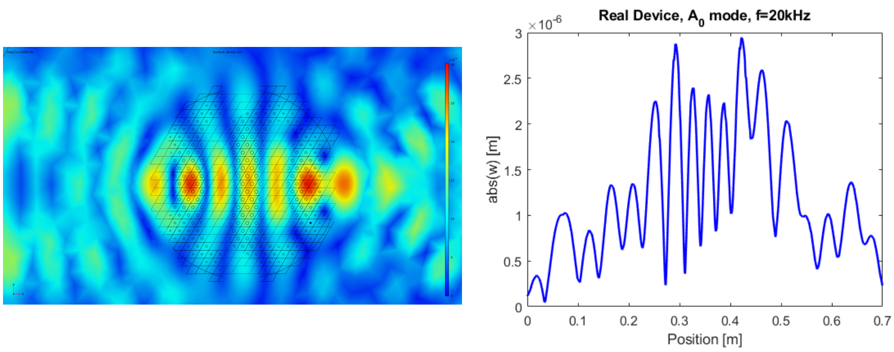

Figure 5.20: Plots of the absolute value of displacement, along the z direction, when testing the A_0 mode on the real device at a frequency of 20kHz.

is not matched. Looking at the bright side, though, in this analysis the device behaves definitely better than in the case for ka=1. Here, the simulation shows a gradual increment toward the absolute maximum, which is located at x=42cm,

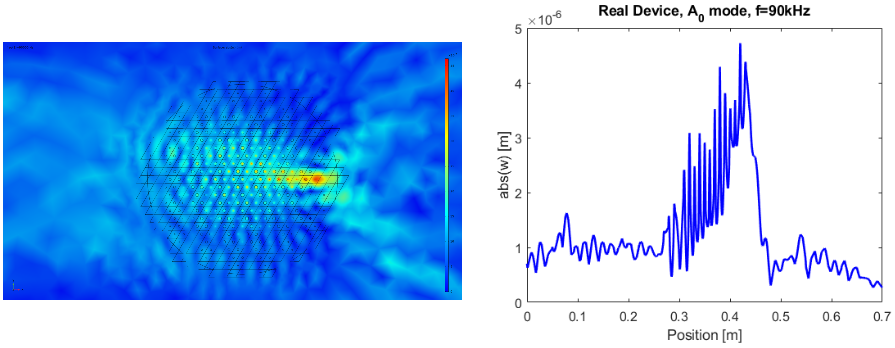

Figure 5.21: Plots of the absolute value of displacement, along the z direction, when testing the A_0 mode on the real device at a frequency of 90kHz.

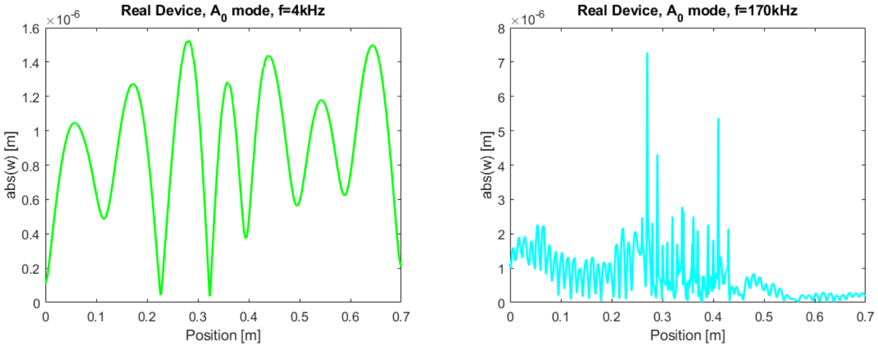

Figure 5.22: Simulation results showing the absolute value of displacement along z, at the y=0 line, for the real geometry device testing the A_0 mode at frequencies correspondent to the theoretical limits. Left: low theoretical limit. Right: high theoretical limit.

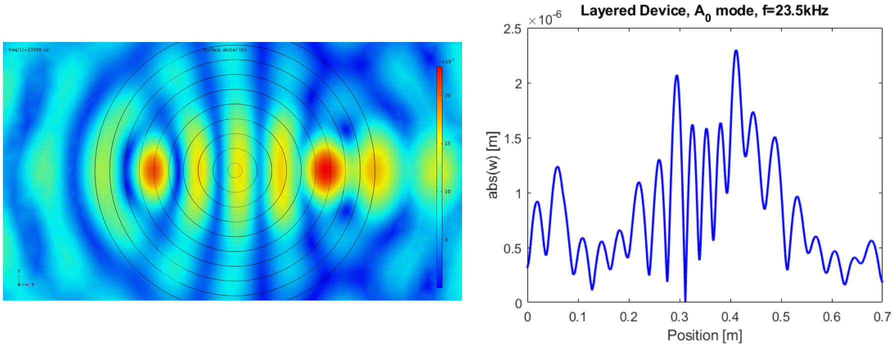

Figure 5.23: Plots of the absolute value of displacement, along the z direction, when testing the A_0 mode on the layered device at a frequency of 23.5kHz.

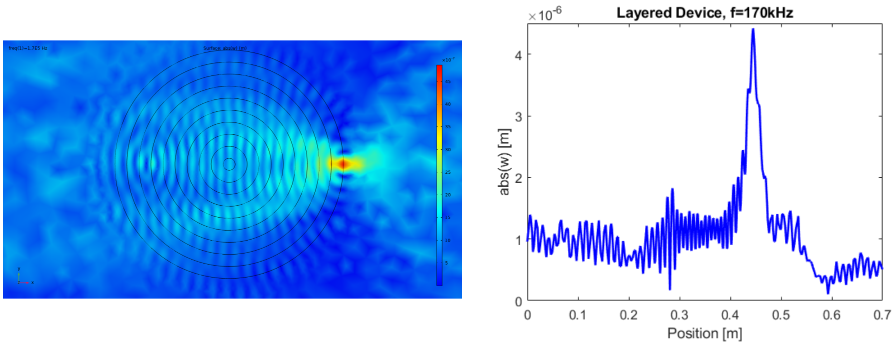

Figure 5.24: Plots of the absolute value of displacement, along the z direction, when testing the A_0 mode on the layered device at a frequency of 170kHz.

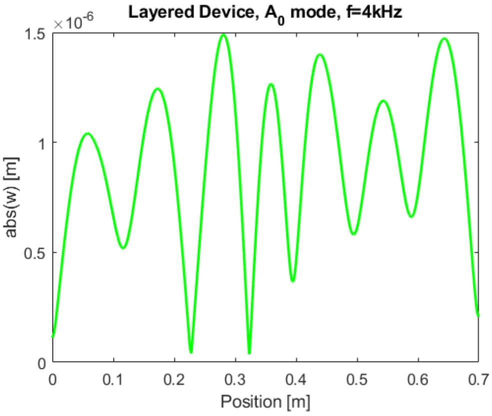

Figure 5.25: Simulation result showing the absolute value of displacement along z, at the y=0 line, for the layered geometry device testing the A_0 mode at a frequency correspondent to the theoretical lower limit.

so still on the left of the theoretical point, but an overall not bad fit. Even the amplification effect with respect to the maximum amplitude of the starting input is great, with a 4.75x magnification. To further demonstrate that the theoretical limits are not respected, analyses at that frequencies are reported in figure 5.22. The low frequency limit, reported in the green graph, shows a flat behaviour, as if no lens was present, but this is a common problem for all low limits. The upper limit, pictured in the light blue graph, shows peaks which are not to be attributed to focusing. Finally, the results for the layered device and A_0 mode are presented. As it has been proven before for the S_0 mode, the upper limit is correctly matched by the analysis, while the lower one is not. The first frequency which starts to show the correct trend is 23.5 kHz, reported in figure 5.23. In this case, the device behaves similarly to its real counterpart, predicting a trend of magnification which is not very great, as a peak in displacement is localised not only toward the end of the device, but even inside it, which is an indicator of some problems in the analysis. This value corresponds to a wavelength of $\lambda = 8.11a$, lower than the theoretical value. On the other

Table 5.6: Comparison, between theoretical ranges and discovered ones, for the A_0 mode.

Theoretical Range	**Real Geometry**	**Layered geoemetry**
4kHz<f<170kHz	20kHz<f<90kHz	23.5kHz<f<170kHz

hand, the upper theoretical limit is matched, at 170kHz, and results are reported in figure 5.24. Clearly, this frequency shows much better agreement with the intended behaviour of the device than the case for $ka = 1$. The focusing point is small and localised, positioned at x=44.5cm. Even the overall trend is very encouraging, as the increase in displacement amplitude is gradual toward the focusing point, where an absolute maximum is achieved. The amplification factor is also pretty great, with a 4x magnification on displacement. To prove that the low theoretical limit is not matched, figure 5.25 reports the analysis made at that value of frequency. There, as pointed out even for all other devices, simulations show a behaviour as if no lens was present. To summarize, table 5.6 reports the comparison between the theoretical range and the one found in numerical simulations for the A_0 mode. Even here, the layered device behaves much better, matching the upper limit and missing only the lower one. The real device, as before, misses both theoretical limits but, this time, predicts a wider range of frequency, in line with what has been found for the GRIN devices built with the same effective medium theory. Having described the behaviour of the device in terms of focusing and theoretical ranges, the next step will be dedicated to demonstrate a particular feature of this lens. In chapter 2, where a section is dedicated to the working principles of lenses, it has been highlighted that Luneburg devices are omnidirectional. This means that, no matter where you place the input, so long as it's applied correctly, the output rotates accordingly. The following analysis tries to prove this feature by performing a rotation of the line on which the input is given by 45°, as pictured in figure 5.26. This test is going to be performed on the layered geometry only as it's the geometry which delivers the most consistent results overall. Analysing results, starting with the S_0 mode, the surface plot of absolute value of displacement, when the input is 45° rotated, is reported in figure 5.27. We can see that the behaviour of the device is exactly the one that was expected: the output rotates

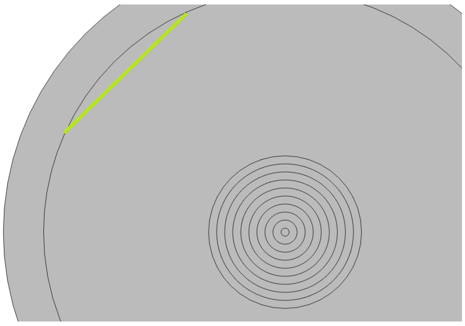

Figure 5.26: Graphical representation of the rotated area where the input is going to be set.

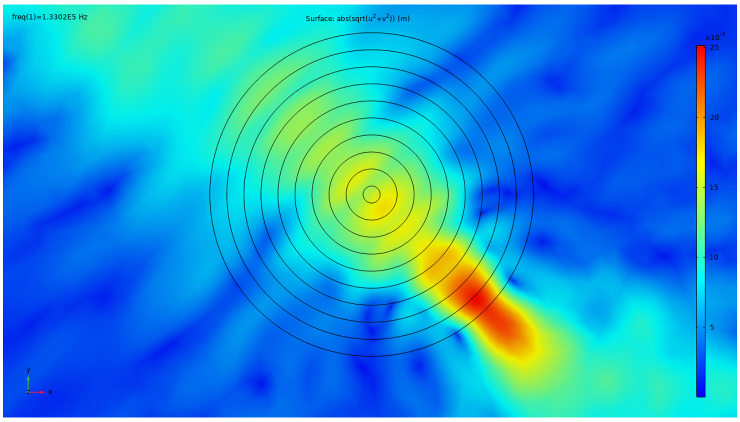

Figure 5.27: Surface graph showing the absolute value of displacement, for the layered geometry, testing S_0 waves coming from a rotated input position.

according to the input, as now the focusing point is 45° rotated. Comparing the absolute value of displacement, along the x direction and taken at the y=0 line, for both the original case and the tilted input one, as done in figure 5.28, we can see that the analysis is exactly the same, as these plots superimpose clearly without severe discrepancies. Repeating the analysis for the A_0 mode propagation, similar results are expected. Figure 5.29 reports the surface plot for the case when the input is rotated. Again, even here the plot shows exactly what could be expected, as the output rotates accordingly to the input position. Figure 5.30 reports a comparison between line plots, this time representing the absolute value of displacement along z, for the original case and the rotated one, confirming even more the idea that the two analyses are absolutely the same.

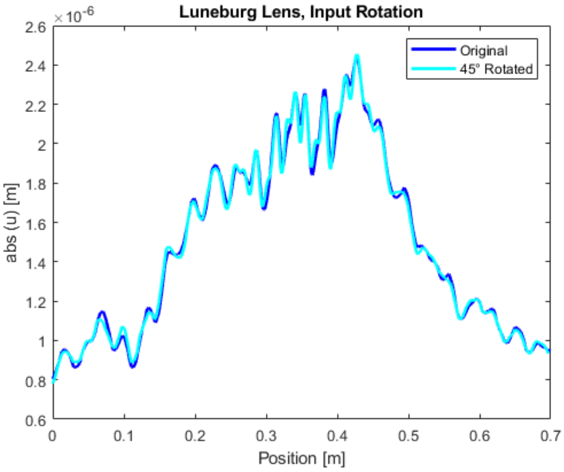

Figure 5.28: Superposition of different plots of absolute value of displacement, which put in comparison the result of the original test with the one of the 45° rotated input case.

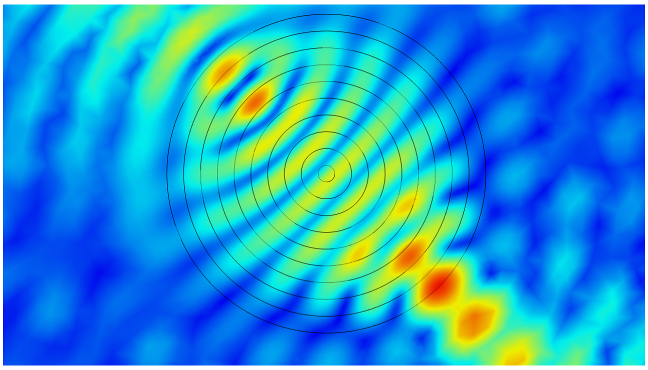

Figure 5.29: Surface graph showing the absolute value of displacement, for the layered geometry, testing A_0 waves coming from a rotated input position.

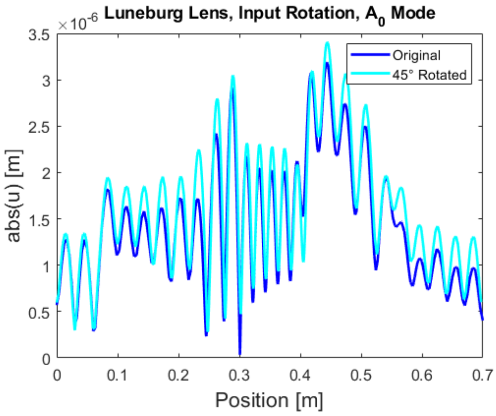

Figure 5.30: Superposition of different plots of absolute value of displacement, which aims at comparing the result of the original test with the one of the 45° rotated input case.

The last frequency analysis has been dedicated to try and place the input in a different configuration. The idea was to apply the input no more on the line highlighted in figure 5.5, but to apply it on a circumference's arc of a defined radius. The idea was that, if the device correctly recognised the input, there could, theoretically, be a larger focusing spot, spread on the edge of the device. Figure 5.31 reproduces the idea in a more graphical way: the blue line covers the area where the the input, which will be applied radially, is going to be placed, while the orange arc represents the hypothetical focusing region if the device recognises the input correctly. This trial is done only on the layered device and for the S_0 mode, for a frequency of $f = 133kHz$. Figure 5.32 reports the results of this trial, where the input has been applied on half the circumference's arc.
The results clearly show that something is wrong here. The focusing behaviour of the lens is gone completely, and the simulation shows results as if there was no lens at all. In fact, since the displacement was applied radially toward the centre, simulations show its concentration at that exact central spot, with no deviation effect to be attributed to the lens detected at all. Then, the following

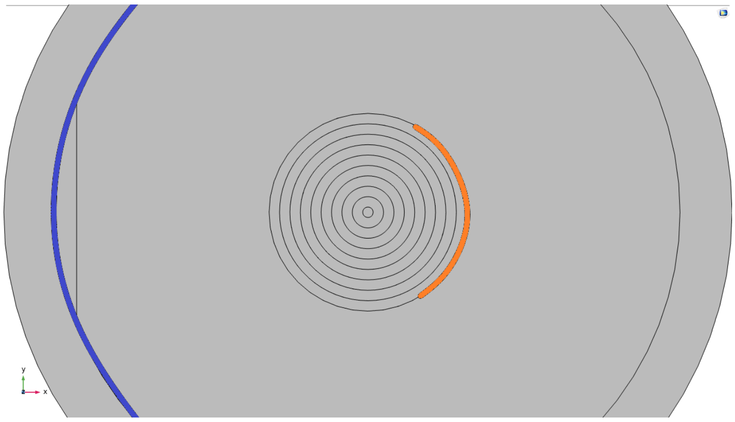

Figure 5.31: Graphical representation of the idea behind the last test.

try was to see if a less wide arc of circumference shows more encouraging results. Results, analysed always for a layered plate on the S_0 mode, are shown in figure 5.33, where the imposition of the displacement is done on a circumference's arc of 40° on the left and 60° on the right. Neither of these simulations show an extended focusing point, but it can be clearly noticed that the device's behaviour changes dramatically between the two simulations reported. On the left, the device works better: the focusing point is placed correctly toward the lens' edge and the maximum amplitude of displacement is reached there. However, taking as a reference results obtained when applying the input on a straight line, there are some discrepancies. Particularly, the focusing point shifts toward the inner part of the lens, becoming x=41cm from the lens' left edge in spite of x=43cm found when applying the input on a straight line, which was a better fit with theoretical findings. The displacement amplitude remains almost unchanged. Increasing the arc's width, the situation worsens badly, as the point shifts toward the centre of the lens, placed exactly at x=35cm, which is the middle point

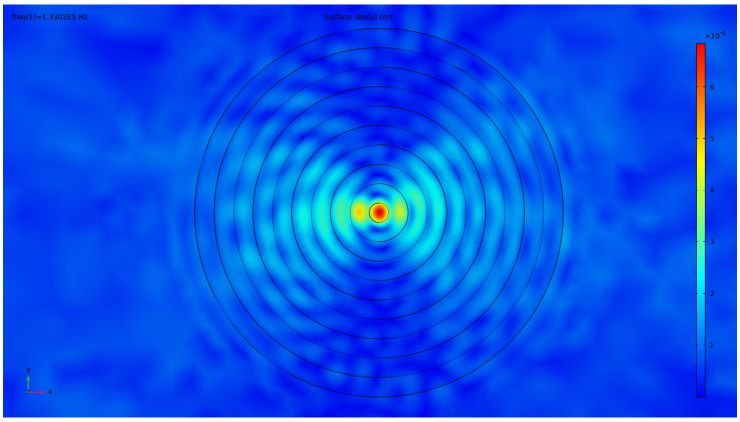

Figure 5.32: Surface plot of the absolute value of displacement registered by the numerical simulation if the input is put on half the circumference's arc.

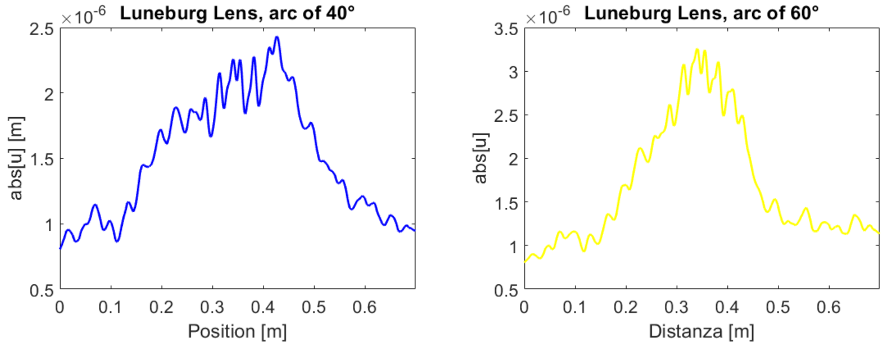

Figure 5.33: Graphical representation of the absolute value of displacement, along the x direction, at the y=0 line, changing the application of the input. Left: 40° arc. Right: 60° arc.

of the device. Not only that, but the displacement magnification increases to 3.2x. Remembering that, for the half arc case the concentration of displacement on the centre of the device was 6x, it becomes clear where the simulation is going. This is even more evident if we make a close comparison between different arc length cases superimposed in one graph, as seen in picture 5.34. It can be noticed that there is a progressive trend on these analysis. Increasing the arc length, the focusing point shifts toward the inner part of the lens and it increases in magnitude, as it can be clearly seen in this graphical comparison. This is to be attributed exactly to the input. As we increase the arc's length, the device progressively doesn't recognise anymore the input as correct and tends to shift from a behaviour where focusing is still appreciable, even though on a

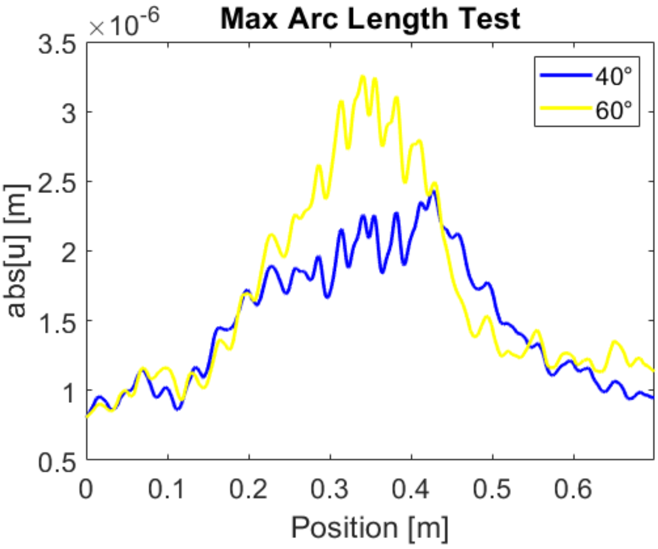

Figure 5.34: Superposition of different plots of absolute value of displacement, taken along the y=0 line, for an input applied over different arc lengths.

single point, to a point where the presence of the lens is completely ignored, as the radial input is not seen by the lens. So, having shown that the problem is this input, clearly the lens works only with planar wavefronts and the focus can only be a localized point, so the idea of extending the focusing point position is completely discarded. Proven that, though, the silicon and lead device works as intended for some frequencies, those will be put to test in time domain simulations.

5.3 Time Domain Analysis

Having discussed the focusing properties of this lens, the next step is to review time domain analysis. In this case, the aim is to first check if informations emerged from frequency domain analysis converge to what is found here. Then, as it has been done for the GRIN device, a multi-frequency test will be carried out, to see if the device correctly recognises a non monochromatic input. Last, a possible prototype for energy harvesting is reviewed and analysed. The setting for all these analyses is not changed: the lens is still put inside a 35cm radius cylinder and absorbing boundary conditions are applied along the cylinder's external thickness, to avoid that reflected waves become an issue for the discretization of the phenomena. What will change, though, is the application of the input, depending on the analysis considered. The first analysis considered will aim at confirming the behaviour that frequency analysis have predicted in the previous section by checking that the informations collected on focusing are retrieved even here. Due to the higher mesh precision, tests will be carried out only on the layered geometry. Previously, the input has been applied as a sinusoidal wave of constant amplitude equal to $1\mu m$, so the input was not changing in time. For this first analysis, the input will be set as a sine burst load com-

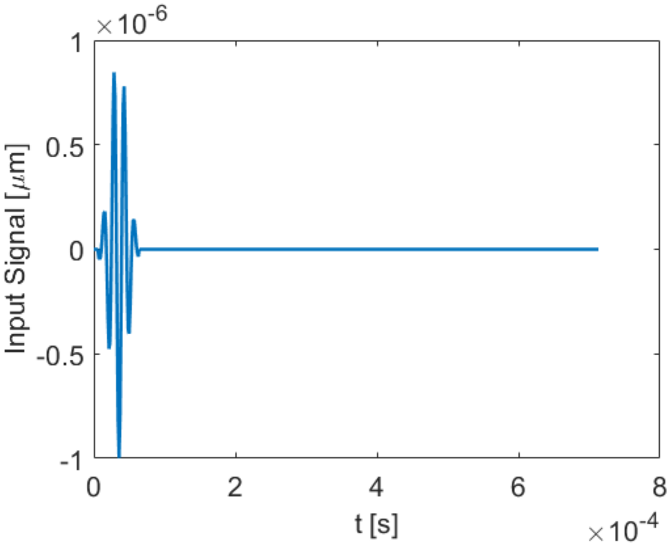

Figure 5.35: Graphical representation of the sine burst load used in time domain simulations.

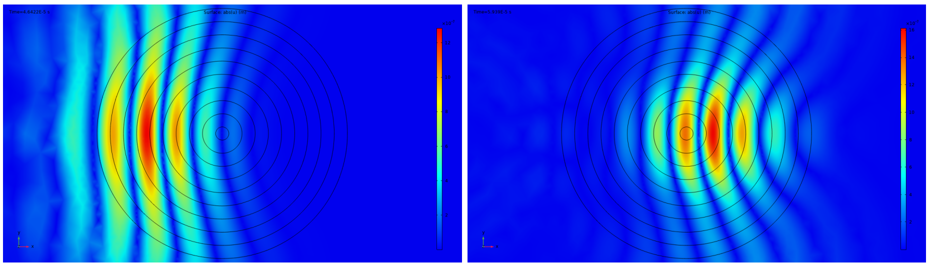

Figure 5.36: Surface plot of the absolute value of displacement, along the x direction, registered at different time frames, for the layered device testing the S_0 mode. Left: $t = 4.64 \times 10^-5s$. Right: $t = 5.93 \times 10^{-5}s$.

posed of 4 cycles of sinusoidal displacement, centred at a given frequency. The input has been calculated with a MATLAB script and its appearance, for a frequency of 133kHz, is reported in figure 5.35. This allows to better see the focusing point in time domain simulations, as we can see waves focusing along their path in a more clear way. The overview of results starts form the test of the S_0 mode. In this case, the device has been tested with a sine burst load centred at 133kHz, to better compare it with the previously discovered results in the frequency domain. Figure 5.36 reports the surface plot of the absolute value of displacement, along the x direction, for two different time frames. Here the effect of the lens is particularly clear, as waves are bent as they progress inside the device, which is a direct consequence of the refractive index tuning operation. Remembering that, for frequency domain analysis for the S_0 waves, results predicted a focusing point placed at x=42.5cm, the next step is to see if, even here, the point is moved back inside the lens. Figure 5.37 reports plots of the absolute value of displacement at the instant at which waves cross the reported coordinate for focusing in the frequency analysis. The magnification effect, with respect to the maximum displacement value of the input, is registered as 2x. This value is in line with what has been found in the previous frequency analysis. Furthermore, if the same plots are taken when waves hit

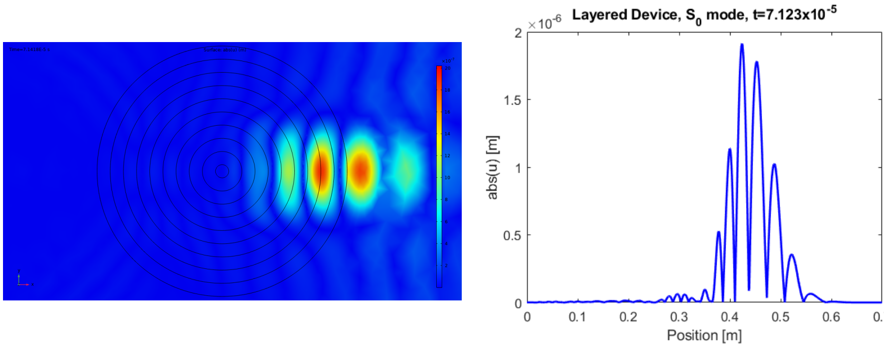

Figure 5.37: Plots of absolute value of displacement, along the x direction, taken at a time frame of $t = 7.14 \times 10^{-5}$ when testing the S_0 mode on the layered device.

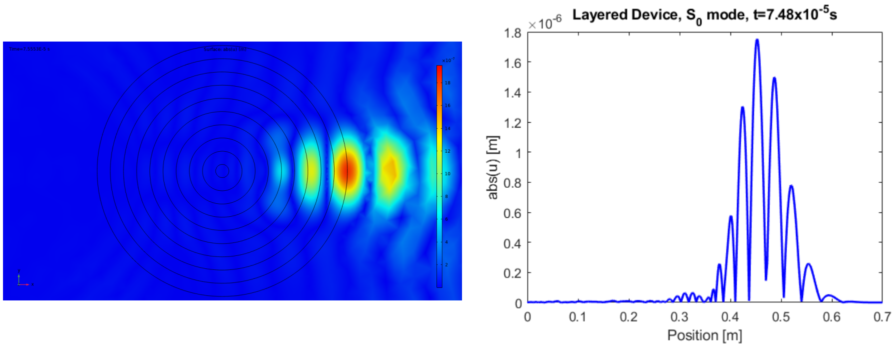

Figure 5.38: Plots of absolute value of displacement, along the x direction, taken at a time frame of $t = 7.55 \times 10^{-5}$ when testing the S_0 mode on the layered device.

the lens' edge, as figure 5.38 shows, the magnitude of displacement goes down to 1.7x, which confirms the idea that focusing takes place a bit on the left with respect to the lens' theoretical focusing point. Having discussed the S_0 mode and demonstrated that the simulation behaved as predicted, the next step will be the review of the A_0 mode. In this case, we test the device with a sine burst centred at 170kHz, since it was clear from the frequency range analysis that, at this frequency, results are particularly promising. Figure 5.39 reports the surface plot of the absolute value of displacement for different time steps. The focusing behaviour can, even here, be clearly seen, as waves are bent toward the diametrically opposed point with respect to the entrance one. The time at which the maximum amplification effect is registered is reported in 5.40 where, thanks to another surface plot of the absolute value of displacement, we can see waves converge in the required area at the lens' edge. In this case the point in which maximum displacement is found is much more closer to the lens' edge, reported at a coordinate of x=44.5cm. The amplification of displacement, in this case, with respect to the one of the given input, is 4x. All this information correspond to what has been obtained in frequency domain analysis. So, even for A_0 waves, informations found here are in line with what has been underlined in the previous section, highlighting the convergence of information between do-

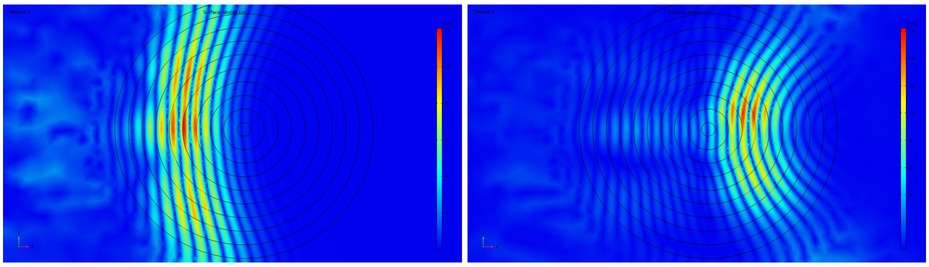

Figure 5.39: Surface plot of the absolute value of displacement, along the z direction, registered at different time slots, for the layered device testing the A_0 mode. Left: $t = 6 \times 10{-}5s$. Right: $t = 8.32 \times 10^{-5}s$.

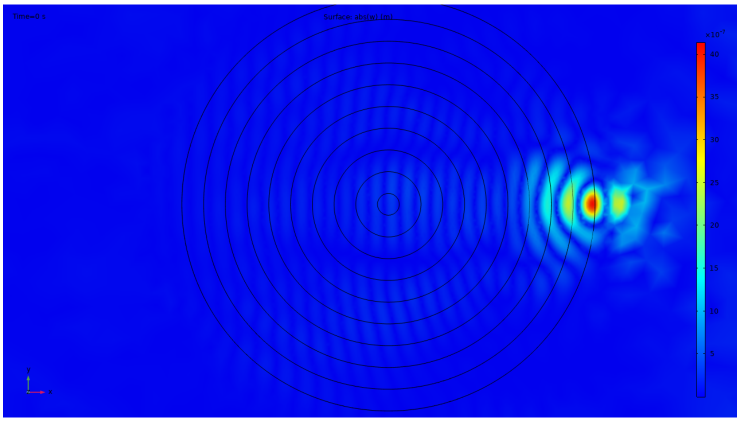

Figure 5.40: Surface plot of the absolute value of displacement, along the z direction, for the layered device testing the A_0 mode at time $t = 1 \times 10^{-4}$.

mains, which is a great result. Having reviewed the behaviour of the device in time domain when tested with a sine burst load, the next step will be aimed at trying to see if non monochromatic inputs are correctly recognised by the device. To do that, a new input has been generated. It consists of some cycles of sinusoidal displacement which varies its frequency in time. In particular, the input starts at a given frequency at $t = 0$ and is set to increase linearly the frequency up to a second time frame t_1. Of course, the test of S_0 and A_0 modes will involve differently built inputs, as their ranges are different. To prove this feature, the input is tested in a frequency window of 10kHz. The graphical representation for the input given when testing the S_0 mode is reported in figure

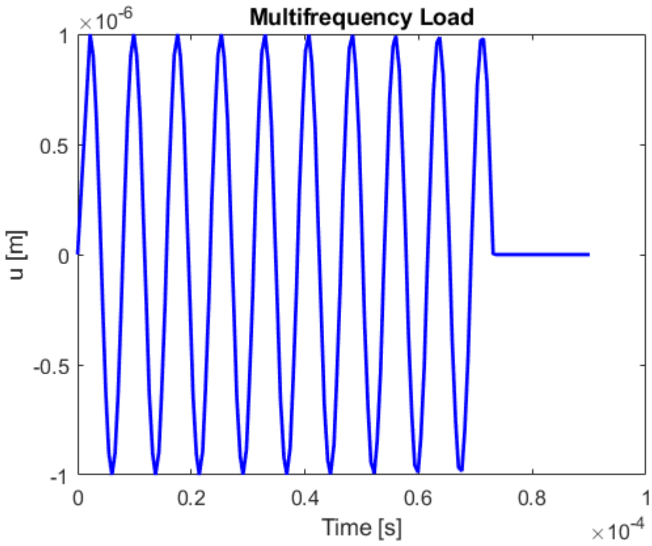

Figure 5.41: Graphical representation of the multi-frequency input given for the S_0 mode testing.

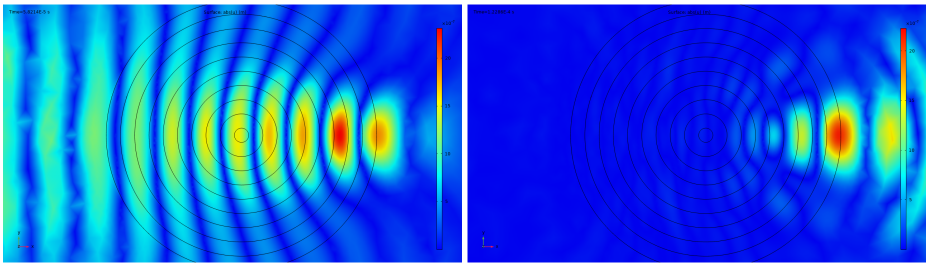

Figure 5.42: Surface plots, taken at different time frames, showing the absolute value of displacement, along the x direction, when testing the S_0 mode with a multi-frequency input. Left: $t = 5.8214 \times 10^{-5}$. Right: $t = 1.22 \times 10^{-4}$.

5.41. The input starts at $t = 0$ with a frequency of 130kHz, which arrives at 140kHz at time $t = 7 \times 10^{-5}$. Having described the multi-frequency input, the next step will be the test of such input. Starting with the description of time domain analyses on the S_0 mode, figure 5.42 reports the correspondent results. The images reported have been taken at two time frames correspondent to the first and last time instant at which the input strikes the device. It can be seen that, notwithstanding the multi-frequency nature of the input, the behaviour represented is the correct one and has been kept from the start to the end of the simulation, as expected. Similar results have been recorded even for the A_0 mode. There, the test has been performed by using a load similar in form to that represented in figure 5.41, but obtained by changing the frequency span from 40kHz to 50 kHz. Results are reported in figure 5.43. Even here it can be noticed that the simulation correctly reproduces the phenomena from the first time frame to the last one. It is even recognisable, from the right image, that there is a spot, on the left part on the lens, where waves concentrate lightly. This phenomena was present even in frequency simulation where, near the entrance of the lens, a peak was visible, once again underlining the convergence between all different analyses. Having confirmed the multi-frequency functioning of the device, the last test that will be reported here involves simulating the same layered geometry with the addition of a beam, which is put to resonance with the frequency of the input. The idea, in this case, is to test if such a configuration allows to localise the energy that waves carry. If such supposition

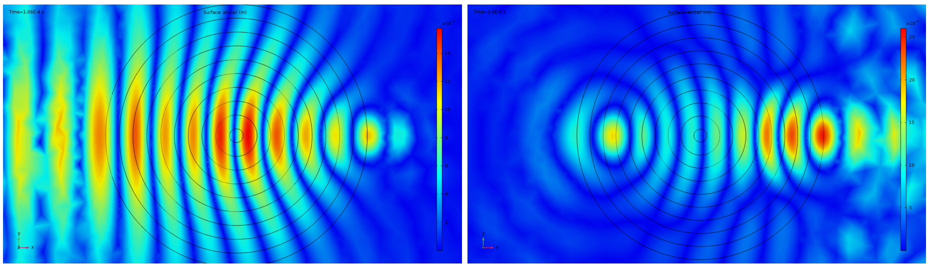

Figure 5.43: Surface plots, taken at different time frames, showing the absolute value of displacement, along the z direction, when testing the A_0 mode with a multi-frequency input. Left: $t = 1.06 \times 10^{-4}$. Right: $t = 3.4 \times 10^{-4}$.

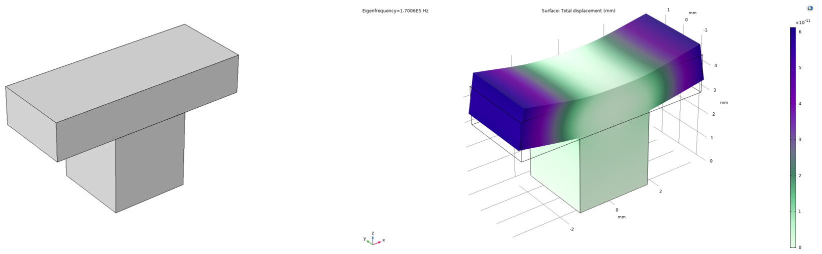

Figure 5.44: Beam used in the time domain simulation. Left: final CAD representation of the beam's geometry. Right: Eigenfrequency analysis showing the flexural mode activated at 170kHz.

is true, then the application of a piezoelectric layer over the beam would ensure energy harvesting capabilities with a good efficiency, which is vital. This test will be performed only on the A_0 mode propagation, since the aim is to test EH performances via the activation of the d_{31} mode of the piezoelectric layer, so flexural waves will be employed. The test is carried out at two different frequencies, to see if results change. The selected frequencies are $f_1 = 38.399kHz$ and $f_2 = 170kHz$. They have been selected since frequency results, at those values, underlined a device which works in either versions, but the amplification effect and accuracy of reproduction of the phenomena is different, being better at f_2. The input, in this case, will be given as a sine burst, like the one pictured in figure 5.35, centred at f_1 and f_2. Before describing results, a description of the used beam is given. As anticipated, a resonator has been built with the precise purpose of putting it at resonance with the frequency of the input. Figure 5.44 reports the CAD representation of such beam in the case where we test the geometry at f_2. The base is composed of a 3x3x3mm cube, while the beam itself is designed as a 7.75x3x1.5mm block placed on top. On the right of the aforementioned figure, it can be seen the activation of the flexural mode at the testing frequency of $f_2 = 170kHz$. A beam with the same geometry, but with different measures, has been created and used for the f_1 case, such that its resonance is f_1. Let's start the overview of results from the f_1 case. First, let's quantify if the lens brings some advantages over the usage of the resonator only.

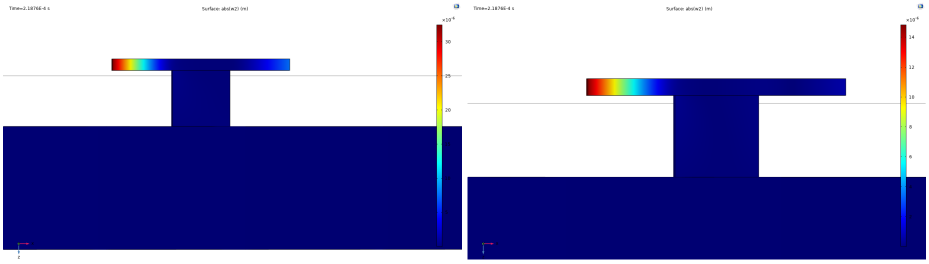

Figure 5.45: Surface plot of the beam showing the absolute value of displacement, along the z direction, taken at time frame $t = 2.18 \times 10^{-4}$ when testing at f_1 for two cases. Left: the lens is present in the domain. Right: the lens is absent.

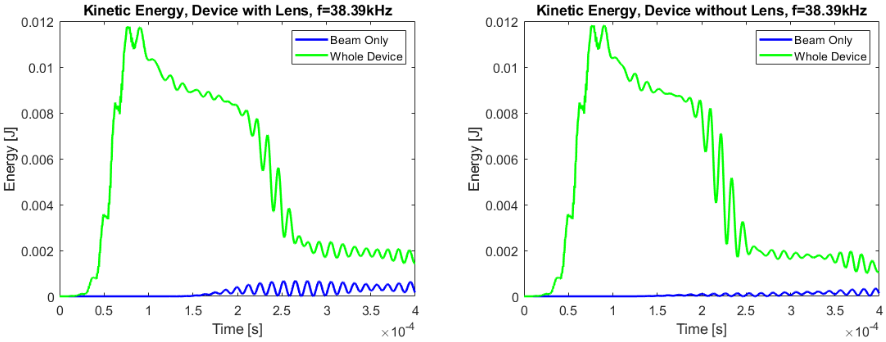

Figure 5.46: Graphs which report the kinetic energy variation across two different volumes: the whole device and the beam only. Left: device with lens. Right: Device with no lens.

Figure 5.45 proposes a comparison between surface plots of absolute value of displacement, along the z direction, taken at a time step for both the case where the lens is present in the domain and when is absent. When the lens is present, the maximum displacement on the beam reaches a value of $33\mu m$ while, if there is no lens present, the value goes down to $14\mu m$. This allows to identify an amplification factor, given by the lens, of 2.35x. Frequency analysis had underlined a slightly better magnification effect, which reached 3x but, still, the effect is present even here. Having described the performances in terms of displacement amplification, the next aim is to verify if energy is correctly localised on the beam. To do that, the goal now is to verify how kinetic energy varies in time in two different volumes: on the beam only and on the whole geometry. Results are reported in figure 5.46 for both the case where the lens is present and when the lens is absent. To obtain these graphs, the kinetic energy density value has been integrated, over all time steps taken, on both the described volumes. It is clear, from the comparison of the two graphs, that the presence of the lens allows to localise the energy of the impinging wave. In fact, the blue graph on the left allows to appreciate a greater localization effect than the case where the lens is absent. The localization effect, although is present, is not that great.

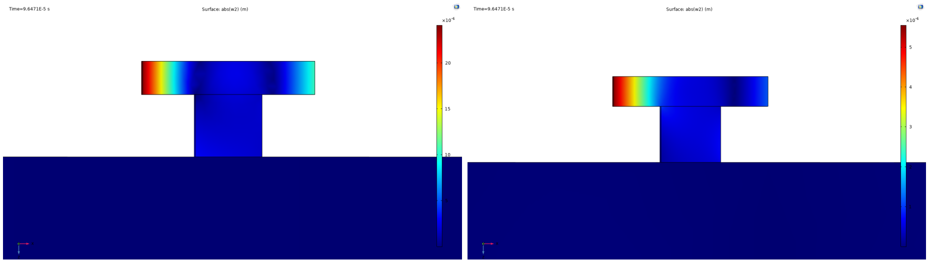

Figure 5.47: Surface plot of the beam showing the absolute value of displacement, along the z direction, taken at time frame $t = 9.64 \times 10^{-5}$ when testing at f_2 for two cases. Left: the lens is present in the domain. Right: the lens is absent.

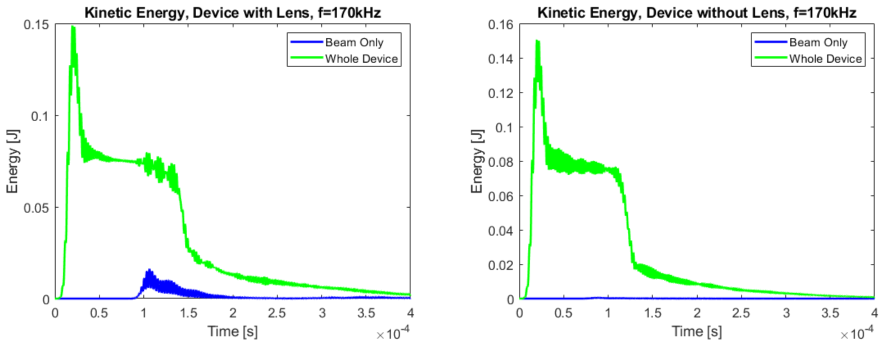

Figure 5.48: Graphs which report the kinetic energy variation across two different volumes: the whole device and the beam only. Left: device with lens. Right: Device with no lens.

Especially, considering the instant $t = 2.2 \times 10^{-4}$, we have that the energy on the beam is 0.5mJ, while on the whole domain is 7.75mJ. This leaves us with a concentration effect of 7.67%, a bit low. Having registered such results, the test is repeated for f_2. Figure 5.47 reports surface plots of the absolute value of displacement comparing the amplification of a design where the lens is present against one where the lens is absent. On the left of the image it can be seen the results of the test with the usage of the lens and the beam altogether. Even here, when the lens and the beam are tested altogether, the amplitude of displacement goes up, as one could expect, since the beam is vibrating at resonance. In particular, as the image suggests, the amplitude of displacement reaches $25\mu m$, which is a very promising result. On the other hand, if the lens is not present, the maximum magnitude of displacement is around $5.5\mu m$, which means that the gain given by the lens is roughly 4.54x. This is a good result, as it tells us that the lens is working better than in the previous example, and is even in line with frequency domain analysis, where simulations reported, for this frequency and the A_0 mode, an amplification factor of 4.5x. The other result which is interesting to comment is the one regarding energy variations inside the structure. To check if energy is localised on the beam and not dispersed, we check again how the kinetic energy varies in the domain. In particular, a volume integration of the kinetic energy density is performed over all time steps calculated for two different volumes: only the beam and on the whole device. Figure 5.48 shows the results of this integration. From the comparison of the two graphs is clear, even in this case, that the presence of the lens allows to localise, on the beam, a greater portion of energy than it would be localised if no lens was present, which is a strong point over the usage of lens structures in EH. Furthermore, here the efficiency is even better than in the previous case. In fact, taking a time instant of $t = 1.2 \times 10^{-4}$, if the whole device registers a kinetic energy of 80mJ, the beam registers 16mJ. This can be translated into a 20% energy localisation. This result is much better than the previous found but, again, this was expected since, as frequency analysis have shown, frequency f_2 has an overall behaviour which allows a greater magnification effect and a greater localisation of displacement, which are responsible for the better performances in energy localisation.

Chapter 6

Luneburg lens prototype 2

This chapter is dedicated to the overview and analysis of the second Luneburg lens design reviewed in this work. First, section 6.1 deals with the theoretical description of this new construction method employed here, highlighting all the major differences found between this procedure and the one described in chapter 5. Subsequently, a detailed report on all numerical simulations, which have been performed via the usage of COMSOL Multiphysics simulation software, is reported. In particular, section 6.2 deals with all the frequency domain simulations which aim at reproducing the correct behaviour of the lens. A discussion on the mesh's convergence will also be reported. Then, section 6.3 reports the results of time domain simulations, with a particular focus on the ones which will be needed for making EH considerations.

6.1 Construction of the Lens

The last category of device that is going to be tested is another Luneburg lens. In this case, as it has been anticipated, the theoretical derivation which leads to the final refractive index distribution is different from the one seen in Chapter 5. The lens, aimed at focusing only flexural A_0 waves, is built here via the usage of guidelines reported on the work first presented by Tol S. et al, 2017[22]. The main discrepancy found between this method and the one previously analysed lies in the definition and calculation of the refractive index. If, previously, the refractive index was calculated via the usage of the plate velocity term, now the referring term is the wave velocity value taken directly from dispersion relations, which creates some differences between the two methods, as it will be explained in a moment. Even in this case, as is has been pointed out in the previous section, due to the peculiar omni-directionality that characterizes this type of lens, the authors employed a unit cell which possesses hexagonal symmetry. The unit cell used for the calculation of dispersion relations is shown in figure 6.1, alongside the representation of its Brillouin zone. The inclusion, in this geometry, is represented by a hollow cylinder which is not completely drilled, leaving a blind hole. The authors justified this choice citing better preservation of the plate's structural integrity, in spite of the corresponding situation with a through hole. The cell has the following dimensions: unit cell size $a = 8mm$, height of the blind hole $h_b = 2.175mm$, total height $h_{tot} =$

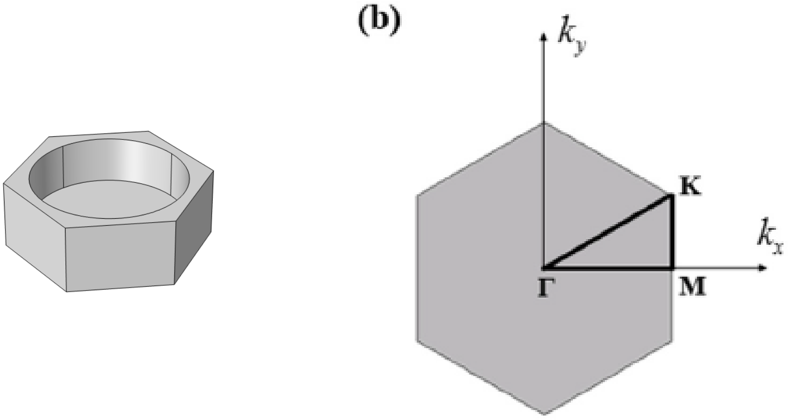

Figure 6.1: Tol S. et al, 2017[22]: Left: Unit cell employed in their work and used for the construction of the second Luneburg prototype. Right: Correspondent brillouin zone for such cell.

3.175mm and a variable diameter of the inclusion. Next, the goal is to tune correctly the refractive index. As anticipated, the most important difference from the previous methods lies exactly in how it has been defined. This time, the refractive index is still calculated by means of a ratio between velocities but, now, the procedure to get those values is different. The refractive index can be written as

$$n_{A_0} = \frac{v}{v_{\Gamma M}} \tag{6.1}$$

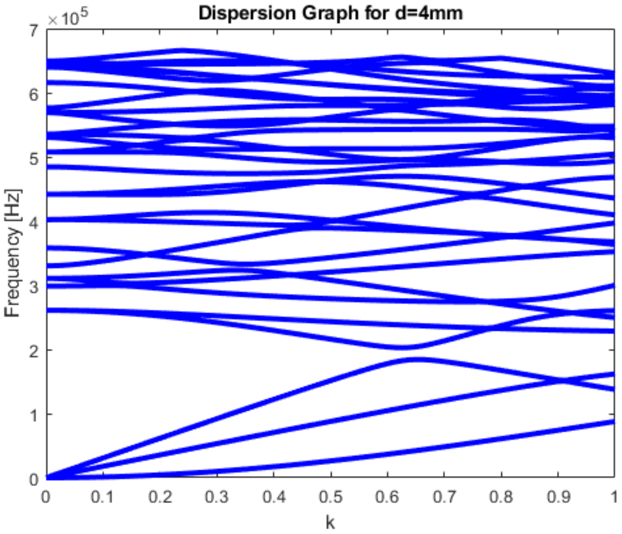

Figure 6.2: Calculated band structure for the hexagonal unit cell at a fixed diameter of 4mm.

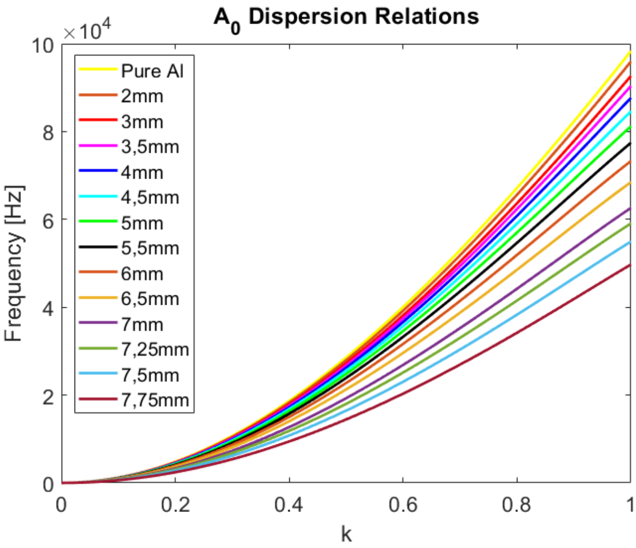

Figure 6.3: Calculated dispersion relations for the A_0 flexural waves in the hexagonal blind holes unit cell as the diameter gradually changes.

where $v_{\Gamma M}$ is the flexural wave phase velocity inside the cell with a varying diameter and v is the phase velocity of flexural waves in a pure bulk material plate. By calculating the band structures for a different set of diameters via numerical simulation software, the speed of the wave at a given frequency can be discovered. Then, the refractive index is readily available and can be compared to the ideal profile, to build the radius' inclusions distribution. To do that, we first have to select a frequency for the functioning of this device. Selecting it to be 50kHz, the derivation of the refractive index can start. Figure 6.2 shows the graphical representation of the band structure for the unit cell depicted in figure 6.1, calculated via simulation software, obtained by making an eigenfrequency analysis and sweeping the wavevector from Γ to M. After having performed this passage for different sets of diameters, the A_0 dispersion relation can be extrapolated by each of this graphs and plotted cumulatively in another one. Figure 6.3 shows the calculated dispersion relation of the flexural A_0 mode for the unit cell at various diameters, ranging from 2mm to 7.75mm. If we know the wavenumber at which the dispersion relation crosses 50kHz, then we can calculate the phase velocity of the wave by using

$$\lambda f = v \tag{6.2}$$

Once the velocity of the A_0 wave inside a given cell is found, then the refractive index is calculated. The next passage is to tune the refractive index inside the device, calculated with the aforementioned derivation, by matching it to an ideal profile. The most common ideal profile used for Luneburg lenses, as explained in more detail in Chapter 2, is the following:

$$n(r) = \sqrt{2 - \left(\frac{r}{R}\right)^2} \tag{6.3}$$

In figure 6.4 this ideal refractive index profile for a Luneburg lens is reported,

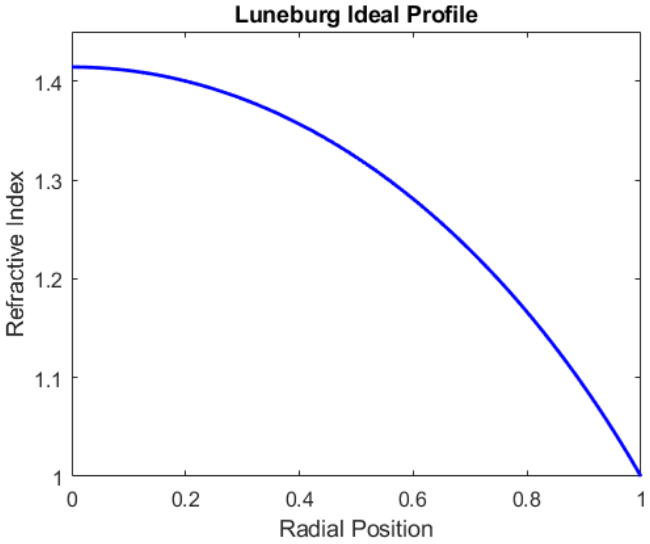

Figure 6.4: Ideal refractive index profile, calculated via the usage of the above given formula, plotted against the radial position inside the lens.

where the different values of refractive index profile are plotted against the radial position where such index has to be set. To do such task, the authors already provided, in their work, the graph that allows to pass from the value of radial position to the value of the cell's diameter. In figure 6.5 on the left such graph is visible. On the right, a representation of the final lens via usage of CAD software is displayed. Diameters value range from a maximum of 7.75mm in the central region, where the wave speed needs to be the lowest, to a value of 2mm at the lens' edge. This is how this lens has been built. The main consequence

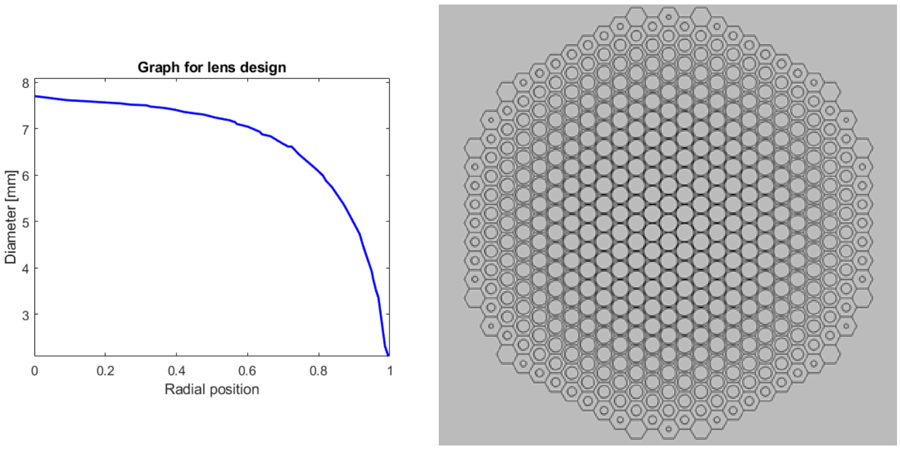

Figure 6.5: Left: Plot of the inclusion's diameter needed at a given radial position to achieve focusing inside the lens. Right: Final lens design obtained via CAD software.

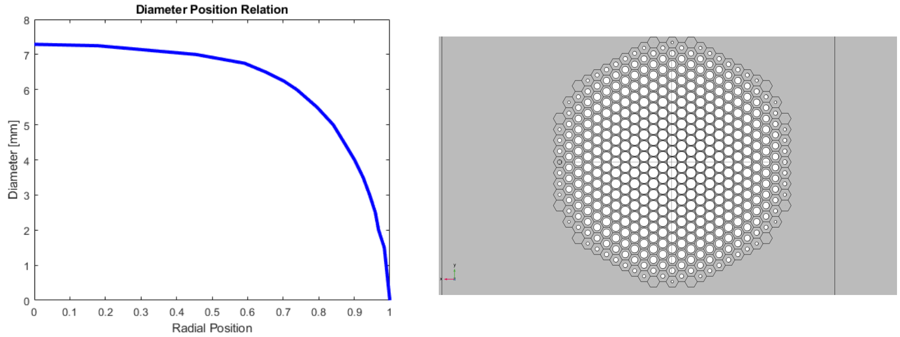

Figure 6.6: Left: Graph that correlates the diameter of the inclusion in the through hole case to the radial position of the cell inside the lens. Right: CAD representation of the through holes design.

of this approach is that this lens prototype, compared to other two described in the previous chapters, where the usage of the effective medium theory allows to increase the frequency-functioning span, does non show this property. This is to be attributed precisely to the different definition of the refractive index. Here, such index is defined thanks to the speed of the wave taken from dispersion curves, so is a frequency dependent value, hence the limited frequency validity of the theory. Previously, the definition of $n(r)$ from the plate thickness and plate velocity allowed to increase the frequency working window of the lens since the cited values depended from the inclusion's diameter but not from the functioning frequency. In order to test more accurately this second design, which does not involve an effective medium theory, another lens has been built for further testing. In this case, it has been supposed that the holes are further drilled such that this second lens is based on unit cells with fully drilled holes. Of course, since now the holes are through, supposing the same working frequency of 50kHz, for a given value of diameter the dispersion relation for the A_0 mode in the through case will be lower that the one in the blind case. So, the graph that allows to know which is the correct diameter value for each value of the device's radial position, reported here in figure 6.5, has to be rebuilt. In figure 6.6 such graph is reported on the left, while the representation of the final lens depicted with CAD software is reported on the right. In this case, diameters range from 7.3mm to 0 on the lens' edge. The material used in this case will be aluminium, with material properties reported in table 6.1. Having explained how each lens has been built, the following step is to describe the analysis performed and to comment on them. The next section is dedicated to the overview of the focusing capabilities for each lens, underlining which is the lens that allows to get the most amplification with respect to a no lens case. A brief discussion on the frequency ranges in which these devices work correctly is also brought up. For simplicity, the two devices will be referred to as "blind hole device" and

Table 6.1: Material Properties used for these simulations

MATERIAL	E [GPa]	ν	$\rho[Kg/m^3]$
Al	70	0.35	2710

"through hole device", to distinguish them more easily.

6.2 Frequency Domain Analysis

Having explained how the lenses are going to be built in the previous section, here the description of some analysis will be carried out. In particular the first focus will be put on analysis in the frequency domain. First, the functioning of each device will be inspected, to demonstrate the power of this second design. Then, a brief analysis is dedicated to demonstrating that this device does not show any broadband functioning, as it has already been recalled. Before, let's discuss the geometry and the boundary conditions. For the setting of the analysis, the guidelines given by the authors of this second method were followed, to ensure the maximum reproducibility of the results reported in that paper[22]. First, the domain is set to be an aluminium plate of dimensions 760x305mm. The domain, compared to the lens, which has a radius of 88mm, is much bigger. This choice has been justified to ensure that reflection of waves at boundaries does not interfere with our problem. Going in the same direction, the application of absorbing boundary conditions along the plate's external thickness has been imposed, to ensure that waves do not reflect back in the domain when they hit the external walls of the plate. Then, depending on the type of analysis performed, a different type of loading condition will be set. The authors of the text from which the design is taken used time domain simulations to evaluate the lens' performances and exploited a sine burst load that changes in time. Before moving to the time domain here, in frequency domain analysis, the type of load will be the same used in the previous frequency analysis, which consists in a prescribed displacement in z direction at a frequency of $f = 50kHz$, since now only A_0 waves trigger the focusing effect and are tested. The first trial reported here will be the one dedicated to the blind hole device, where the focusing capabilities of the device are tested. Before going through the results, a bit of discussion is dedicated to the mesh, visible here in figure 6.7. The mesh has been built by using the following rule: for being at convergence when dealing with wave phenomena, you need to have at least 6 or 7 finite elements per unit wavelength, such that the result is correctly reproduced. In our case, wave propagation is along x, but displacements are along z, so the number of elements in z has to be checked. For the selected frequency f=50kHz, the wavelength inside the pure Al plate is

$$\lambda = \frac{v}{f} = 2.3cm \tag{6.4}$$

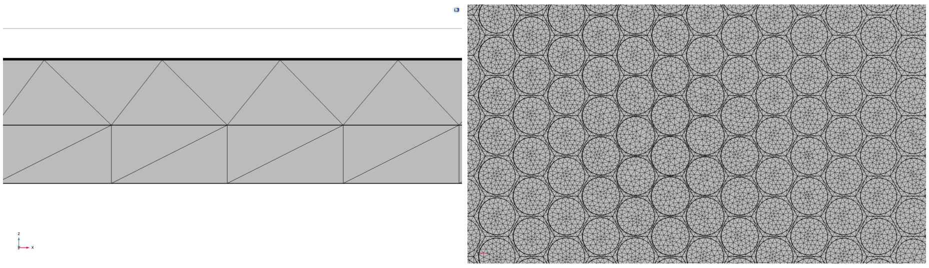

Figure 6.7: Graphical representation of the mesh used for the blind hole device.

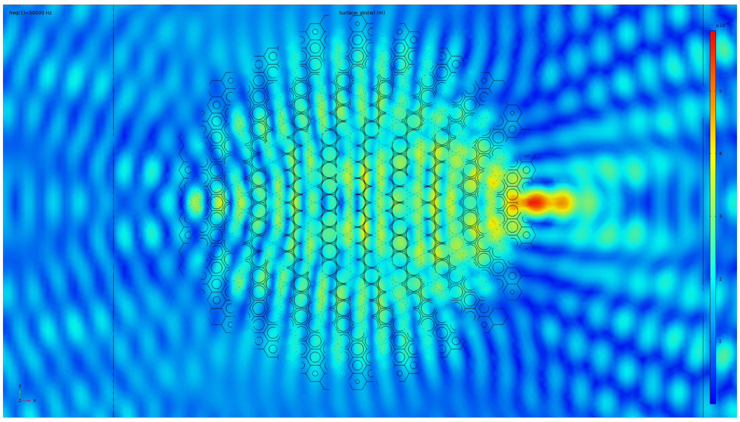

Figure 6.8: Surface plot displaying the absolute value of displacement, along the z direction, for the blind hole device tested at f=50kHz.

Where v is the velocity and f the frequency of the wave.The overall thickness of the device is 3.175mm, and in that space 2 elements are placed, clearly visible in the left image of figure 6.7. This means that, in our case, the minimum requirement holds. Results evaluated with this mesh are reported in image 6.8.

Here it can be seen that the blind hole device works great and as expected. Planar A_0 wavefronts are focused at the opposite point with respect to the entrance one, as it can be clearly noted. To make more quantitative assessments, the conventional line plot which passes across the focusing point is proposed in image 6.9, where the absolute value of displacement along the y=0 line is

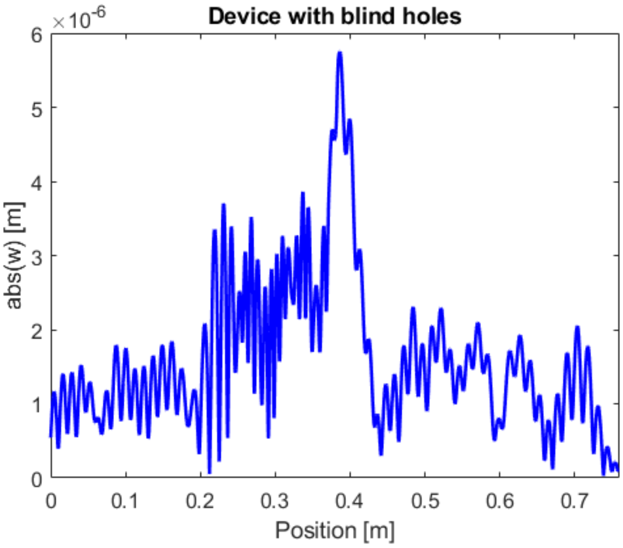

Figure 6.9: Line plot showing the absolute value of displacement, along the z direction and plotted at the y=0 line, for the blind hole device tested at f=50kHz.

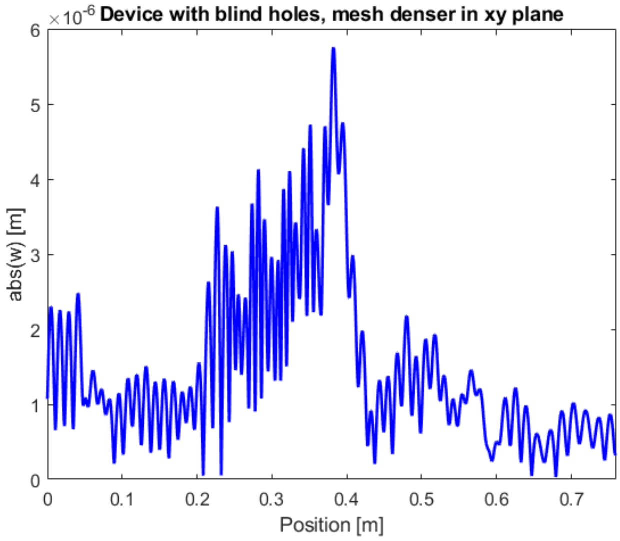

Figure 6.10: Line plot, created along the y=0 line, of the absolute value of displacement obtained with the use of a mesh more refined in the xy plane.

reported. In this case, the effectiveness of the device can be clearly noticed by looking at the sharp and localised peak present at the end of this lens. Even the displacement concentration effect found here is very great, since a 5.75x magnification, with respect to the maximum amplitude of displacement of the initial input, is registered. The following efforts will be dedicated to the demonstration that this simulation has indeed reached convergence, with some comparison between different meshes. As it has been declared, the mesh that has been used up to this point has got two elements along the thickness of the device and a "finer" element size, defined in COMSOL, along the xy plane. Here it will be proposed the comparison with two other meshes, one more refined in z, the other more refined in the xy plane, to see if the increased number of elements in either directions alters the results considerably or not. The first comparison deals with analysing the behaviour when we make the mesh denser along the xy plane. In this case, the new mesh contains only 1 element along the thickness of the device, while the size of elements on the plane has been set, inside the simulation software, as "extra fine". For this new mesh the line plot, at y=0, of the absolute value of displacement along the z direction, is proposed in figure 6.10. We can still notice that the behaviour is correctly reproduced and, so, that even 1 element along the thickness allows the phenomena to be grasped by the numerical simulation. This was expected though, as we still are inside the 6-7 finite elements per unit wavelength limit. To make a closer comparison, image 6.11 proposes the comparison between this mesh, denser on the xy plane, and the one used previously in the test of the device. It can be clearly seen that both meshes allow the simulation to work as expected, with some minor differences. The mesh with 1 element along the thickness shows a more gradual increment of the displacement when approaching the maximum point of amplification, which is a more elegant representation of the functioning of the device. The other, with 2 elements along the thickness, reproduces the

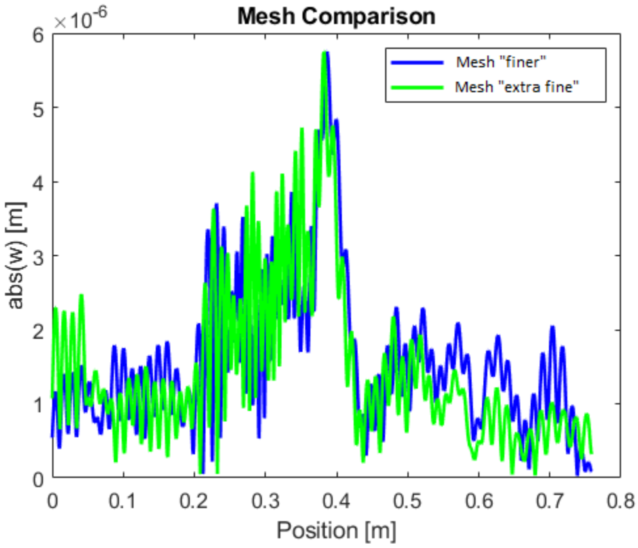

Figure 6.11: Comparison between line plots of absolute value of displacement, along the z direction and taken at y=0, obtained from two analysis performed with two different meshes, one more refined in the xy plane (green plot) and the other more refined in z (blue plot).

phenomena correctly but the increment between the middle peaks and the final one is more abrupt. The peak shifts even slightly, from x=38.25cm in the mesh with 1 element along the thickness of the device to x=38.75cm for the other, so a very small shift. For what concerns the actual amplification, the maximum amplitude is the same in both, with the focusing point that reaches

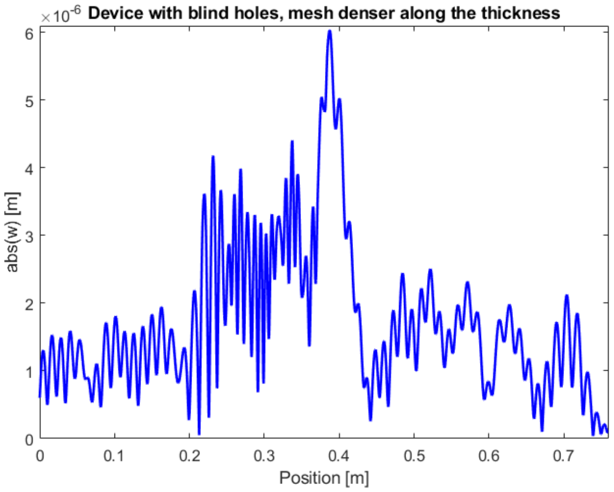

Figure 6.12: Line plot of the absolute value of displacement along the z direction, taken at the y=0 line, for the mesh with 3 elements along the thickness.

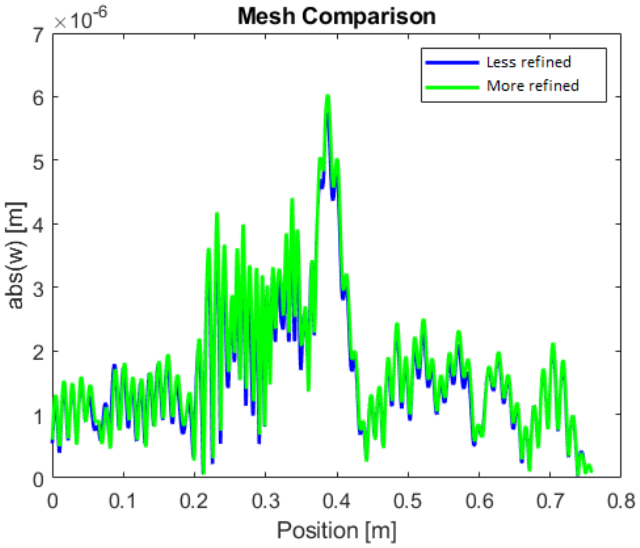

Figure 6.13: Comparison between line plots which represent the absolute value of displacement, along the z direction and taken at y=0, obtained from two analysis performed with two different meshes, one with 2 elements along the thickness and the other with 3.

a 5.75x amplification of displacement. Overall, both meshes are very good at reproducing the phenomena. Next, the test of a refinement along the thickness will be proposed, where a mesh with 3 elements along the thickness and the same density of elements along the plane as the initial mesh will be studied. The line plot of the absolute value of displacement, drawn along the y=0 line, is reported in figure 6.12. Here it can be seen that the simulation, with this mesh more refined in z, behaves almost identically to the original one with less elements along the thickness. A more detailed comparison with the initial mesh can be brought up by superimposing the line plots at figure 6.13. Here, it can be seen that the behaviour of the device under these two different meshing conditions is practically the same, justifying even more the evidence that the first mesh is, at least in z direction, at convergence. The only minimal difference is on the amplitude of displacement, where this new mesh more refined in z registers a 6x amplification, compared to the 5.8x of the previous one. Again, even if a small increment is found, it is not considered too wide to justify the usage of this new mesh over the other. Concluding, it has been demonstrated that the correct behaviour of this device is picked up by all of these meshes, which propose overall close results. It is expected that the most precise behaviour on the simulation will be reached with two elements along the thickness and an "extra fine" element size along the xy plane. Sadly, this mesh does not run on our computer, since more RAM would be needed. A choice, then, has to be made for the following simulations on which mesh to use, where the starting mesh will be employed, as it demonstrated to be overall well balanced. Next, the final analysis for this device involves the demonstration that is not capable of broadband functionality. In particular, a frequency sweep has been done for frequencies between 49kHz and 51kHz, with a step of 100Hz, reported in figure

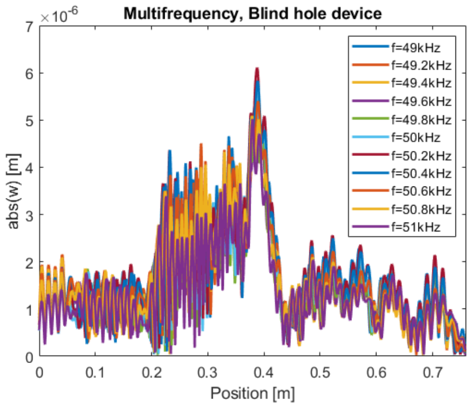

Figure 6.14: Superposition of various line plots of the absolute value of displacement, along the z direction and taken at the y=0 line, for the blind hole device at different frequencies, ranging from 49 kHz to 51 kHz.

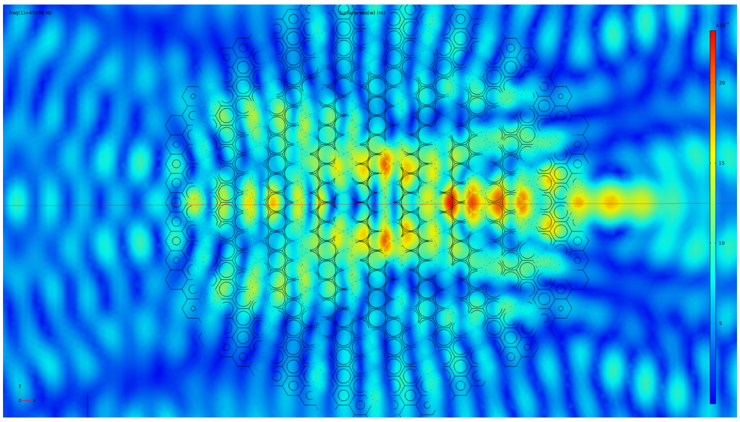

Figure 6.15: Surface plot showing the absolute value of displacement, along the z direction, in the lens' region. The device tested is the blind hole design at a frequency of f=45kHz.

6.14. As it can be noticed from the analysis, the device still works, but the middle peaks are starting to arise, showing a progressive worsening in the trend of the analysis. If a frequency even lower is taken, for example 45kHz, reported in figure 6.15, it can be seen that the focusing behaviour of the lens vanishes completely. This is particularly evident by checking that the maximum red dot has moved form the lens' edge, where it belongs theoretically. Looking at the usual line plot reported in figure 6.16, which reports the absolute value of displacement along the y=0 line, the differences are straightforwardly grasped. Not only the final peak decreases in intensity, bet even the other middle one increase, owing to a more flat behaviour of the lens, where focusing capabilities have been lost. This result is in agreement with what has been stated before on the working principle of this lens. It can be added that the device can work at frequencies near the design one but, as it has been demonstrated, going

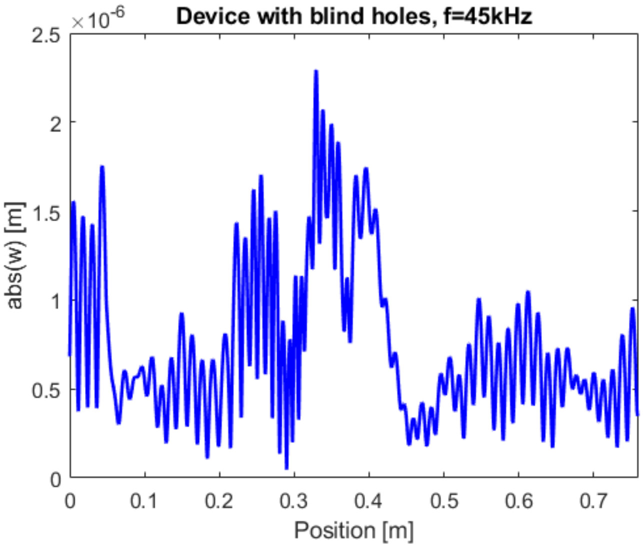

Figure 6.16: Line plot, graphed at y=0, of the absolute value of displacement, along z, in the blind hole case at a frequency of f=45kHz.

further from those compromises the functioning severely. Having concluded the analysis on the blind hole design, the next step is to review the through hole design to make a closer comparison between the two. Of course, as it has been anticipated, the settings of the analysis have not changed: we barely changed the geometry, but boundary and loading conditions remain the same. So, along the thickness of the device absorbing boundary conditions are imposed, while the loading condition is still a sinusoidal displacement at frequency 50kHz with maximum amplitude $1\mu m$. This time, the use of through holes allows to further refine the available mesh on the xy plane. In particular, the mesh used has been built by creating a free triangular mesh on one surface with an element

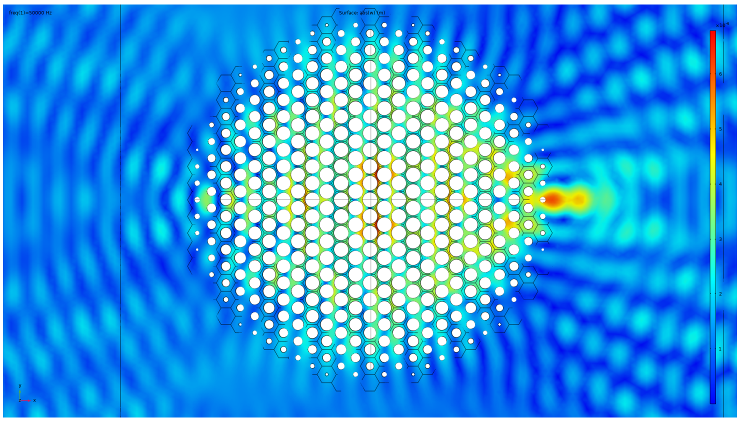

Figure 6.17: Surface plot of the absolute value of displacement, along the z direction, of the through hole device tested at the design frequency of f=50kHz.

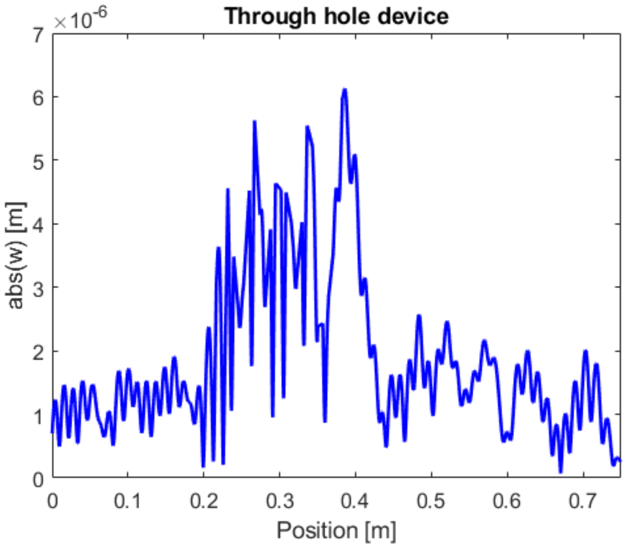

Figure 6.18: Line plot, taken at y=0, of the absolute value of displacement, along z, for the through hole device working at the design frequency of f=50kHz.

size of "extra fine", which was then used to create a free tetrahedral mesh. In figure 6.17 results for the analysis at 50kHz are reported. Although the picture reported here seems nice, as the focusing point can clearly be seen in the image and registers a 5.5x amplification, there are some problems with the through

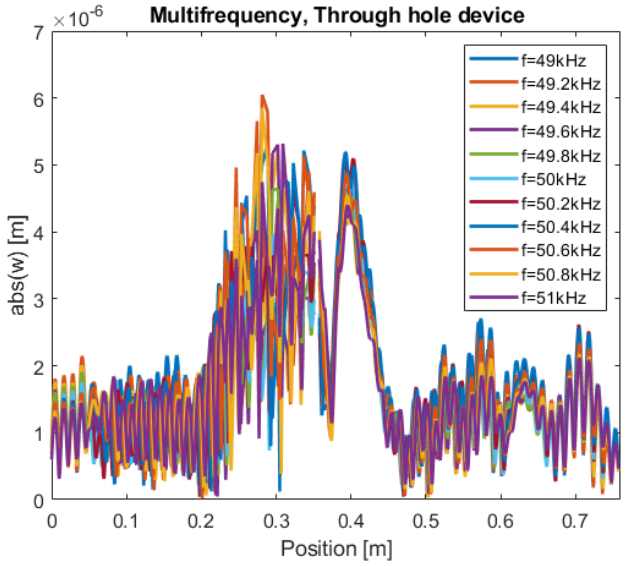

Figure 6.19: Cumulative representation of the line plot, at y=0, of the absolute value of displacement, along the z direction, for the through hole design at frequencies ranging from 49kHz to 51kHz.

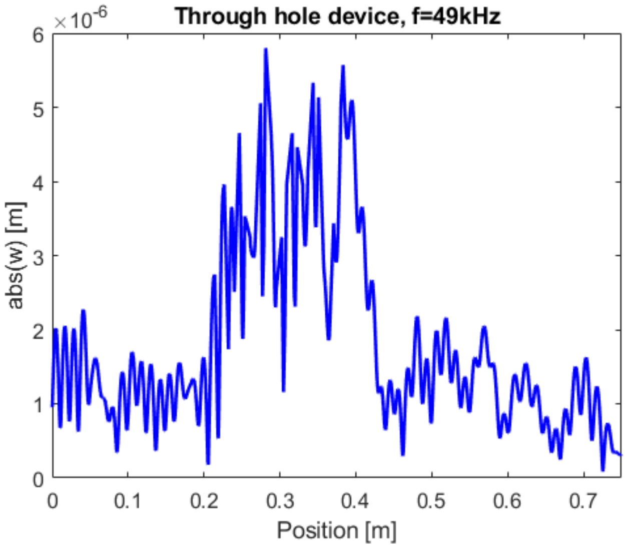

Figure 6.20: Line plot of the absolute value of displacement, taken at y=0, for the through hole case working at a frequency of f=49kHz.

hole design. First, even if in the image cannot be clearly seen, there are some red spots inside the lens, which means that amplification occurs even inside the device, and this is unusual, to say the least. Not only that, but actually the absolute maximum is not achieved at the lens' border, but in the middle. This are all signals that, even if an amplification at the end is present, the device doesn't work completely as intended. To support more this deduction, the graph along y=0 of the absolute value of displacement is reported in figure 6.18. Here it can be clearly seen that, while the device shows focusing at the lens' edge, something is wrong with the behaviour inside the lens. In particular, peaks in the middle of the device start to arise and have an almost comparable height to the maximum at the lens' end. So, even if focusing is indeed present, the device's behaviour is showing deviations from its ideal one, which is not a great sign. This becomes more evident if, like it has been done for the blind hole design, a sweep between 49kHz and 51kHz is performed. Cumulative results, where the plot of the absolute value of displacement along the y=0 line are reported for all frequencies, are shown in figure 6.19. In this case, gong away from the design frequency alters more substantially the behaviour of the device. The last peak remains the absolute maximum only for a handful frequencies very near 50kHz. Already going to 49kHz, for example, as figure 6.20 shows, alters the behaviour badly. In fact, for this frequency, the middle region of the lens registers higher amplifications than the edge region. Concluding, it has been demonstrated that, while the blind hole device behaves as expected, the through hole one still shows focusing, but with overall less precision in the reproduction of the phenomena. Both devices are not set to work at wide frequency range, being able to work only at their design frequency or for frequency not that far.

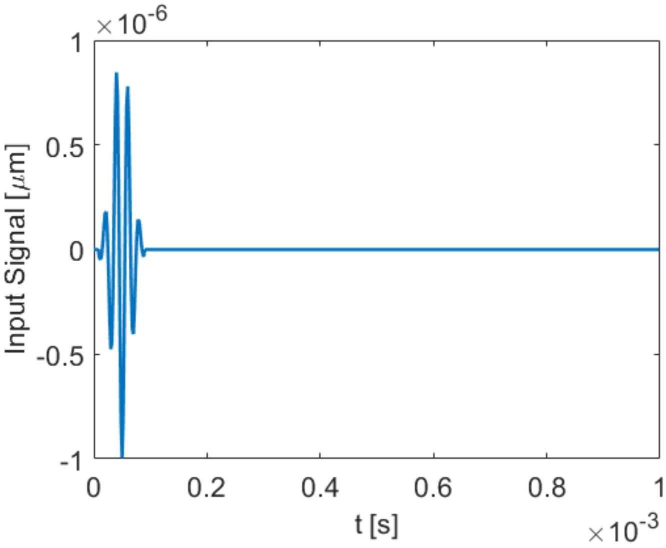

Figure 6.21: Graphical representation of the sine burst input calculated with MATLAB.

6.3 Time Domain Analysis

In this section, time domain analysis made on both devices will be reviewed. In our case, these analysis have been performed for two main reasons. First, using time domain simulations allows to see better the focalization effect localized at a precise given time frame. So, the simulated behaviour is much closer to what can be expected to occur in real life. Second, these analyses will be fundamental in the subsequent discussion on the possibility of using this design for energy harvesting purposes, since they will allow us to make considerations on the energy of the system. Both devices will be tested in time domain simulations, trying to see if what has been found in the frequency domain matches this new results. The simulations have been set in the same way as the other ones, which means that the same plate with absorbing boundary conditions along the thickness is going to be tested. Even the same meshes used in frequency domain simulations are employed. This time, though, what changes is the input. Following the guidelines given by the authors in their research[22], a sine burst input has been given, composed of 4 cycles at amplitude $1\mu m$ centred at 50kHz. A representation of this input is given in image 6.21. The main difference is, of course, that this input is no more constant in time, as the previous ones were. This particular input, though, should allow to see the working principle of the lens very clearly by representation of waves bending in the medium and reaching the focusing point at different speeds. As it has been done before, we start from the blind hole device. The simulation hs been run between zero and $t = 4.6 \times 10^{-4} s$, which should allow to see the phenomena. The time step has been selected such that it respects the Courant-Friedrichs-Lewy condition, represented by

$$C = \frac{v\Delta t}{\Delta x} < Cmax = 0.2 \tag{6.5}$$

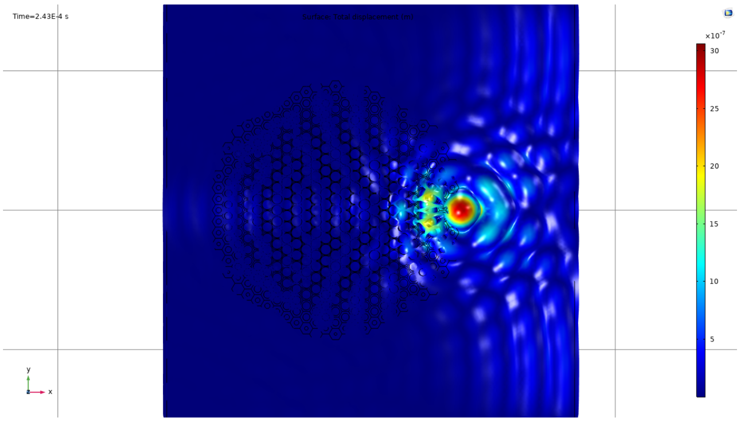

Figure 6.22: Surface plot of the absolute value of displacement, along the z direction, for the blind hole device taken at time $t = 2.43 \times 10^{-4}$

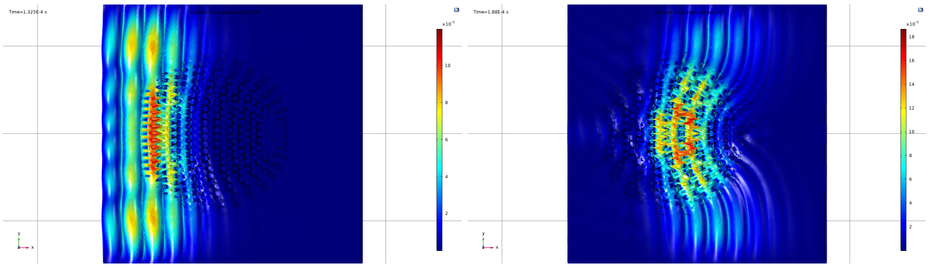

Figure 6.23: Surface plots of the absolute value of displacement, along the z direction, for the blind hole device taken at different time windows, to help visualise the focusing effect in time. Left: $t = 1.325 \times 10^{-4}$. Right: $t = 1.88 \times 10^{-4}$

where v is the wave's speed, Δx the spacial interval and Δt the temporal one. This is done to ensure that time convergence is met. Setting Δx as the mesh dimension, we get that $\Delta t \leq 3 \times 10^{-7} s$. For what concerns the mesh, the one with 2 elements along the thickness and a "finer element density along the plane" has been used, like in the previous section. Having cleared that, let's start by looking at the results. Figure 6.22 shows the instant at which focusing happens. The image clearly tells us that the device is working, as the displacement is well concentrated in the point diametrically opposed to the entrance one. The maximum displacement at the focusing point is registered as $3.3 \mu m$. Considering that this input, built using MATLAB, has a maximum amplitude of $1 \mu m$, the magnification effect is 3.3x. This is a little bit less than what has been found in frequency analysis. It is to be noticed, though, that the input there was constant and not a sine burst, so the increased magnitude there is probably due to the different input. To help visualize better the functioning of this device, figure 6.23 reports two surface plots, of the absolute value of displacement, at two different time instants, before wave localization occurs.
As it can be clearly seen, planar wavefronts enter the device, they travel inside a medium with different speed, due to the locally tailored refractive index,

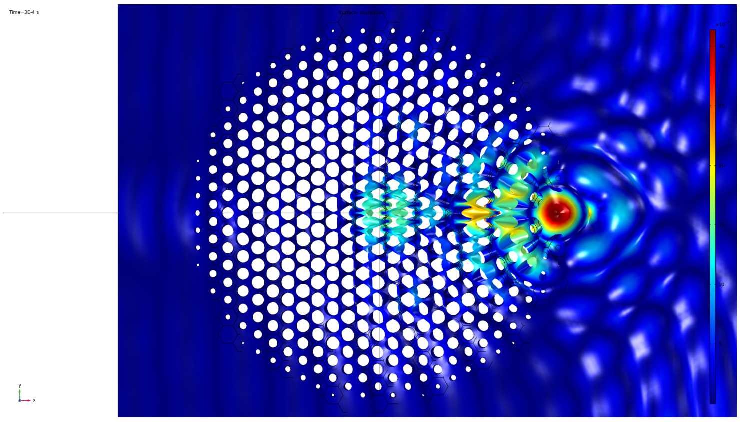

Figure 6.24: Surface plot of the absolute value of displacement, along the z direction, for the through hole device taken at time $t = 2.4 \times 10^{-4}$

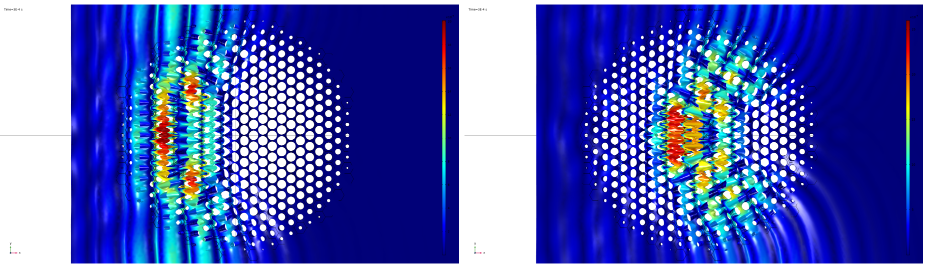

Figure 6.25: Surface plots of the absolute value of displacement, along the z direction, for the through hole device taken at different time windows, to help visualise the focusing effect in time. Left: $t = 1.5 \times 10^{-4}$. Right: $t = 1.87 \times 10^{-4}$

to then converge into the focusing spot, which is represented by the instant shown in figure 6.22. The next analysis will be dedicated to the through hole device. The same sine burst load will be used as input. Figure 6.24 reports the instant at which focusing occurs even in this lens. In this case, the amplitude of displacement predicted at the focusing point is very similar to the blind hole case, so the magnification effect of the input is comparable. Figure 6.25 reports the behaviour of the device at two different instants, highlighting the deviation effect caused by the refractive index tuning even for through holes. The main difference, highlighted in the section dedicated to frequency analysis, is that this through hole design causes to have high magnitudes of displacements inside the lens, which come much closer to the maximum value reached at the lens' edge. This can be even appreciated by comparing the plots reported in figures 6.23 and 6.25. If, for the blind hole case, inside the lens the displacement rarely overcomes $15\mu m$, in the through holes the displacement slightly overcomes $20\mu m$, underlining one more time that the blind hole device shows a behaviour which is more in line with the ideal one. Having cleared that the time domain simulation and the frequency domain one converge, the following analysis for energy localization can be carried out. In particular, being interested at the behaviour for energy harvesting, the idea is to add to the domain a beam. If

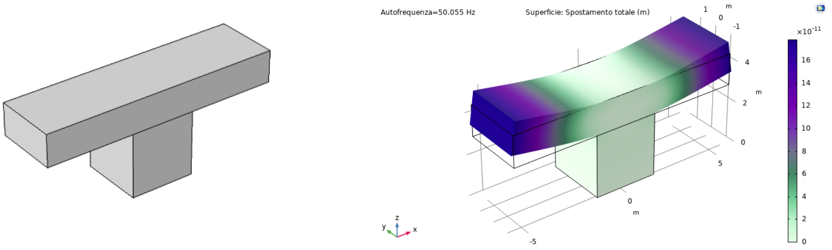

Figure 6.26: Left: CAD representation of the beam used for the time domain simulation. Right: Graphical representation of the activation of a flexural resonance at f=50.05kHz

the resonance frequency of the beam is set to match that of the input, of course the beam will vibrate in resonance and amplify even more the displacement. Our hope is first to check if the usage of both this lens and the beam is convenient in terms of amplification of displacement and, then, if such design allows to concentrate energy locally on the beam, such that a piezoelectric layer placed on top of the beam can benefit from this setup by activating the d_{31} mode. The beam used in this domain is reported in figure 6.26. The beam is 11.14mm long, 5mm wide and 2mm thick. On top there is a $2\mu m$ piezoelectric layer, while the base is a 3x3x3mm cube. This particular design has been selected since it allows to use the same material as the material of the lamina for reaching resonance at 50kHz. Otherwise, if the base was all on the left, the resonant frequency would have been too low. The right image of figure 6.26 shows the eigenfrequency analysis, which confirms that, at f=50.05kHz, a flexural vibration mode is activated. Having done so, this beam is placed inside the Luneburg lens plate at the exact position of the maximum achieved by numerical calculations.

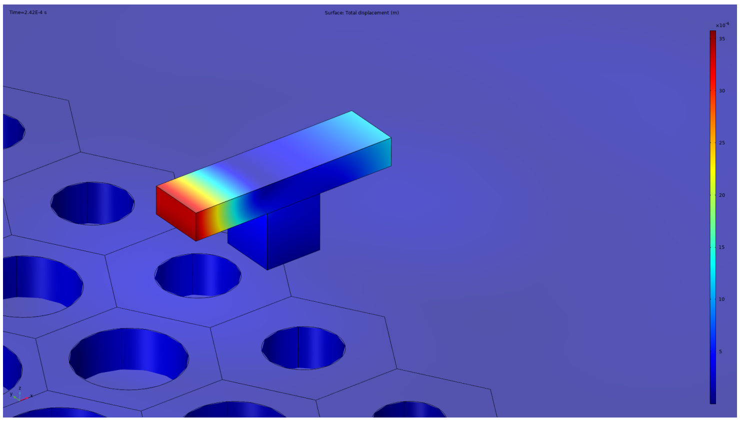

Figure 6.27: Surface plot showing the absolute value of displacement, along the z direction, for the beam tested in conjunction with the blind hole lens. The image is taken at instant $t = 2.42 \times 10^{-4}$

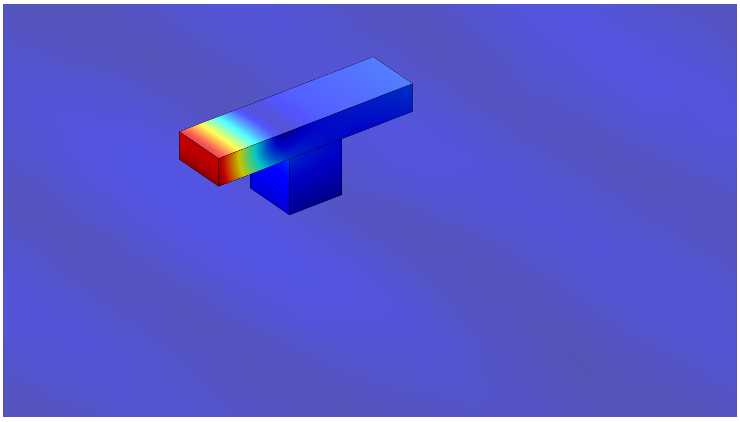

Figure 6.28: Surface plot showing the absolute value of displacement, along the z direction, for the beam tested without any lens. The image is taken at instant $t = 2.5 \times 10^{-4}$

The same sinusoidal input as the previous time analysis is given, composed by a 4-cycle sine burst centred at 50kHz and represented in image 6.21. Having said so, the review of this results starts with an overview of the blind hole device. Figure 6.27 reports the absolute value of displacement in the z direction on the beam at a time frame slightly after the time at which, in previous analysis, the focusing was achieved. It can be noticed that the displacement along the beam is not symmetric. This could be justified by the fact that the displacement is not caught and distributed symmetrically from the below lamina. The maximum amplitude reached by this configuration of the left beam's edge is $35\mu m$. Overall this does not seem a bad number but, to put it more on perspective, the same test has been repeated removing the lens from the domain, to see if effectively the usage of the lens brings up some advantages or not. The result can be seen

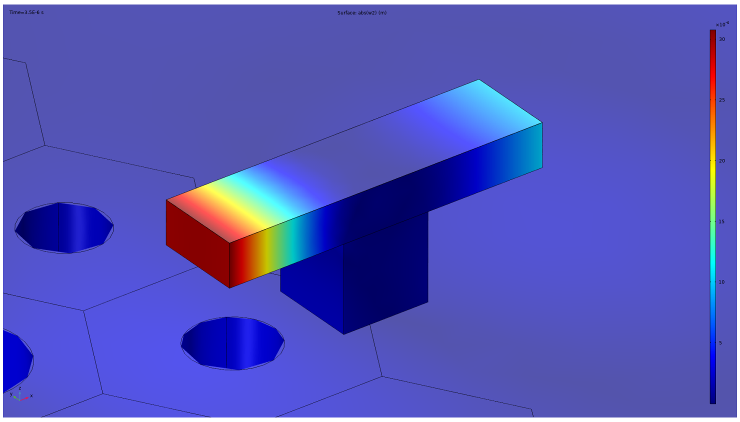

Figure 6.29: Surface plot showing the absolute value of displacement, along the z direction, for the beam tested in conjunction with the through hole lens. The image is taken at instant $t = 2.58 \times 10^{-4}$

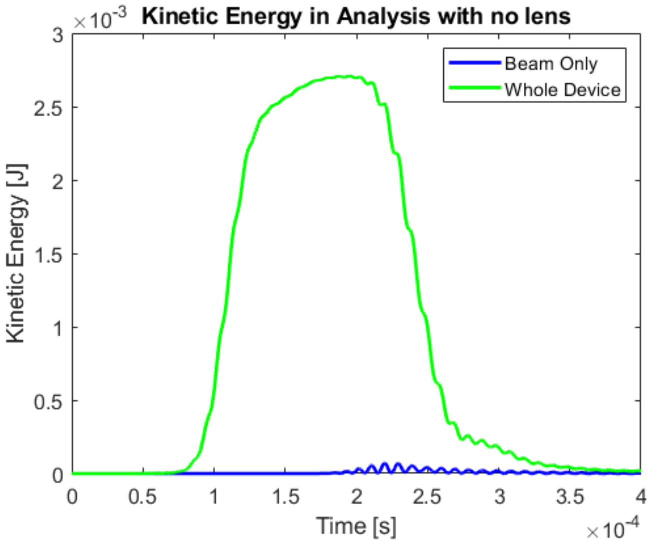

Figure 6.30: Graphical representation of the energy density value, integrated over a given volume and for every time step simulated, when the lens is not present in the domain.

in figure 6.28. Looking at the figure, we can see that the beam without the lens captures a maximum displacement of $9\mu m$ given the same input. The ratio, at this point, is almost 4x, which is in line with what the previous analysis in time domain revealed. However, the real great advantage of using the lens is another, as it will be shortly demonstrated, precisely energy concentration. The same conclusion can be made for the through hole design. Making the same analysis with the same sine burst, results are reported in figure 6.29. In this analysis, the maximum amplitude of displacement is a little bit lower than in the previous case at $30\mu m$, but the same conclusion can be made. In fact, the analysis of this domain without the lens is exactly the same reported in figure 6.28, so the amplification effect here is 3.5x, similar to the blind hole case. Having demonstrated that both lenses indeed have an effect in displacement magnification, which is similar in both through hole and blind hole design, the goal now is to check how the kinetic energy varies in time with the input that propagates in both cases. To be a good setup for energy harvesting, the device should show energy localization where we want to place the piezoelectric material, so the beam, to ensure that the efficiency of energy conversion goes up. To do that, we calculate, in both analyses with and without the lens, how kinetic energy varies in all the domain and how it varies locally on the beam. Let's start by analysing the results for the plate without any lens, reported in figure 6.30. These curves have been obtained by integrating the kinetic energy density, time step by time step, in a given volume. Two volumes are put in comparison: the whole domain and only the beam. In this graph, it can be pointed out that there is no energy localization in the no-lens case. In fact, the green curve, which represents the energy variation inside all the plate, is orders of magnitude above the blue curve, which represents the energy variation inside the beam. This means that, although the beam picks up the displacement of

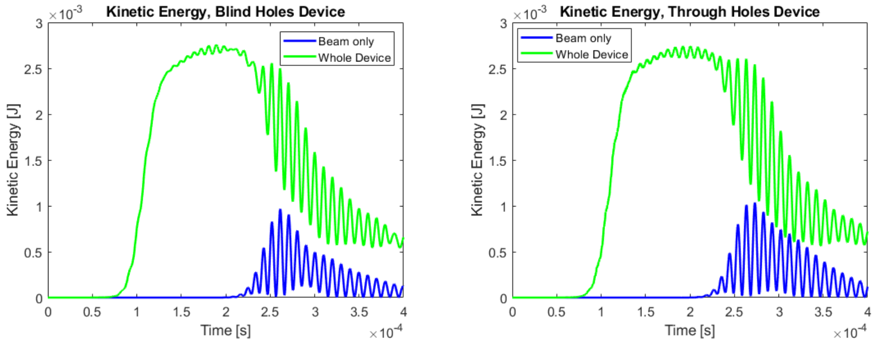

Figure 6.31: Graphical representation of the energy density value, integrated over a given volume and for every time step simulated, when the lens is present in the domain. The left image is referred to the blind hole design, the right one to the through one.

the sine burst and magnifies it, energy is more disperse all over the plate. This, fortunately, is not true for the case when either lens is coupled with the beam. Figure 6.31 reports the same kinetic energy integration operation in the case where the blind hole or the trough hole lens is added to the domain. These graphs, on the other hand, are much more promising. The green curve still represents the whole device. Comparing it to the previous one, the behaviour is similar, which is a relief since it means that the time domain simulations are in agreement. The only difference between the green curve of figure 6.30 and the ones in figure 6.31 lies in the behaviour after the wave hits the beam, which is more oscillatory in the case where a lens is present, meaning that the beam's kinetic energy constitutes a relevant fraction of the whole one, as we should expect if localization takes place. Even looking at the blue curve of figure 6.31 we can deduce the same conclusion: the kinetic energy of the beam is no more negligible: at its maximum, the kinetic energy on the beam is roughly $1mJ$ while, at that same time fraction, the kinetic energy of the whole structure is $2.5mJ$. This can be translated into a 40% energy localization, which is great for a possible prototype for EH.

Chapter 7

Conclusions

To conclude, in this thesis project different lenses designs have been tested and compared, to be able to see which one showcases the greatest potentiality for an application in energy harvesting. Three different devices have been tested: a GRIN lens and two Luneburg lenses. Each single device has been tested thoroughly with different trials. Frequency domain tests aimed at verifying the focusing properties of each lens, reviewing their accuracy and eventual broadband frequency functioning span. Time domain simulations aimed at confirming previously found informations and posed ground for evaluating the potentiality of each design for energy harvesting. After having collected informations from the analysis of all this devices, the following conclusions can be made.

Every lens tested proved to be effective from the focusing point of view, as focusing is reproducible in every situation. In particular, we have that:

- The GRIN lens device worked as expected for a broadband frequency range, although shallower than the theoretical one. The layered geometry predicts a wider range than the real geometry does.
- The first Luneburg lens prototype, built with identical guidelines as the GRIN lens, reproduces similar results to that lens, so analogous conclusions can be made.
- The second Luneburg lens prototype, on the other hand, proved to be effective only at the design frequency, or for frequencies not that far.

The main reason for this drastic change in behaviour is to be traced back to the two different theories employed in the construction of such lenses, as the refractive index derivation is different. More specifically,

- The effective medium theory of Pennec Y. et al.[26] links the refractive index in the material to the plate velocity term and to the thickness of the plate.
- The theory proposed by Tol S. et al.[22], on the other hand, exploits a refractive index calculation based on the phase velocities of waves in the phononic crystal.

This leads to the consequence that, while the effective medium theory allows to get a broadband functionality, the other developed theory does not show this property. As such, this is the greatest selling point of the GRIN lens and the first Luneburg lens. The main limitation, however, is that, although focusing is appreciable, the magnification effect provided by the lens is not always so great. In particular,

- Devices built with silicon and lead through the effective medium theory show mild displacement amplifications, averaging at 2-3x.
- Devices built with silicon and holes through the effective medium theory show greater displacement amplifications, averaging at 5x.
- Devices built with the other theory, on the other hand, show an amplification of 4.75x, more stable in both the blind hole and through hole case.

In every chapter, different configurations have been tested and picked, differentiating for focusing positions and materials employed. To make a recap, for each device the best lens was:

- GRIN lens prototype: Device made with silicon and holes
- Luneburg lens prototype 1: Device made with silicon and lead (the only one tested)
- Luneburg lens prototype 2: Blind holes device

Focusing now on energy harvesting, however, only the two Luneburg prototypes have been tested, and for a practical reason. If we suppose to test the GRIN plate with equipment for EH, the problem of where to place it arises, since through holes are present in the zone where we want to absorb energy. For Luneburg devices this problem doesn't pose, as the focusing point is at the edge of the device, so all the apparatus can be put on the background material, hence why only the two Luneburg lenses have been tested for EH. Summarizing found results, it was found that:

- The first Luneburg lens prototype, although great in focusing waves at wider ranges of frequency, was able to reach only a 20% energy concentration effect, and only at the most promising frequency of the entire range.
- The second Luneburg lens prototype managed to match, in both blind and through hole configurations, an energy localisation effect of 40%.

At this point, is pretty clear that the best design for energy harvesting is the second Luneburg lens. Not only for a question of efficiency, but even because the first Luneburg lens, tested with silicon and lead, would be much harder to build as a real prototype. Having to think at possible ways to build a prototype at the microscale with this configuration, there could be different options. Exploiting micro-fabrication technologies, ThELMA™process from STMicroelectronics[28] has already been used to build some kind of structures like the one illustrated here. The process allows to build devices with through holes in the structural layer, leaving them suspended over the base wafer, being anchored only on specifically designed parts. This works, however, for the through hole version of the device. There have been successful trials of using a modified version of ThELMA™technology for building devices with blind holes. Of course, being more complex to carry, the cost goes up and, if there aren't very compelling reasons to go for the blind hole model over the other, probably this process is not the best for building the blind hole device. Instead, another possible option would be the use of additive manufacturing technologies. Hypothetically, in this case, for both the blind hole and the through hole device, there could be the possibility of getting a prototype. However, as of today, the construction of such devices at the micro-scale is not possible with metals. Successful trials have been performed with polymers though, in particular with two-photon lithography[29]. This process allows to locally induce polymerization, thanks to the double absorption of photons on a photosensitive material, which acts as an initiator for polymerization processes. As such, the reaction is carried locally, only where the material has been chemically modified by the photon absorption, allowing to build complex 3D structures. Future developments of this argument will aim at testing energy harvesting properties more thoroughly and, if possible, at the comparison between numerical and experimental results for such presented devices.

References

[1] Pierre A. Deymier. *Acoustic Metamaterials and Phononic Crystals.* Springer, 2013.

[2] C. E. Bottani. *Lecture notes of Solid State Physics.* 2018.

[3] Abdelkrim Khelif and Ali Adibi. *Phononic Crystals: Fundamentals and applications.* Springer, 2016.

[4] Augustìn Udìas and Elisa Buforn. *Principles of Seismology.* Seconda edizione. Cambridge University Press, 2018.

[5] Su Zongqing and Ye Lin. *Identification of damage using Lamb waves: from fundamentals to applications.* Springer, 2009.

[6] Joseph L. Rose. *Ultrasonic Guided Waves in Solid Media.* Cambridge: Cambridge University Press, 2014. ISBN: 9781107048959 (hardback). DOI: `10.1017/CBO9781107273610`.

[7] Carlos Gomez-Reino, Maria Victoria Perez, and Carmen Bao. *Gradient-Index optics, Fundamentals and Applications.* Springer, 2002.

[8] R. K. Luneburg. *Mathematical Theory of Optics.* University of California Press, 1964.

[9] S. P. Morgan. "General Solution of the Luneberg Lens Problem". In: *Journal of Applied Physics* 29 (1958), pp. 1358–1368.

[10] J. D. Joannopoulos, Pierre R. Villeneuve, and Shanhui Fan. "Photonic crystals: putting a new twist on light". In: 386.6621 (1997). SP: 143, p. 149. URL: `https://doi.org/10.1038/386143a0`.

[11] S. Tol, F. L. Degertekin, and A. Erturk. "3D-printed phononic crystal lens for elastic wave focusing and energy harvesting". In: *Additive Manufacturing* 29 (Oct. 2019). ID: 306190, p. 100780. DOI: `https://doi.org/10.1016/j.addma.2019.100780`.

[12] Jaeyub Hyun, Wonjae Choi, and Miso Kim. "Gradient-index phononic crystals for highly dense flexural energy harvesting". In: *Applied Physics Letters* 115.17 (Oct. 2019). doi: 10.1063/1.5111566; 21, p. 173901. DOI: `10.1063/1.5111566`. URL: `https://doi.org/10.1063/1.5111566`.

[13] Yuping Tian et al. "Phononic crystal lens with an asymmetric scatterer". In: 52.2 (2018). SP: 025102. URL: `http://dx.doi.org/10.1088/1361-6463/aae679`.

[14] Sz-Chin Steven Lin et al. "Gradient-index phononic crystals". In: *Phys.Rev.B* 79.9 (Mar. 2009), p. 094302. DOI: `10.1103/PhysRevB.79.094302`. URL: `https://link.aps.org/doi/10.1103/PhysRevB.79.094302`.

[15] Yabin Jin et al. “Gradient Index Devices for the Full Control of Elastic Waves in Plates”. In: 6.1 (2016). SP: 24437. URL: `https://doi.org/10.1038/srep24437`.

[16] Jacopo Iannacci. “Microsystem based Energy Harvesting (EH-MEMS): Powering pervasivity of the Internet of Things (IoT) – A review with focus on mechanical vibrations”. In: *Journal of King Saud University - Science* 31.1 (Jan. 2019). ID: 278678, pp. 66–74. DOI: `https://doi.org/10.1016/j.jksus.2017.05.019`.

[17] Alberto Corigliano et al. “Mechanical Energy Harvesters”. In: Mechanics of Microsystems. https://onlinelibrary.wiley.com/doi/pdf/10.1002/9781119053828.ch9. John Wiley and Sons, Ltd, 2018. Chap. 9, pp. 161–183. ISBN: 9781119053828. DOI: `10.1002/9781119053828.ch9`. URL: `https://onlinelibrary.wiley.com/doi/abs/10.1002/9781119053828.ch9`.

[18] Hongwen Sun et al. “MEMS based energy harvesting for the Internet of Things: a survey”. In: 24.7 (2018). SP: 2853, p. 2869. URL: `https://doi.org/10.1007/s00542-018-3763-z`.

[19] Priya Shashank and Inman Daniel. *Energy Harvesting Technologies*. Springer, 2009. DOI: `10.1007/978-0-387-76464-1`.

[20] Zhu Dibin and Steve Beeby. *Energy Harvesting Systems - Principles, Modeling and Applications*. Springer, 2011.

[21] Tae-Gon Lee et al. “Enhanced energy transfer and conversion for high performance phononic crystal-assisted elastic wave energy harvesting”. In: *Nano Energy* 78 (Dec. 2020). ID: 280655, p. 105226. DOI: `https://doi.org/10.1016/j.nanoen.2020.105226`.

[22] S. Tol, F. L. Degertekin, and A. Erturk. “Phononic crystal Luneburg lens for omnidirectional elastic wave focusing and energy harvesting”. In: *Applied Physics Letters* 111.1 (July 2017). doi: 10.1063/1.4991684; 21, p. 013503. DOI: `10.1063/1.4991684`. URL: `https://doi.org/10.1063/1.4991684`.

[23] M. Carrara et al. “Metamaterial-inspired structures and concepts for elastoacoustic wave energy harvesting”. In: 22.6 (2013). SP: 065004. URL: `http://dx.doi.org/10.1088/0964-1726/22/6/065004`.

[24] S. Tol, F. L. Degertekin, and A. Erturk. “Gradient-index phononic crystal lens-based enhancement of elastic wave energy harvesting”. In: *Applied Physics Letters* 109.6 (Aug. 2016). doi: 10.1063/1.4960792; 21, p. 063902. DOI: `10.1063/1.4960792`. URL: `https://doi.org/10.1063/1.4960792`.

[25] Liuxian Zhao, Changquan Lai, and Miao Yu. “Modified structural Luneburg lens for broadband focusing and collimation”. In: *Mechanical Systems and Signal Processing* 144 (Oct. 2020). ID: 272413, p. 106868. DOI: `https://doi.org/10.1016/j.ymssp.2020.106868`.

[26] Yabin Jin et al. “Simultaneous control of the S0 and A0 Lamb modes by graded phononic crystal plates”. In: *Journal of Applied Physics* 117.24 (June 2015). doi: 10.1063/1.4923040; 27, p. 244904. DOI: `10.1063/1.4923040`. URL: `https://doi.org/10.1063/1.4923040`.

[27] Yan Pennec and Bahram Djafari-Rouhani. “Effective medium theory for elastic metamaterials in thin elastic plates”. In: 90.10 (Sept. 2014). SP: 104110. URL: `https://link.aps.org/doi/10.1103/PhysRevB.90.104110`.

[28] Alberto Corigliano et al. “Microsystems and Mechanics”. In: *Procedia IUTAM* 10 (Dec. 2014), pp. 138–160. DOI: `10.1016/j.piutam.2014.01.015`.

[29] Brian H. Cumpston et al. “Two-photon polymerization initiators for three-dimensional optical data storage and microfabrication”. In: *Nature* 398.6722 (Mar. 1999). ID: Cumpston1999, pp. 51–54. DOI: `10.1038/17989`. URL: `https://doi.org/10.1038/17989`.

In primo luogo, desidero ringraziare il professor Corigliano, il professor Frangi e la dottoressa Zega, per avermi coinvolto nella realizzazione di questo progetto. La tematica che mi è stata proposta mi ha incuriosito sin da subito e, in questi mesi di lavoro, ho imparato molto, non solo sull'argomento nello specifico, ma anche nel come affrontare problemi di questo genere mediante una precisa organizzazione del lavoro da svolgere e la condivisione in gruppo di idee e soluzioni. Per questo, e la disponibilità dimostrata anche nel rispondere a ogni minimo dubbio e perplessità, dandomi fiducia e facendo nascere un confronto di idee costruttivo, li ringrazio di cuore. Successivamente, desidero ringraziare la mia famiglia, per avermi sempre sostenuto e incoraggiato in questi mesi che, vuoi anche per la difficile situazione sanitaria che ci siamo trovati ad affrontare nel corso dell'anno, sono stati insoliti. Con alcuni siamo stati costretti a periodi di lontananza. Penso, soprattutto, ai miei nonni (ma non solo) che, per proteggerli, non vedo da settimane ormai. Nonostante questo, siamo riusciti a trovare dei modi per sentirci più vicini, come le videochiamate della domenica allargate. Con altri siamo stati costretti a settimane di convivenza forzata in poco spazio vitale ma, nonostante le giornate un pò tutte uguali, insieme abbiamo superato anche i primi mesi dell'anno. Un enorme ringraziamento, va anche a tutti i miei amici. Grazie a Lara, Martina ed Elena. Grazie per tutti i bei momenti passati insieme in questi anni, dalle vacanze avventurose alle semplici serate in cui ci raccontiamo di tutto e di più, o in cui abbiamo semplicemente bisogno di sfogarci un pò. Purtroppo non ci vediamo tanto quanto spereremmo ma, nonostante tutto, so di poter contare su tutte voi, grazie per esserci sempre e comunque. Grazie mille anche a tutti i miei amici del liceo, i pochi eletti facenti parte del gruppo "Antiquus Citretum 2.0" (ogni tanto mi chiedo da dove ci escano questi nomi molto sobri...): Ila, Marti, Bonda, Bertu, Mattia, Domi e Luca. Grazie per tutti i bei momenti passati insieme. Grazie per le seratone in cui riviviamo le nostre bellissime disavventure liceali, imbarazzanti e non. Grazie per le videochiamate e le partite online a Risiko durante la quarantena, che sono state un'ottima trovata per sentirsi più vicini gli uni agli altri in un momento in cui serviva (però, magari, le prossime volte impegnatevi un pò di più a giocare, altrimenti non c'è gusto a battervi sempre!). Scherzi a parte, grazie per tutto, non so come farei senza di voi e la vostra allegria. Un doveroso grazie va anche agli amici conosciuti al Poli: Nico, Teo e Gian. Per 5 anni abbiamo condiviso buona parte delle nostre giornate, sfasato insieme su formule ed esercizi, sclerato insieme per gli appelli, spesso e volentieri sovrapposti o ravvicinati. D'altronde, che gusto ci sarebbe altrimenti? Questi 5 anni di università sarebbero stati molto più noiosi e pesanti senza di voi. Grazie di cuore a tutti. Senza il vostro appoggio e la vostra vicinanza non sarei mai arrivato a questo risultato. Speriamo di poter tornare a vederci presto, e di poter festeggiare in qualche modo, prima o poi (ovviamente, sempre in ottemperanza al DPCM di turno, ci mancherebbe). Nel frattempo, ci limiteremo alle videochiamate.